Master's thesis

NTNU
Norwegian University of Science and Technology
Faculty of Natural Sciences
Department of Physics

Ole Jakob Berg Bratting

MR image quality assessment of a radiotherapy tailored imaging setup on hybrid PET/MRI: a phantom study

Master's thesis in Applied Physics and Mathematics
Supervisor: Kathrine Røe Redalen
Co-supervisor: René Winter
June 2022

NTNU
Norwegian University of
Science and Technology

Ole Jakob Berg Bratting

MR image quality assessment of a radiotherapy tailored imaging setup on hybrid PET/MRI: a phantom study

Master's thesis in Applied Physics and Mathematics
Supervisor: Kathrine Røe Redalen
Co-supervisor: René Winter
June 2022

Norwegian University of Science and Technology
Faculty of Natural Sciences
Department of Physics

NTNU
Norwegian University of
Science and Technology

Preface

This master thesis was written at the Department of Physics at the Norwegian University of Science and Technology (NTNU) in the spring of 2022. The thesis is the final part of the five-year MSc program in Applied physics and mathematics, with specialization in biophysics and medical technology. During the autumn of 2021 another student in my study program, Maren Lium, wrote a specialization project, which lays a foundation for the work presented in this thesis. This includes Python scripts and data measurements used in this thesis. I would like to thank Maren for her great work and helpful comments when I have had questions regarding scripts or concepts regarding this project. Her work has also been an inspiration for the work I have done.

I will also also thank Kathrine Røe Redalen and René Winther for their helpful guidance throughout the semester. René has been around for all scans and performed the scans with me in Tromsø, Trondheim and Bergen. His enthusiasm and general interest in the work have been very motivating for me and made me work hard. Kathrine has helped me with everything from ordering tickets and hotels for conferences to understanding k-space theory. She has also helped me with the structure of the thesis, giving helpful tips along the way.

The data used in this thesis are, as mentioned, acquired in three different cities, and I would like to thank all people making the scans possible at the PET-centers at University Hospital of North Norway, St. Olavs and Haukeland University Hospital. Sorry if I made your evenings longer to finish the measurements. Lastly, I want to thank Kirsten Margrete Selnæs at the PET-center at St. Olav for giving me access to the MATLAB script that automatically calculates a lot of the data from the ACR QA, you saved me a lot of work.

Abstract

The development of combined imaging modalities can improve radio therapy (RT) by enabling better tumor delineation and identification of aggressive subregions. The combined positron emission tomography (PET) and magnetic resonance imaging (MRI) scanner, PET/MRI, has the advantage of high soft tissue contrast from the MRI in addition to functional and molecular information from PET. Functional information helpful for RT planning can be the degree of diffusion within the tumor region since low diffusion is related to high cell density and often an aggressive tumor. To measure this diffusion, an imaging modality called diffusion weighted MRI (DWI) can be used. Quantitative DWI measurements can vary across scanner and to be able to use the measurements in a clinical setting, this variation has to be assessed. In addition, to use PET/MRI for RT-planning, certain requirements for the imaging equipment must be met. These requirements are related to both patient positioning and adjustment of the practical configuration of imaging equipment. An RT-tailored setup compatible with PET equipment is used to acquire high-quality images. The performance of the RT-tailored setup must be evaluated in multiple centers to reveal any possible variation that must be taken into account if the setup is used clinically.

The image quality and an RT-tailored setup was evaluated by measurements of two different phantoms at three centers located in Tromsø, Trondheim and Bergen during the autumn of 2021 and spring of 2022. The two phantoms used in the evaluation were the Diffusion Standard Model 128 (High Precision Devices, Inc.) and The Large ACR Phantom (Newmatic Medical). The diffusion phantom is recommended by the Quantitative Imaging Biomarker Alliance (QIBA) and the ACR phantom is recommended by the American College of Radiology. The QIBA profile for DWI was used for quality assurance (QA) for the diffusion phantom. QA was performed for the RT-tailored setup in both the head and neck and the pelvic region. In the QA, two sequences were used, first a single-shot benchmark echo planar imaging sequence (SS-EPI) and then a clinically relevant sequence, readout segmentation of long variable echo trains (RESOLVE). For comparison, the benchmark sequence was performed with a 16-channel diagnostic coil. The results were compared with the recommended values in the profile and with similar studies. For the QA of the ACR phantom, the ACR Large Phantom manual was used. A T1-weighted and a T2-weighted axial series was performed in the RT-tailored head and neck setup. The results were compared with the recommended values in the ACR manual and other studies.

The results for QA with the diffusion phantom showed promising results. ADC measures in the center vial of the phantom for the clinical protocol in the head and neck RT-setup in Tromsø, Trondheim and Bergen gave the following results; mean ADC-bias(±%95 CI), -0.02(± 0.06) and -0.16(±0.04) and -0.06(±0.07) $\times 10^{-4}$ mm^2/s; error, 2.94%, 2.2% and 3.55%; short-term repeatability, 0.2%, 0.37% and 0.16%. The intercenter reproducibility for the ADC measurements was 0.65%. The QA of the pelvic RT-setup yielded similar results. For both setups, the error was the

only measure that did not fulfill the QIBA recommendations. The recommended value of error in the ADC measurement is 2%.
The results from the ACR QA showed that the scanners performed similarly. All measures for the T1-weighted series in three centers were within the ACR recommendations, with one exception. The result for image uniformity in Trondheim was 79.13% with a recommended value of 80%. Compared to an RT-setup that consisted of only the head coil, the inclusion of the neck coil enhanced the SNR value by a factor of 1.9 in positions within the coil setup relevant for imaging of neck cancer.

The conclusion is that the scanners in the three centers and the RT-tailored coil setup performed consistently within the recommendations for both the diffusion phantom and the ACR phantom. The further work should focus on clinical imaging of humans to see if the same reproducibility can be achieved as in this phantom study.

Sammendrag

Utviklingen av kombinerte medisinske avbildningssystemer kan fobedre stråleterapibehandling ved å forbedre presisjonen i inntegningen av kreftsvulster og identifiseringen av aggressive områder innad i svulsten . En scanner som kombinerer magnetisk ressonans (MR) og positron emisjon tomografi (PET), PET/MR, har en høy bløtvevskontrast fra MR i tillegg til funksjonell og molekylær informasjon fra PET. Funksjonell informasjon som graden av diffusjon innad i svulsten er nyttig i planleggingen av stråleterapi, siden lav grad av diffusjon er relatert med høy celletetthet og ofte aggressive kreftsvulster. For å kunne måle denne diffusjonen kan diffusjonsvektet MR være et godt hjelpemiddel. Kvantitativ diffusjonsvektet MR kan variere fra scanner til scanner. Denne eventuelle variasjonen må evalueres. I tillegg må utstyret, både det som brukes for å måle MR-signalet og det som brukes for å posisjonere pasienten, også kvalitetssikres for å vite om målingene fra en scanner kan sammenlignes med målingene fra en annen scanner.

Bildekvalitet og et stråleterapi-tilpasset MR-spoleoppsett ble evaluert ved hjelp av målinger av to forskjellige MR-fantomer. Kvailitetssikringen (KS) ble utført på tre universitetssykehus i Tromsø, Trondheim og Bergen i løpet av høsten 2021 og våren 2022. De to fantomene som ble brukt i evalueringen var Diffusion Standard Model 128 (High Precision Devices, Inc.) og The Large ACR Phantom (Newmatic Medical). Diffusjonsfantomet anbefales av Quantitative Imaging Biomarker Alliance (QIBA) og ACR-fantomet anbefales av American College of Radiology. QIBA-profilen for KS for DWI ble brukt for kvalitetssikring av diffusjonsfantomet. KS ble utført for det stråleterapi-tilpassede spoleoppsettet i både hode- og nakkeregionen og i bekkenregionen. To sekvenser ble brukt i KS, først en referanse-sekvens, SS-EPI, deretter en klinisk relevant sekvens, RESOLVE. For sammenligning ble referansesekvensen utført med en 16-kanals diagnostisk hodespole i tillegg. Resultatene ble sammenlignet med anbefalte verdier i QIBA-profilen og med lignende studier. For KS av ACR-fantomet ble ACR Large Phantom-manualen brukt. En T1-vektet og en T2-vektet aksial sekvens ble utført for det stråleterapi-tilpassede hode- og nakkeoppsettet. Resultatene ble sammenlignet med de anbefalte verdiene i ACR-manualen og med andre studier.

Resultatene for KS med diffusjonsfantomet viste lovende resultater. ADC-målinger i senterampullen til fantomet for den kliniske sekvensen med hode- og nakke stråleterapi-oppsettet i Tromsø, Trondheim og Bergen ga følgende resultater; gjennomsnittlig ADC-bias ($\pm$95%CI), -0.02($\pm$ 0.06) og -0.16($\pm$0.04) og -0.06($\pm$0.07) $\times 10^{-4}$ mm^2/s ; feil i ADC målinger, 2.94%, 2.2% og 3.55%; repeterbarhet, 0.2%, 0.37% og 0.16%. Reproduserbarheten for ADC-målingene var 0.65%. KS av stråleterapi-oppsettet i bekkenregionen ga lignende resultater. For begge oppsettene var feilen den eneste parameteren som ikke oppfylte QIBA-anbefalingene. Anbefalt feil i ADC-målingene er under 2%. Resultatene fra ACR KS viste at skannerne yter tilsvarende bra på alle tre sykehus. Alle parametere for den T1-vektede serien i de tre sykehusene var innenfor ACR-anbefalingene, med ett unntak. Resultatet for signaluniformitet i Trondheim var 79,13% med en anbefalt verdi på 80%.

Sammenlignet med et stråleterapi-oppsett som bare besto av hodespolen, økte inkluderingen av halsspolen SNR-verdien med en faktor på 1.9 i posisjoner innenfor spoleoppsettet som er relevante for avbildning av nakkekreft.

Konklusjonen er at skannerne på de tre sykehusene og det stråleterapi-tilpassede spoleoppsettet presterte stabilt innenfor anbefalingene for både diffusjonsfantomet og ACR-fantomet. Det videre arbeidet bør fokusere på klinisk avbildning av mennesker for å se om samme reproduserbarhet kan oppnås som i denne studien.

Table of Contents

List of Figures viii

List of Tables x

1 Introduction 1

2 Theory 4

2.1 Magnetic resonance imaging 4

2.1.1 Basic principles of MRI 4

2.1.2 Excitation 6

2.1.3 Relaxation 7

2.1.4 Spatial encoding 9

2.1.5 k-space 11

2.1.6 Diffusion weighted MRI 12

2.1.7 Fast imaging sequences 14

2.2 PET/MRI 18

3 Materials and Methods 20

3.1 Diffusion phantom 20

3.1.1 Phantom measurements 20

3.1.2 Segmentation and image analysis 23

3.2 ACR phantom 26

3.2.1 Phantom measurements 26

3.2.2 Image analysis 28

4 Results 36

4.1 Diffusion phantom 36
4.2 ACR-phantom 45

5 Discussion **54**

5.1 The QIBA phantom 54
5.2 The ACR phantom 58

6 Conclusion **61**

Bibliography **62**

Appendix 65
A help_functions.py 65
B ADC_qualities_near_isocenter.py 66
C ADC_reproducibility.py 68
D ADC_b-value_dependence.py 69
E SNR.py 71
F PIU calculation 74
G Ghosting ratio calculation 77

List of Figures

1.1 Comparison of imaging modalities 2

2.1 Larmour frequency 5

2.2 MRI scanner 6

2.3 Excitation 7

2.4 FID signal 8

2.5 T1-relaxation 9

2.6 T2-relaxation 10

2.7 SE-sequence diagram 11

2.8 Diffusion sequence diagram 13

2.9 SE-EPI sequence diagram 15

2.10 k-space filling in SS-EPI 15

2.11 RESOLVE sequence diagram 16

2.12 k-space filling in RESOLVE 17

2.13 Comparison of RESOLVE and SS-EPI image quality 17

2.14 Comparison of imaging modalities 19

3.1 Diffusion phantom positioning 22

3.2 Diffusion phantom segmentation 24

3.3 ACR phantom 27

3.4 ACR phantom positioning 28

3.5 Geometric distortion in ACR QA 30

3.6 Resolution in ACR QA 31

3.7 Slice thickness accuracy and slice position accuracy in ACR QA 32

3.8 PIU, LCD and ghosting in ACR QA 34
3.9 SNR in ACR QA 35

4.1 Results for QIBA QA for 16-channel diagnostic head coil 38
4.2 Results for QIBA QA for head and neck RT-setup 39
4.3 Results for QIBA QA for pelvic RT-setup 40
4.4 b-value dependence for ADC value 42
4.5 b-value dependence for SNR-values 43
4.6 SNR-values for different RT-setups 44
4.7 Results for the T1-weighted series in ACR QA, three centers 47
4.8 Results for the T1-weighted series in ACR QA, three centers 48
4.9 Results for the T1-weighted series in ACR QA, one center 50
4.10 Results for the T1-weighted series in ACR QA, one center 51
4.11 Results for the T1-weighted series in ACR QA, setup dependent 52
4.12 Results for the SNR calculation for the ACR phantom, setup dependent 53

List of Tables

3.1 Sequence parameters for DWI QA 21

3.2 DWI measurements summary 22

3.3 QIBA QA recommendations 26

3.4 Sequence parameters for ACR QA 27

3.5 ACR QA recommendations 29

4.1 ADC bias results in QIBA QA 36

4.2 Error in the ADC value measurements in QIBA QA 37

4.3 Short-term repeatability in QIBA QA 37

4.4 Short-term repeatability 41

4.5 Results for the T1-weighted series in ACR QA 46

4.6 Results for the T2-weighted series in ACR QA, three centers 46

4.7 Results for the T1-weighted series in ACR QA, one center 49

4.8 Results for the T1-weighted series in ACR QA, one center 49

Chapter 1

Introduction

Radiotherapy (RT) is a cancer treatment used to damage cancer cells and through this damage halt the cells growth and further division. The treatment causes damage in the DNA-strands which in turn causes cell death [1]. In current cancer treatment, RT is one of the most used treatment modalities. The basic principle is that by using high-energy radiation of photons, electrons, other charged particles, or radioactive sources, we can deliver region-specific treatment to areas with cancer cells. RT is often used together with other treatments such as immunotherapy, chemotherapy and surgery to increase the probability of curing the cancer. The rays used in RT also damage healthy cells, so it is of great importance that the radiation is delivered to the correct area [2].

RT is usually divided into external beam RT (EBRT) or internal beam RT, also called brachytherapy. The most common RT is the EBRT and is the one that is relevant for this thesis. In EBRT, the radiation dose is delivered to the patient using a linear accelerator (linac). The dose is the energy deposited into the tissue from the radiation and is given as energy per mass of tissue. The linac can deliver the RT through either electrons or photons.

In modern cancer treatment, techniques have been developed to deliver the dose with increasing precision. Techniques such as intensity modulated radiotherapy (IMRT) and volumetric-modulated arc therapy (VMAT) give a highly improved accuracy. The beam in IMRT and VMAT is modified with the help of small "leaves" of tungsten that together build up a multileaf collimator. This device forms the beam in the desired form to best fit the tumor area from the given angle. The linac has a gantry that can rotate around the patient. With the help of this rotating gantry the linac is able to radiate the tumor from all angles and gives a great advantage compared to earlier techniques where the beam is modified by the use of angles. The difference between the two techniques is that IMRT irradiates the target from fixed angles while VMAT irradiates continuously while the gantry rotates [2]. In current cancer treatment, most of the treatments are given with VMAT.

To be able to deliver the correct dose to the tumor volume, it is crucial that we have images of high quality. Images are used both to locate the tumor and to identify and locate healthy tissue and organs in proximity of the tumor, these organs are called organs at risk (OAR). Several medical imaging modalities are used in the planning process for RT. Most commonly, X-ray computed tomography (CT) is used, this is because CT provides information about the electron density in addition to the anatomical information. The information about electron density is vital for the calculation of the dose delivered in the tissue. Magnetic resonance imaging (MRI) is another

imaging modality used in cancer treatment planning. MRI has a superior soft tissue contrast compared with CT, which gives MRI an advantage when it comes to localization and delineation of tumors and healthy tissue. Positron emission topography (PET) is used to obtain molecular information about the tumor. This information can include metabolism and heterogeneity, which can be used to adapt the treatment of the most aggressive regions of the tumor with the highest dose. The 3D images acquired by the different imaging modalities can be combined and then used to delineate the tumor and the OARs.

After imaging, the next step in the treatment cycle is to decide which irradiation technique the patient will be treated with. The RT-treatment is then simulated and the dose calculated before the dose distribution is visualized and evaluated. If the treatment plan is approved, the treatment can be given to the patient. Before treatment starts, the importance of patient positioning is again addressed. The patient has to be positioned in the exact same position as it was when imaged and previously treated. When the positioning of the patient is correct, the treatment is given. Between RT-fractions, imaging can be used to verify the effect of the treatment and give reason to continue with the given plan or to make changes to optimize patient outcome.

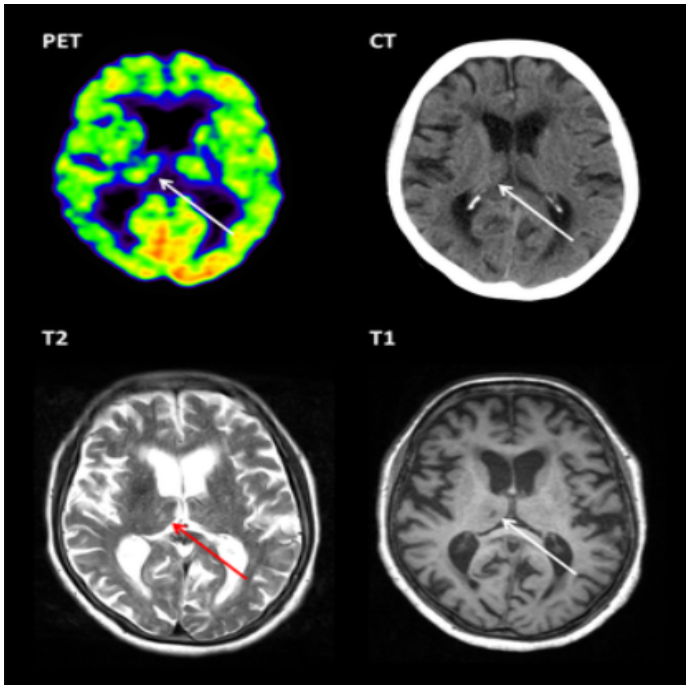

Figure 1.1: A brain imaged with PET, CT and MRI (T1-weighted and T2-weighted) to show the different imaging modalities highlight different parts of the human body [3].

Image modalities can be combined in the same scanner. In such a scanner, the images are acquired simultaneously and the co-registration of the images is done precisely by the scanners software. With the introduction of combined PET/MR scanners, treatment can be improved by more precise tumor delineation, localization of more radioresistant areas of the tumor and better assessment of the treatment given. There are also challenges that must be considered and overcome to be able to integrate the PET/MR scanner into the RT workflow. In the localization process, the immobilization of the patient is extremely important. An inaccurate location of the OARs and the tumor volume due to the different positioning of the patient between imaging and treatment will give the wrong dose to the OARs and the tumor volume. To ensure that the patient is immobilized, equipment such as casts, headrests and moulds can be used for different parts of the body. In a

clinical setup for head and neck PET/MR imaging an immobilization masks is used in addition. To ensure the same positioning as in the linac a flat table top is used for the PET/MR examination. The MR-coil setup has to be RT-tailored as well. An RT-tailored coil setup used for head and neck imaging consists of MR-coils mounted on flexible coil holders. These coils ensure improved signal acquisition in the head an neck area. All this equipment must be compatible with PET and MRI [4].

Diffusion weighted MRI (DWI) has been proven to improve both tumor detection / characterization and also for monitoring treatment response. Therefore, DWI is of high clinical interest. DWI measures the diffusion of water, which is a complex mechanism dependent on multiple factors such as cell density, viscosity of extracellular fluids and cell membrane integrity. DWI quantifies these factors and can express them as an apparent diffusion coefficient (ADC). In this way, DWI can potentially be used as a biomarker to stage and characterize cancers[5].

To be able to use quantified data from modalities such as DWI in a clinical assessment, it is important to have high-quality images and results that are comparable in size between centers/scanners. To assess whether the results are sufficient, quality assurance (QA) can be performed. QA is usually performed with the use of phantoms. The Quantitative Imaging Biomarkers Alliance (QIBA) is an institution that develops and provides technical performance standards, QIBA profiles, which can be used for QA of imaging modalities such as DWI. By using these standard profiles, the results from different centers acquired with the same coil setups and same scanner setting should be comparable [6].

The American College of Radiology (ACR) is a leading institution for accreditation for MRI scanners. Their accreditation program is known as the "gold standard". The ACR phantoms are developed to assess a broad spectrum of the scanners abilities and quality. Several centers use the ACR phantoms as a weekly quality control. The QA performed with the ACR phantoms is standardized in profiles published by the ACR.

In this work, the quality of DWI on a hybrid PET/MR scanner has been assessed for scanners at three university hospitals: University hospital in North Norway in Tromsø, St.Olavs hospital in Trondheim and Haukeland university hospital in Bergen. Diffusion QA was performed according to the QIBA profile for DWI [7]. Quality was assessed in the head and neck region and the pelvic region. The phantom used in the QA was the Standard Model 128 (High Precision Devices, Inc.).

In addition to DWI QA, a QA was performed for The Large ACR Phantom (Newmatic Medical) according to the ACR Large phantom profile in the three centers with the same RT-tailored setup as the DWI QA [8]. QA for ACR was performed only for the head and neck region. The results in the three centers were compared with the recommendations given in the ACR profile and between the centers.
The project has focused on comparing an RT-tailored head and neck coil setup designed at NTNU with a diagnostic 16-channel diagnostic head and neck coil to assess if the image quality is good enough for clinical use. Another focus has been to assess the feasibility of using the quantitative measures of the phantom QA in a larger intercenter study.

Chapter 2

Theory

2.1 Magnetic resonance imaging

2.1.1 Basic principles of MRI

MRI is a non-invasive imaging modality that utilizes the magnetic properties of the nucleus. For magnetic resonance imaging of the human body, the most used nucleus is the hydrogen nucleus, which consists of one proton. Hydrogen is used because of the major presence of hydrogen in the body as contributor for water and approximately 60 per cent of our body is water. All protons have a fundamental property called spin. A very simplified classical analogy to spin is that a mass spins around itself. In addition to spin, protons possess a charge and therefore each proton has something called a magnetic dipole moment, μ. This is a consequence of the laws of electromagnetism [9]. The magnetic dipole moment is taken advantage of by applying an external magnetic field, $\mathbf{B_0}$, to the area of interest. This external field is applied by using a coil. The coils are in their simplest form just a wire circuit formed in a way that it makes a magnetic field when an current is driven through the coil, following from fundamental electromagnetism. The magnetic moment of the protons will align parallel or anti parallel to $\mathbf{B_0}$. The two spin states differ in energy, the state parallel to $\mathbf{B_0}$, *spin up*, will be the lower energy state while the anti parallel state, *spin down*, will be the higher energy state [10].

$\mathbf{B_0}$ will be giving the magnetic dipole moment a torque and cause the protons to precess around $\mathbf{B_0}$, as seen in figure 1. The frequency that the protons are precessing with is called the Larmour frequency, ω [10]. ω is dependent on $\mathbf{B_0}$ and γ and given by,

$$\omega = -\gamma B_0. \tag{2.1}$$

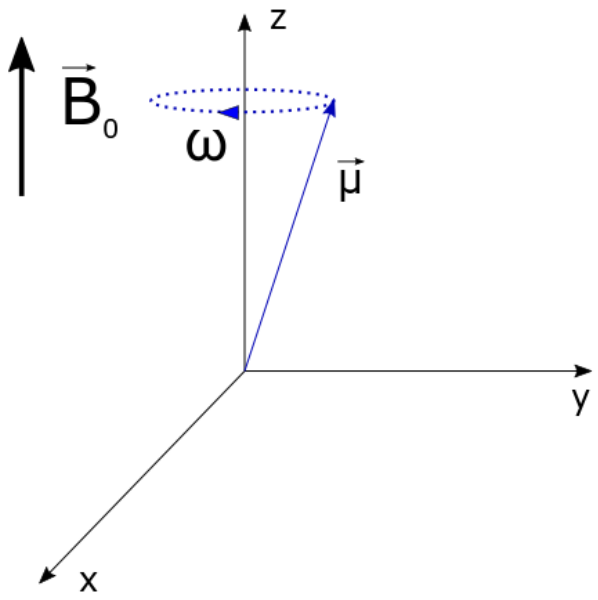

Figure 2.1: In an external magnetic field, B_0 a proton with a magnetic moment μ precess around the field direction with the Larmour frequency, ω .

In 1946, Felix Bloch published a set of macroscopic equations to explain the origin of the MR-signal. While magnetic resonance is a quantum mechanical process, it is possible to have a macroscopic view at the process. Bloch used the assumption that all individual spins add up to the net magnetization vector **M** [11]. In equilibrium a small majority of the spins will be in the spin up state because of the lower energy. The sum of all the spins can therefore be seen as a net magnetization in the same direction as $\mathbf{B_0}$. The ratio between the population of spin up and spin down is given by the Boltzmann distribution. During MRI, **M** is purposely tipped out of equilibrium. In this situation **M** will also experience a torque from $\mathbf{B_0}$ and therefore precess around it. The change of **M** over time is described as,

$$\frac{d\vec{M}}{dt} = \gamma\vec{M} \times \vec{B}. \tag{2.2}$$

The cross product, $\mathbf{M} \times \mathbf{B}$ gives a resultant vector perpendicular to **B** and **M**. The amplitude of this vector is equal to $|M||B| \sin\alpha$ where alpha is the angle between **B** and **M**.

The net magnetization vector can be divided into three components, $\mathbf{M_x(t)}$, $\mathbf{M_y(t)}$, $\mathbf{M_z(t)}$, each dependent on time. Usually, z is the longitudinal direction while x and y are in the transverse plane. With only the external field, $\mathbf{B_0}$, present we say that $\mathbf{M_z(t)}$= $\mathbf{M_0}$ and there is no magnetization in the transverse plane.

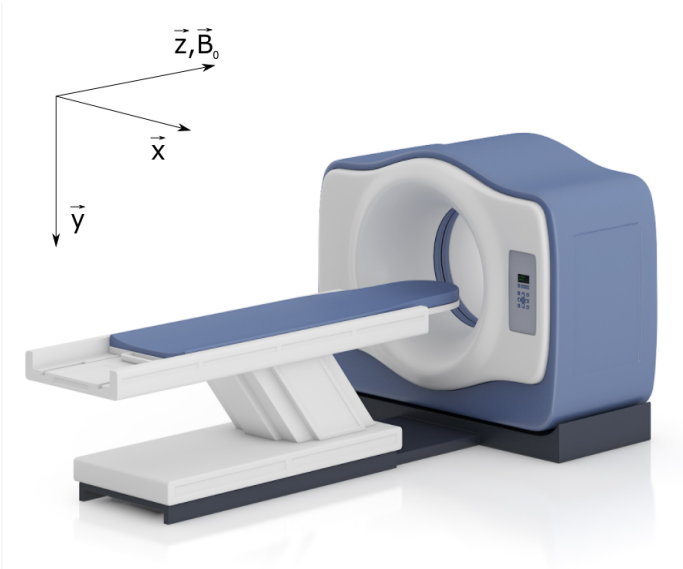

Figure 2.2: Sketch showing the axes in an MRI scanner. $\mathbf{B_0}$ and $\mathbf{z}$ in the longitudinal direction and $\mathbf{x}$ and $\mathbf{y}$ in the transverse plane.

Source: [12]

2.1.2 Excitation

To be able to record any signal in a MRI we need to flip the net magnetization vector down to the xy-plane. This is done by applying a second magnetic field, $\mathbf{B_1}$, for a limited time period. $\mathbf{B_1}$ is perpendicular to the existing $\mathbf{B_0}$ and is created by induction of radio frequency (RF) waves in the transmit coils. These transmit coils use an alternating electrical current to create a magnetic field oscillating with a frequency similar to the Larmour frequency. This short-lasting RF field is often called an RF-pulse. As we recently looked at, the spins aligned parallel to $\mathbf{B_0}$ are in a lower energy state, this yields that to flip the net magnetization the medium has to receive energy from the RF-pulse. It is important to remember that we cannot state which direction each spin has, but that the entire ensemble of spins receives this energy and the net magnetization vector is rotated. The relative orientations of the individual spins are not rotated.

By again using the Bloch equation, we can say that the situation for change in the net magnetization can be described as,

$$\frac{d\vec{M}}{dt} = \gamma\vec{M} \times B_0 \vec{+} B_1. \tag{2.3}$$

To be able to flip the magnetization vector away from the z-direction it is important that the RF-pulse oscillates with a similar frequency as the Larmour frequency. By controlling how long we apply the $\mathbf{B_1}$- field, we can control how much the magnetization vector will be flipped. The flip angel α is given by

$$\alpha = \gamma B_1 t_{rf}, \tag{2.4}$$

where α is the relative flip angel from the z-direction, B_1 is the applied RF-field and t_{rf} is the time we apply the field.

By flipping the net magnetization vector down to the xy-plane we end up with a transverse component, M_{xy}. This component will precess around the z-direction with ω giving an alternating magnetic flux in a receiver coil. An alternating magnetic flux produces an electrical current that can be measured, following Faradays law of induction [13]. In different MRI sequences different RF-pulses are often named after what flip angel the net magnetization vector experiences. As an usual example, a 90 degree RF-pulse applied at $T = 0^+$ will take all the magnetization in the z-direction down into the xy-plane and make $M_z(0^+) = 0$ and $M_{xy}(0^+) = M_0$, see figure 2.6.

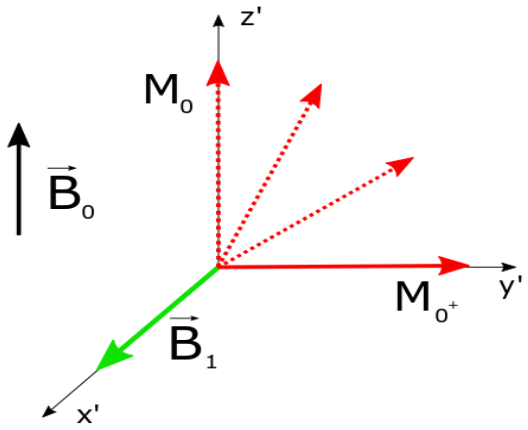

Figure 2.3: Schematic of the excitation process drawn in a frame of reference rotating with ω. The effect of an 90°excitation RF-pulse applied in the x' direction. The energy from the RF-pulse is transferred to the ensemble of spins and the net magnetization vector is rotated down in the xy-plane after a time t.

2.1.3 Relaxation

After we have applied an RF-pulse, the external field $\mathbf{B_1}$ is turned off. The external field $\mathbf{B_0}$ will then make the net magnetization restore its equilibrium state. This process is called relaxation and is the process in which protons interact and lose some of their energy. The signal that will be measured in the receiver coils is often called the free induction decay (FID). The FID is caused by the relaxation divided in two mechanisms, T1-relaxation and T2-relaxation.

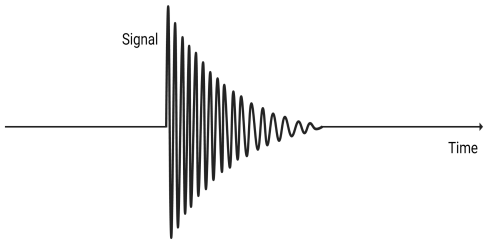

Figure 2.4: The free induction decay (FID) signal.

T1-relaxation is called spin-lattice or longitudinal relaxation. In this relaxation process, the net magnetization is growing back to its original value, M_0, parallel to the external field B_0 with a rate R1 which is the inverse of T1. The lowest possible energy state for the spin is parallel to B_0, this indicates that there must be some energy transferred away from the spin system for this T1-relaxation to occur. The energy is transferred to nearby atoms, molecules and nuclei by collisions, rotations or electromagnetic interactions. The longitudinal relaxation can be described by,

$$\frac{dM_z}{dt} = \frac{1}{T_1}(M_0 - M_z). \tag{2.5}$$

Solving (2.6) for $\mathbf{M_z}$,

$$M_z = M_0(1 - e^{-\frac{t}{T_1}}), \tag{2.6}$$

.

shows that T1-relaxation follows an exponential curve with a rate given by the T1-value, specific for each tissue type. T1 is given as the time required for the net magnetization vector to regain 63 percent of its initial value, $1 - (1/e) \approx 0.63$. Typical values for T1 is from a few tenths of a second to several seconds. The difference in T1 can be utilized to make contrast in MRI by using T1-sensitive pulse sequences. In T1-weighted images, tissues with short T1 have a brighter signal than tissues with long T1. This is because more of the original magnetization vector has grown back before the RF pulse is applied to bring the vector down to the xy-plane.

The other relaxation mechanism, T2, is happening because the spins are dephasing. All the different spins will interact with each others small magnetic fields. This small interaction will cause the spins to experience different magnetic fields and therefore end up with different rotation frequency. The T2-relaxation will cause transverse magnetization decay as the resulting net magnetization vector weakens as spins are dephased. This decay follows an exponential curve with a rate R2, which is the inverse of T2. T2 is the time required for the transverse magnetization to loose 63 percent of its initial value. The difference in T2 for different tissues can be used to make contrast in MRI by using T2-weighted pulse sequences. In a T2 weighted image, the tissue with the longest

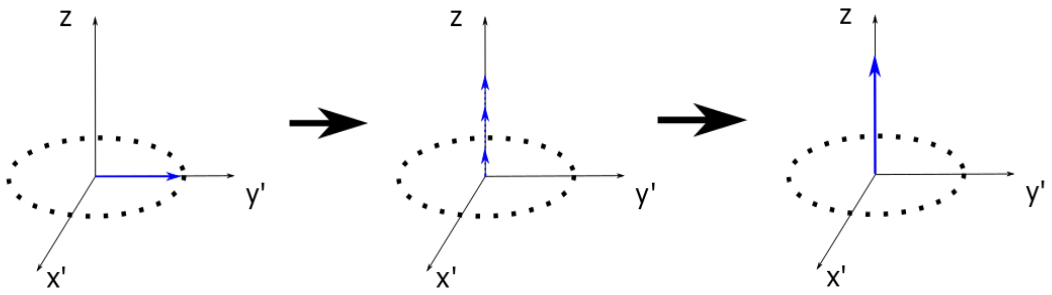

Figure 2.5: Schematic of longitudinal relaxation drawn in a frame of reference rotating with ω. (a) Immediately after excitation (b) Energy is transferred from the spins in the highest energy state, in opposing direction to $\mathbf{B_0}$, transfer energy to nearby atoms, molecules and nuclei by different mechanics. (c) The spins are completely redistributed according to equilibrium conditions.

T2 will have the strongest signal while the tissue with the shortest T2 will appear darker. When considering T2 relaxation we also have to take T2'-relaxation into account. The T2'-relaxation is happening because of spatial inhomogeneities in the external magnetic field. These inhomogeneities will dephase spins that experience different magnetic fields. The true relaxation time, T2*, is taking both the dephasing from external effects (T2') and internal effects (T2) into account. The rate R2* will therefore be the sum of R2' and R2. The dephasing effect caused by the external field can be recovered by applying a pulse reversing the dephasing process. On the other hand T2-relaxation can not be reversed as this is caused by random and time-dependent field variations [10]. The transversal relaxation, T2, can be described by,

$$\frac{dM_{xy}}{dt} = -\frac{1}{T_2} M_{xy}. \tag{2.7}$$

Solving (2.7) for M_{xy} gives,

$$M_{xy} = M_0 e^{-\frac{t}{T_2}}. \tag{2.8}$$

2.1.4 Spatial encoding

The signal recorded for a specific time in an MRI scan originates from all the spins that have been excited. To be able to make an image of the scanned object, we have to be able to distinguish the amount of signal from each spatial location. To achieve this spatial encoding, gradients in different directions are used. The Larmour frequency is dependent on field strength, as (2.1) shows, and the idea is that the frequency of the spins can be used to locate the spins. The gradients G_x, G_y, G_z are the different gradients used to perturb the spins. G_z is the gradient used for slice selection. The gradient is a magnetic field with varying strength along the desired axis, for slice

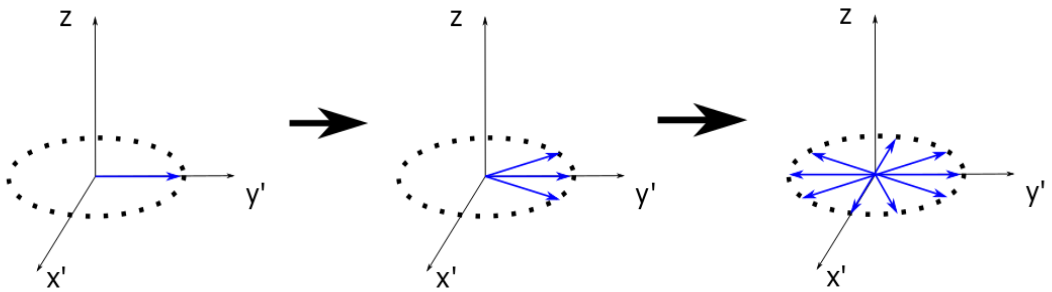

Figure 2.6: Schematic of the transversal dephasing, drawn in a frame of reference rotating with **omega**. (a) The situation immediately after the excitation. (b) Due to the spin-spin interactions and field inhomogenities the spins will rotate with slightly different frequencies. The spins dephase. (c) At some time t after excitation the spins will be completely dephased.

selection this is often chosen as the Z-axis. This will cause the spins along the z-axis to precess with different frequencies in accordance with (2.1). This slice selection gradient has to be switched on during all RF-pulses as only spins excited will be the ones with a specific frequency. Further the G_y gradient is applied for a short time to give a phase difference between the spins in y-direction. A changed magnetic field for a short time leads to a changed frequency and therefore a phase difference between spins experiencing different magnetic fields. The last gradient, G_x, called the frequency encoding gradient or the readout gradient, gives a difference in the frequency along the x-axis [14].

By using different pulse sequences which consists of different gradients in different order with different spacing and duration we are able to achieve the desired contrast. To be able to apply all these gradients in different directions, the MRI-scanner needs some time, meanwhile, the MRI signal is starting to decay the moment the spins are excited. The equipment used to apply the gradients and read out the signal has to be given time so we are able to record what we really want. Therefore, it is common to record the echo of the original signal, which is the original signal brought back at a later time, in figure 2.7 the echo is the second signal occurring on the signal axis. There are two main classes of sequences often used in MRI, spin echo (SE) and gradient echo (GRE) sequences. SE and GE sequences differ in how the echo signal is made. In SE-sequences a 180°pulse is applied between the phase encoding gradient and the readout gradient. This pulse is reversing the dephasing caused by the external effects. The signal measured in a SE-echo sequence is an echo instead of the FID and is bound by the true T2 relaxation. Figure 2.7 shows a general SE-sequence.

MRI have the ability to generate contrast based on several properties of the different tissues that are being imaged. Different weighting of properties gives a wide range of possibilities. The most common ones are T1 and T2 weighting. Looking at equation (2.6) we see that by letting the time t pass for a long time before exciting the spins again, long repetition time (TR), the T1 value of the different tissue will have a small impact on the signal intensity. This is because M_z will be

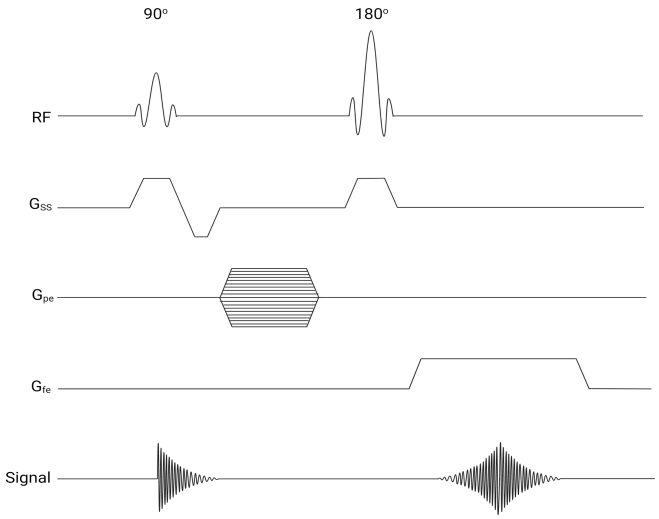

Figure 2.7: Sequence diagram for a spin echo sequence. The levels of the phase encoding gradient represents the different repetitions. Readout of the signal happens simultaneously as the frequency encoding gradient.

equal to M_0 for every tissue after a long TR. By using a short TR the different tissues will be able to decay to different degree with the T1 value determining to which degree they decay. Equation (2.8) shows that a very short time before acquiring the M_{xy} will give the different tissues to little time to dephase long enough to be able to distinguish tissues based on their T2. The time between excitation and the readout is the echo time (TE). Therefore a short TR and short TE gives a T1 weighted image. Short TR is usually in the size of the mean T1 of the imaged tissues, under 600 ms. Short TE is usually under 30 ms. .

For T2 weighted image the case is the opposite. In this weighting the goal is to distinguish tissues based on T2 values and a long TR and long TE is used to achieve this. A along TE is usually longer than 1500 ms and a long TE is usually around 100 ms [15], [16].

2.1.5 k-space

The MRI data is acquired in real time and stored in something we call $k-space$. K-space is a 2D or 3D representation of the spatial frequencies in the MR image. Each point in k-space contains spatial frequency and phase information about all the excited spins that makes the MR signal, in other words only the spins that are excited. K-space has axes k_x and k_y, points along the k_x-axis is representing spatial frequencies along the x direction of the final image while points along k_y represent the spatial frequencies along the y-axis in the final image. Any real image will have spatial frequencies in all directions and as a consequence k-space end up as a 2D-array of points representing the spatial frequency from all directions [14]. By convention k-space is filling one row for each phase encoding step. The rows are in k_x direction while the phase encoding steps are in k_y direction. That means that for each echo one row of k-space is sampled. The x- and y-gradients are used to move through k-space. Along the k_x-axis this is done by applying a frequency encoding gradient under evolution of the MRI-signal. By doing that, successive data points in the recorded signal will correspond to increasing spatial frequency and therefore be directly plugged into k-space. Each step on k_y axis is the phase encoding step applied for that readout. For each new

phase encoding step we move to a new line [17].

Increased spatial frequency represent edges and details in an image while low spatial frequencies represent the shapes and contour, therefore the edges of k-space is said to be where the small details are stored while the center is where the shapes are stored [14]. By taking the 2-dimensional Fourier transform of the k-space data we end up with a image. This is because a Fourier transform of a signal in the time domain, which is the signal stored i k-space, is a signal in the frequency domain. The Fourier transform will decompose the time signal with varying frequency, into its frequency components. When applying gradients we encode the positions in the xy-plane to frequency and phase values. With the help of the Fourier transform we now have frequency components that can be assigned to positions and the result is an image.

2.1.6 Diffusion weighted MRI

Diffusion weighted MRI (DWI) is a MRI imaging technique utilizing diffusion to get contrast. Diffusion is the random microscopic movement of small molecules related to the thermal energy in the tissue, also known as Brownian motion. Similar to other MRI-techniques, the small molecules in focus in DWI is water. In free non-directional (isotropic) diffusion, the mean squared displacement in 3 dimension Brownian motion is given by the relation:

$$\langle r^2 \rangle = 6Dt, \tag{2.9}$$

where t is time and D is the diffusion coefficient. D depends only on the particle and the medium at the given temperature [18].

In biologic tissue, the movement of the water molecules are not isotropic as the movement is restricted by cell membranes, macromolecules and organelles. This creates diffusion anisotropy, the water is diffusing more in some directions than other. The measured diffusion coefficient in a DWI is named the apparent diffusion coefficient and this coefficient can be dependent on permeability and perfusion as well.

The difference in diffusion of water in different tissues is what gives contrast in DWI. The signal is acquired by two strong diffusion gradients with opposite polarization. During the application of the first gradient the protons get an additional phase shift according to their position and therefore dephase. The pause following the first gradient gives the spins some time to diffuse. The spins will therefore have a new position when the second gradient is applied. The second gradient will, because of its opposite polarization, rephase the spins as long as the spins are located at the same position. The spins that have diffused along the direction of the gradient will not be rephased. The incomplete rephasing will give signal loss. The areas with the highest signal loss will be the areas with the highest diffusion, and the areas with a low signal loss will be the areas with the most restricted diffusion [19].

The magnitude of diffusion weighing in a DWI can be expressed by the b-value, The b-value is given as,

$$b = \gamma^2 G^2 \delta^2 (\Delta - \delta/3), \tag{2.10}$$

where G is the amplitude of the gradients, δ is the duration of each of the gradients and Δ the

time interval between the two gradients, visualised in figure 2.8 [19].

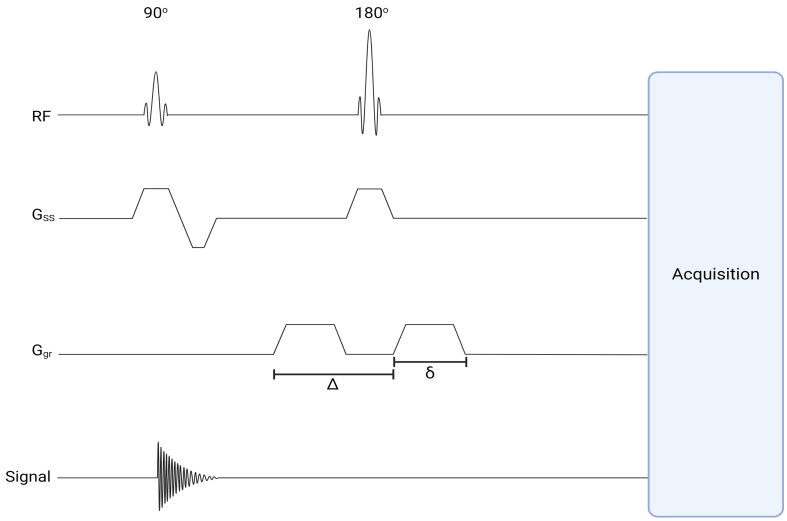

Figure 2.8: Sequence diagram for a diffusion preparation followed by the image acquisition. The direction of the diffusion gradient can be chosen as any direction.

There are several models available to quantify information wanted from a DWI. The simplest and most commonly used model for DWI analysis is the mono-exponential model,

$$S(b) = S_0 e^{-ADC \cdot b}, \tag{2.11}$$

where S(b) is the signal for a given b-value and S_0 is the signal without any diffusion gradients. This equation shows that a higher b-value will give rise to a more pronounced signal difference between areas with high and low diffusion. ADC is the apparent diffusion coefficient. The ADC is the measured diffusion coefficient and is named apparent since it can be influenced by perfusion and permeability also. In images with low b-values the perfusion will influence more as (2.11) shows.

The diffusion in a DWI is only measured along the direction of the diffusion sensitizing gradients. The diffusion in biological tissue is highly anisotropic and we need to measure the diffusion in several directions to get a good estimation. The gradient sequence is measured in at least three directions. As an example, these three directions can be along the laboratory x, y, and z axes. The directionally-specific diffusion coefficients are D_{xx},D_{yy} and D_{zz}. The signals of the respective direction source images are then given by,

$$S_x = S_0 e^{-D_{xx} \cdot b} \qquad S_y = S_0 e^{-D_{yy} \cdot b} \qquad S_z = S_0 e^{-D_{zz} \cdot b}. \tag{2.12}$$

The three source images are then combined to give the resulting DWI, also called trace image [20]. The most common method to use for combination of the images is to take the geometric mean,

$$S_{DWI} = \sqrt{S_x S_y S_z} = S_0 e^{-(D_{xx} D_{yy} D_{zz})b/3} = S_0 e^{-b(D_{trace})/3} = S_0 e^{-b \cdot ADC}. \tag{2.13}$$

Since the biological tissues are anisotropic they have multiple diffusion coefficients that vary by

direction. The diffusion can be represented by a diffusion tensor, a 3x3 array of numbers in the example where we measure the diffusion along three directions. The term *trace* means the sum of the diagonal elements of such a tensor. We use the average value of the trace to reduce the multi-directional diffusivity at each point into a single number. This number is then considered as the ADC value of that voxel.

The results from a DWI-sequence can also be presented by the ADC value, a so called ADC map. This map is a image with the corresponding ADC value of each voxel [20]. The calculation uses a S_{DWI} image and a b0 image, which is just a T2-weighted image. The ADC value is calculated by rearranging equation (2.11):

$$ADC = \frac{1}{b} ln \left(\frac{S_0}{S_{DWI}} \right), \tag{2.14}$$

2.1.7 Fast imaging sequences

Conventional MRI is prone to motion artifacts due to the long scan time and can have trouble imaging rapid physiological processes. To deal with these challenges, echo planar imaging (EPI) has been developed. EPI is a fast imaging technique filling a greater part of k-space for each RF-pulse sequence. This is done by rapidly reversing the readout gradient. EPI is divided between single-shot EPI (SS-EPI), which acquires all of k-space in a single excitation, and multi-shot EPI (MS-EPI) which fills the k-space using multiple excitations. EPI can be pure GRE sequences or combining a spin echo with the gradient echo train.

For the SE-EPI, the sequence starts with a 90° pulse to excite spins in the desired slice selected by the slice selective gradient, see figure 2.9. Then follows a phase and a frequency gradient to move to the start position of the k-space that is going to be sampled. No signal is recorded during this time. The frequency and phase gradients depend on the method that is used to fill k-space. In the example in figure 2.10 a zig-zag method is used and the filling of k-space starts in the bottom left corner. Next a 180° pulse is applied to refocus the spins before the recording begins. The recording is done one line at a time with a change in the polarity of the frequency encoding gradient between consecutive lines. The changing of lines along k_y is done by very short phase gradients, called "phase-blips". The "phase-blips" will change the position in k-space to a new k_y-value, the sequence is shown in figure 2.9 [21].

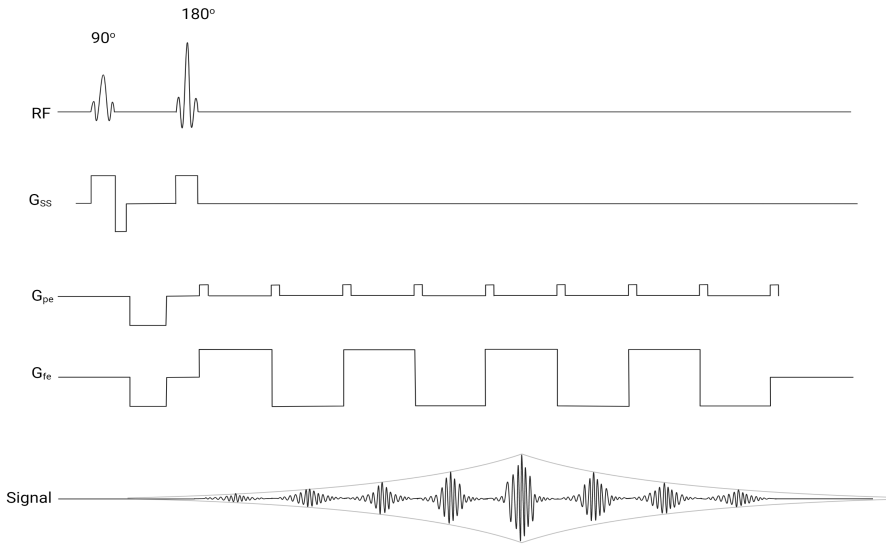

Figure 2.9: SE-EPI sequence diagram.

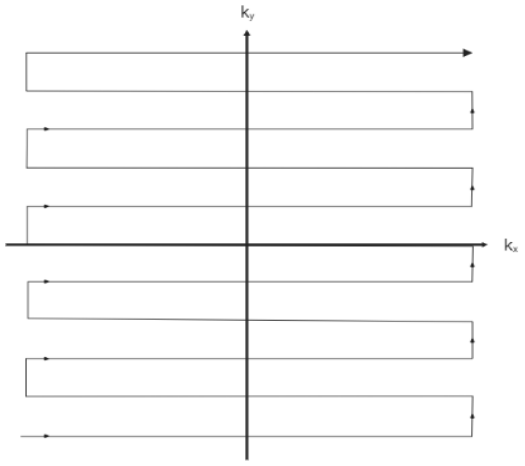

Figure 2.10: k-space trajectory for a SS-EPI sequence.

SS-EPI has the advantage of low sensitivity to motion-induced artifacts because of its fast image acquisition. However, the technique is very sensitive to susceptibility-induced artifacts, most evident in areas with many air-tissue boundaries. The technique is also prone to low signal/noise ratio (SNR) and spatial blurring. To cope with these artifact sensitivity, we can introduce parallel imaging techniques. Parallel imaging techniques are acquiring a reduced amount of the k-space and thus speed up the acquisition time. Parallel imaging algorithms are then used to regenerate the parts of k-space not acquired and construct artifact-free images. The use of parallel imaging will help a lot at lower field strengths, but at higher field strengths, such as 3T, the technique is still prone to artifacts. By using multi-shot EPI (MS-EPI) instead of SS-EPI the artifacts can be further limited.

MS-EPI uses several shots to fill k-space and is also called readout segmentation. Siemens has developed a DWI imaging sequence combining parallel imaging and segmented EPI. Readout seg-

mentation of long variable echo trains (RESOLVE) is a sequence that gives high resolution DWI with reduced susceptibility artifacts[22]. The RESOLVE-sequence is more time consuming than standard SS-EPI. This increased time can be reason for some increased motion in the patient, which can further lead to artifacts. This is because motion during the diffusion sensitizing gradient leads to a spatially dependent phase variation that is different from excitation to excitation. If not compensated for, the following artifacts will be severe. In RESOLVE a 2D navigator acquisition is used to perform 2D nonlinear phase correction and at the same time control the reacquisition of unusable data that cannot be corrected. The unusable data is characterized by navigator images with large nonlinear phase errors. The reacquisition is done at the end of the standard measurement and the navigator images with the largest phase error are acquired before the final images are reconstructed. Generalized Autocalibrating Partially Parallel Acquisitions (GRAPPA) is used as the parallel imaging algorithm to reconstruct images in RESOLVE. The idea in GRAPPA is to use parts of the acquired k-space to calculate the missing parts. After the calculation of the missing parts, the filled k-space is Fourier transformed to the final image.

The RESOLVE sequence diagram is presented in figure 2.11. The sequence has two diffusion sensitizing gradients, each followed by a spin echo. The first spin echo is the imaging echo while the second spin echo is the 2D-navigator echo. Before the imaging echo, a variable prephasing gradient (colored pink) sets a variable offset along the k_x-axis, and a different region of k-space is imaged in each shot. Before the navigator echo, there is a constant prephasing gradient ensuring that the same central part of k-space is acquired for each shot. Figure 2.12 shows the k-space trajectory of the RESOLVE sequence [23].

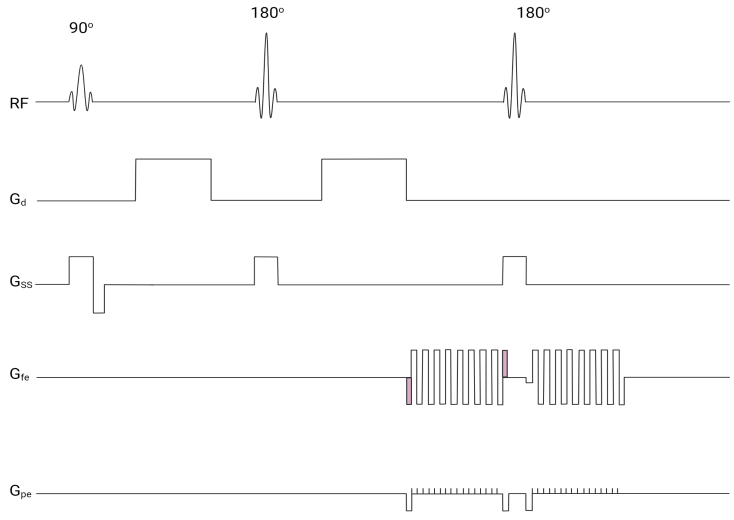

Figure 2.11: RESOLVE sequence diagram. Figure adapted from [23].

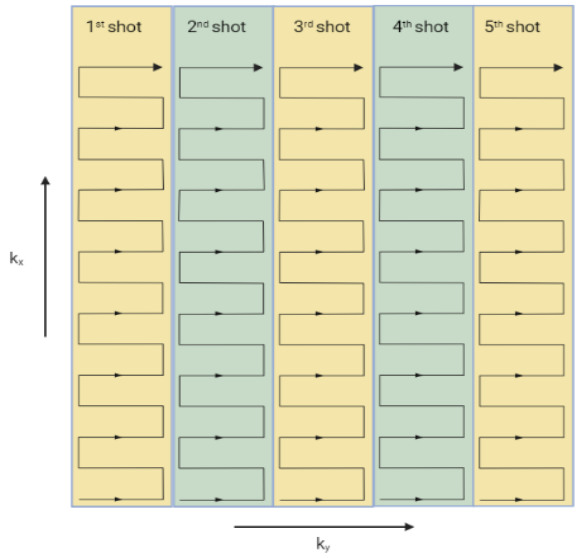

Figure 2.12: k-space trajectory for the RESOLVE sequence. Figure adapted from [23].

The RESOLVE sequence has shown significantly better image quality than SS-EPI for brain images, especially in brain regions where susceptibility effects are at their most severe, see figure 2.13. The imaged region, which is the base of the brain, is also particularly challenging for MS-DWI due to the high level of CSF pulsation, leading to large phase errors. The RESOLVE image shows a great reduction in susceptibility artifacts compared to the SS-EPI image, in addition to a greater level of anatomical detail without showing any artifacts as a result of the phase errors. The scan was performed on a 3T scanner.

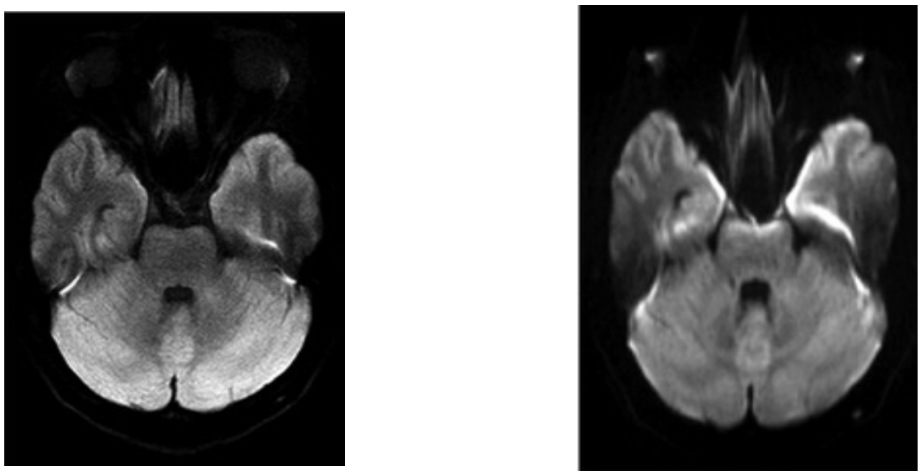

(a) (b)

Figure 2.13: The comparison between images of the base of the brain acquired with (a) RESOLVE and (b) SS-EPI. Both images are trace weighted images with b=1000 and GRAPPA used as the parallel imaging algorithm. Images retrieved from [23].

2.2 PET/MRI

All imaging in this project were performed on a combined PET/MRI scanner. Therefore, it is relevant to give a brief introduction to PET to give an idea of the advantages this imaging modality offers to justify why a combined PET/MRI scanner is used, and how the modalities affect each others acquisition and setup.

PET/MRI is a hybrid imaging technique that combines functional and molecular information from PET data with the soft tissue contrast of MRI. The PET and MRI data can be acquired simultaneously and PET/MRI is therefore an effective imaging technique. A fully integrated PET/MRI scanner is built up of a full body axial PET detector inside an MR scanner. It is important that the PET detector is MR compatible. With a combined scanner for PET and MR the problem with repositioning of the patient between different imaging modalities is eliminated. Therefore, the combination of images is much easier and the combined information gives increased accuracy in the delineation of tumor volumes.

PET is an imaging modality used to provide functional, molecular and anatomical information about the tumor volume. The technique uses the annihilation of a positron and an electron to locate a radiotracer. Radiotracers are radioactive compounds that are injected into the patient. Radiotracers used in PET decay through β^+ decay, which results in the formation of a positron. In PET there are several radioisotopes that can be used to investigate different properties of the tumor. The most commonly used isotope in PET-tracers is fluorine-18 ($[^{18}F]$). Positrons emitted from $[^{18}F]$ will move a distance of 2-3 mm before they encounter an electron. The encounter results in two photons with an energy of 511 keV and will travel in opposite directions. The PET detector is a ring full of many small photo sensors that will detect the incoming photons. By the detection of the two opposite traveling photons we can determine the position of the annihilation[24].

To be able to use the images acquired in a PET / MRI in RT planning, the patient must be positioned exactly the same way in the PET/MRI as on the linac. Therefore, the PET / MRI has a flat tabletop like the one in the linac, as well as coil holders for the MR receiver coils and thermoplastic masks to ensure reproducible positioning between imaging and treatment. This equipment is used in imaging of head and neck cancer. With the use of coil holders for the receiver coils, we ensure that there is no deformation of the patient's anatomy that can affect the delineation and at the same time the coils get close enough to yield a good signal. Since PET/MRI is a combined scanner, we must take into account how the equipment for the two imaging modalities will affect each other. One consequence is that the PET detector must be MR compatible. Regarding the PET signal, we see in figure 3.1 that there is a lot of equipment in the field of view (FOV). The PET signal is attenuated by everything inside the FOV and attenuation correction must therefore take all the equipment such as MR-coils, the coil setup and the mask into account in the attenuation map.

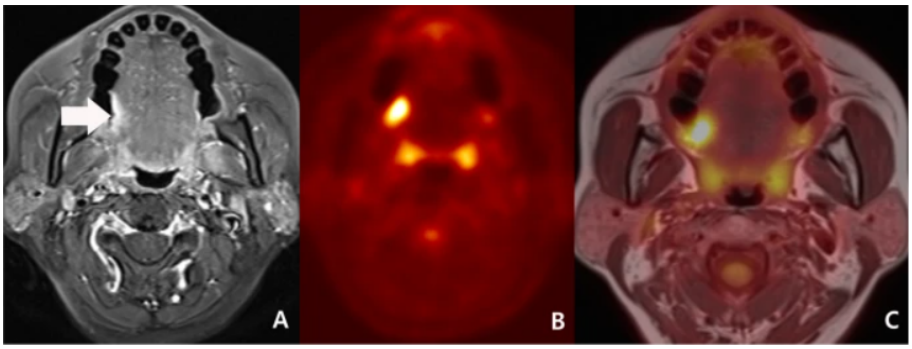

Figure 2.14: Imaging of a tongue cancer and metastasis. (A) Contrast enhanced MRI showing a lesion, see arrow. (B) PET reveals enhanced metabolism at the same area. (C) the combination of the two modalities can be used to give more precise diagnosis [25]

.

Chapter 3

Materials and Methods

In this project, MRI quality assurance (QA) was performed on three Siemens biograph mMR hybrid PET/MR scanners. The three scanners are located in the university hospitals in Tromsø, Trondheim and Bergen. Two different phantoms were used to acquire the measurements used for QA, the Diffusion Standard Model 128 for QA of DWI and the Large ACR (American College for Radiation) MRI phantom. The two phantoms differ both in appearance and in the measured parameters. Therefore, this chapter consists of two sections: one section focusing on the diffusion phantom and one section focusing on the ACR phantom.

3.1 Diffusion phantom

For the Diffusion Standard Model 128, hereby called the diffusion phantom, the QA process can be divided into three parts: phantom measurements, segmentation and image analysis, and data analysis using Python scripts. Each of these three parts will be presented in detail in this section. The method used in this project was in accordance with the *QIBA Profile: Diffusion-Weighted Magnetic Resonance Imaging (DWI))* [7].

3.1.1 Phantom measurements

For the DWI measurements, the Diffusion Standard Model 128 (High precision Devices - Caliber MRI, US) was used. The phantom consisted of 13 30 mL vials with a polymer solution. The concentration of polymer in each vial was different and a given concentration corresponds to a known ADC value at 0°C. To ensure a temperature of 0°C, the phantom was filled with ice water the night before the measurements and kept in a refrigerator. On the day of the measurements the ice water was changed with fresh ice water before the measurements started. The ice water was monitored by acquiring localizer images before, during and after the imaging sequences to ensure that the temperature was not rising above 0°C. As a general rule, the ice water was changed after one complete measurement with a coil setup.

The diffusion measurements consisted of two different sequences: 1) an EPI-based benchmark sequence, described in detail in the instructions for the diffusion phantom. 2) RESOLVE, a clinical sequence developed by Siemens and only available on their scanners. The RESOLVE sequence

is used clinically because it is largely free of distortions and delivers sharp images with reduced scanning time. The sequence is especially attractive for the evaluation of small lesions in DWI examinations [26]. The central settings for the two sequences are listed in table 3.1. The benchmark sequence included four different b-values in the range 0-2000 s/mm^2 while the RESOLVE sequence included four b-values in the range 0-800 s/mm^2. To be able to determine the short-term repeatability, each b-value image in both sequences was repeated four times.

Table 3.1: MRI-sequence parameters for the benchmark EPI sequence and the clinical RESOLVE sequence.

Parameter	Benchmark EPI sequence	Clinical RESOLVE sequence
FOV (mm^3)	216 x 216 x 214	216 x 216 x 214
Imaging plane	Transversal	Transversal
Slice thickness (mm)	4	4
TR (ms)	1000	4710
TE (ms)	102	73
Flip angle	90	180
b-values (s/mm^2)	0, 500, 900, 2000	0, 50, 100, 800
Acquired voxel size (mm)	5.1	5.1

The two sequences were performed in both a head and neck position and a pelvic position on the tabletop with and without an RT-setup. The RT-setup consisted of a hard tabletop, coil holders and flexible Body 6 receiver MR-coils, produced by Siemens. For image acquisition, the body coils were combined with the spinal coils integrated in the table in the scanner. The setups are shown in figure 3.1. The benchmark sequence was performed with both the RT-setup and the 16 channel diagnostic head coil from Siemens in the head and neck region. In the pelvic position, it was only performed with the RT-setup. The clinical sequence was only performed on the RT-setup in both the head/neck region and in the pelvic region. The phantom was oriented in a transversal orientation in the scanner, like the phantom in figure 3.1b.

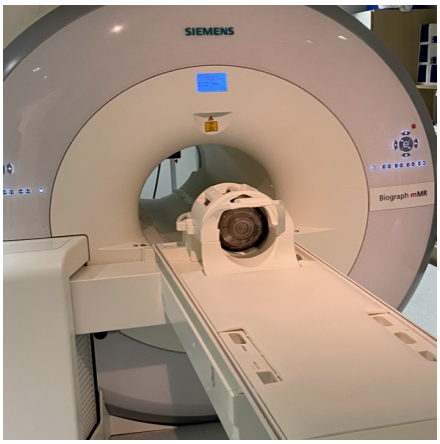

(a)

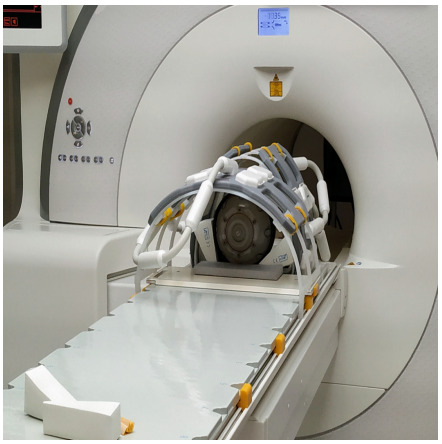

(b)

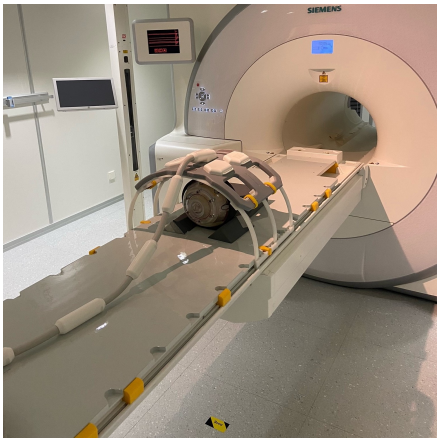

(c)

Figure 3.1: The figure shows (a) the 16-channel head coil from Siemens together with the RT-setups for the (b) head and neck position and (c) the pelvic position for the diffusion phantom scans.

Table 3.2: Summary of all DWI measurements.

Sequence (setup/position)	b-values (s/mm^2)	Signal averages per b-values
Benchmark (RT coil/head neck)	0, 500, 900, 2000	1, 2, 3, 2235
Benchmark (16 channel coil/head neck)	0, 500, 900, 2000	1, 2
Benchmark (RT coil/pelvic)	0, 500, 900, 2000	1, 2, 3, 2235
Clinical (RT coil/head neck)	0, 50, 100, 800	1, 2, 1123
Clinical (RT coil/pelvic)	0, 50, 100, 800	1, 2, 1123

In this project, an objective was to investigate whether increasing the number of signal averages influenced the accuracy of the ADC measurements and quantify the influence. The number of signal averages describes how many repeated scans that are used to calculate the average signal in the resulting image. The sequences were repeated with an increasing number of signal averages for increasing b-values. For the benchmark sequence on the RT-setup the images were acquired with 1, 2 and 3 signal averages for all b-values. In addition, one acquisition with 2, 2, 3 and 5 signal averages for 0, 500, 900 and 2000 s/mm^2, respectively, was acquired. In this last scan, the signal intensity in the images with b=0 and b=500 was averaged over two scans, images with b=900 averaged over 3 scans and images with b=2000 averaged over 5 scans. For the diagnostic 16-channel head coil, images are acquired with 1 and 2 signal averages for every b-value. For the

clinical sequence with the RT-setup the images are acquired with 1 and 2 signal averages for every b-value in addition to an acquisition with 1, 1, 2 and 3 signal averages for 0, 50, 100, 800 s/mm^2 respectively. Table 3.2 summarizes all scans.

A last scan was performed to investigate the influence on SNR of different RT-coil setups in a distance of 6 cm from the center of the RT-setup in the head and neck position, the phantom was moved inferiorly relative to patient laying head first in the scanner. The investigation of coil setup dependency inside the RT-setup was only done in the head and neck region. One scan was performed with both the head and neck coil active. In the other scan, only the head coil was active. This was done to determine the influence of the neck coil on the SNR value and was only done in Trondheim.

3.1.2 Segmentation and image analysis

The diffusion measurements are presented in table 3.2. For each measurement, four trace images were generated, one for each b-value, in addition to an ADC map calculated directly by the scanners software. All images were converted from DICOM to Nifty before further analysis. To be able to analyze the data from the vials, segmentation maps, later referred to as label maps, had to be made. Label maps were made in the image analyzer tool 3D Slicer. For each combination of coil setup and sequence, two label maps were made. The label maps were drawn in the central slice of the image stacks. The first label map contained only one segment, which is a circular region of interest (ROI) with a diameter of 15 mm in the central vial, see figure 3.2a. The other label map consisted of 13 circular regions with a diameter of 15 mm located in each of the 13 vials, see figure 3.2b. The phantom was not repositioned during the acquisition of images of a coil setup/sequence combination. Since all scans were performed in three centers, this resulted in a total of 15 pairs of label maps. The ROIs in the label map are used as masks in the scripts. This means that only the values inside the ROIs the script chooses will be used in the calculation.

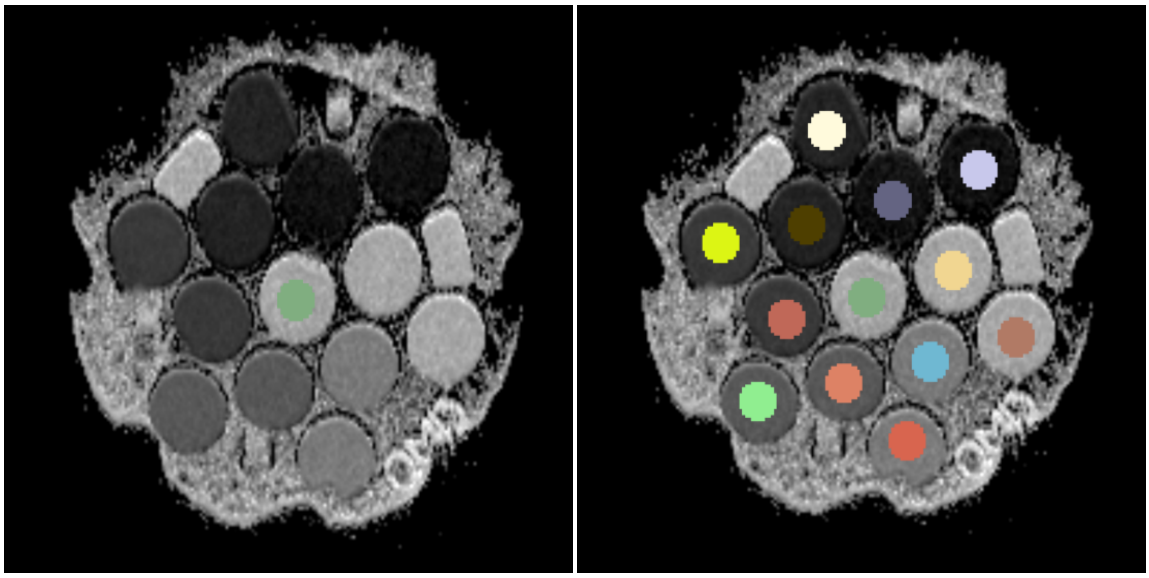

(a) (b)

Figure 3.2: The figure shows (a) the label map for the central vial close to the isocenter with an ROI with a diameter of 15 mm and (b) the label map for all 13 vials with 13 ROIs with a diameter of 15 mm. In the figure, the label maps are overlayed an EPI-image acquired in the RT-setup in the head and neck region.

The images and the label maps were imported into Python as nifty files after the segmentation. In Python the following parameters were calculated: ADC bias, error, short-term repeatability, reproducibility, SNR and ADC b-value dependence. The diffusion phantom manufacturer has developed a profile, later referred to as QIBA profile, that was used as a guideline for which parameters that were calculated[7]. The formulas to calculate the different parameters are presented below. The Python script used for the calculations is included in the appendix. All plotting of the results was done in Jupyter notebook using matplotlib, this code is not included.

The ADC bias ± 95 % confidence interval was calculated according to

$$ADCbias = (\mu - ADC_{ref}) \pm 1.96\frac{\sigma}{\sqrt{N}}, \tag{3.1}$$

where μ is the mean and σ is the standard deviation of the ROI, ADC_{ref} is the reference ADC value given by the QIBA profile. This parameter was evaluated in all 13 vials in the central slice of all scans. The bias can also be given in % and was calculated by dividing the bias with the reference ADC,

$$\%bias = \frac{(\mu - ADC_{ref})}{ADC_{ref}}. \tag{3.2}$$

The random measurement error, and precision, in an ROI were given as the coefficient of variation, %CV, in that ROI. The error was calculated for the central vial only and was calculated with the following formula,

$$\%CV = \frac{\sigma}{\mu} \cdot 100\%. \tag{3.3}$$

To determine short-term repeatability, the within-subject coefficient of variation, wCV, of the mean ADC value for the four repeated scans was calculated,

$$wCV = 100\% \cdot \frac{\sigma_4}{\mu_4}, \tag{3.4}$$

where μ_4 is the mean ADC value while σ_4 is the standard deviation of the mean ADC value for the 13 individual ROIs for the four repeated scans.

Reproducibility, also called variations between systems, was determined by calculating the %CV over the mean ADC values in the central ROI for the first of the four scans in the three centers [**kro**],

$$Reproducibility = \frac{\sigma_{3c}}{\mu_{3c}} \cdot 100\%, \tag{3.5}$$

where μ_{3c} is the mean and σ_{3c} is the standard deviation of the mean ADC value of the ROI in the first pass in the three centers [27].

SNR in the DWI was estimated as a temporal change in the pixel values in the central ROI through the four repeated scans. Due to parallel imaging, the SNR in a signal-free ROI in the background is unreliable in terms of DWI. Before the SNR calculation, all central ROIs were inspected to look for distortions and artifacts. If nothing was found, an image with the mean signal for each voxel was calculated, this was the *signal image* in the final calculation. Then an image with the temporal standard deviation between the four scans for each voxel was calculated, this was the *temporal noise image*. By calculating the spatial mean of these two images, the SNR could be calculated by using the following,

$$SNR = \frac{\text{Spatial mean of signal image}}{\text{Spatial mean of temporal noise image}}, \tag{3.6}$$

The 95% confidence interval for the SNR value can be calculated with,

$$CI_{SNR} = 1.96 \cdot SNR\sqrt{\frac{sCV^2 + nCV^2}{N}}, \tag{3.7}$$

where sCV and nCV are the spatial coefficient of variation in the ROI for the signal and the temporal noise image, respectively. N is the number of pixels in the ROI.

The diffusion phantom should have a monoexponential signal decay with increasing b-value, see equation (2.11). The b-value dependence was calculated to investigate if the choice of b-value influenced the ADC value measured. To investigate this, ADC-maps had to be calculated according to equation (2.14), this was done for 3 pairs of b-values where each pair consisted of b0 and a nonzero b-value. According to the QIBA profile, the difference in b-value between the two images had to be greater than 400 s/mm^2 to have sufficient contrast. Another requirement was that the minimum b-value was included in each pair, for the benchmark sequence the minimum b-value is 0. Because of these requirements, the b-value dependence was only calculated for the benchmark sequence. From the calculated ADC maps, a mean ADC b-value for the ROI was calculated. The

b-value dependence is calculated as,

$$\text{b-value dependence} = \left| \frac{ADC_{b_{min},b_1} - ADC_{b_{min},b_2}}{ADC_{b_{min},b_1}} \right| \cdot 100\%, \tag{3.8}$$

where ADC_{b_{min},b_1} and ADC_{b_{min},b_2} are the mean ADC values in the center vial in the ADC-maps calculated with b_0, and b_1 or b_2.

In the QIBA profile, the recommended values for the different parameters are listed. According to the profile, these values have to be fulfilled. The recommended values are listed in table 3.3.

Table 3.3: Threshold values given as requirements in the QIBA profile as requirements for the Diffusion Standard Model 128.

Parameter	QIBA requirement
ADC bias	$\leq$ 0.04 x 10^{-3} mm^2/s or 3.6 %
ADC error	$\leq$ 2 %
Short-term repeatability	$\leq$ 0.5 %
DWI SNR for b=0	$\geq 50 \pm 5$
b-value dependence	$<$ 2 %

3.2 ACR phantom

For the ACR phantom, the QA can be divided into two parts: phantom measurements and data analysis in MATLAB. Each part will be presented in this section. The method used in this section is in accordance with *ACR Large phantom Guidance*, hereby referred to as the ACR phantom profile, by the American College of Radiology (ACR) [8].

3.2.1 Phantom measurements

In this project the ACR Large Phantom was used to assess a broad specter of different measures. The measures are recommended by the ACR phantom profile. The phantom was a hollow cylinder of acrylic plastic, closed in both ends. The phantom was filled with 10 mM $NiCl_2$, 75 mM $NACl_2$. For the large phantom it was required that a sagittal localizer and two axial series of images, one T1-weighted and one T2-weighted, were acquired. In each of the axial series, all 11 slices in the phantom are imaged. The sagittal localizer and the 11 axial slices are presented in figure 3.3. The scan parameters are listed in table 3.4. Both the T1-weighted and the T2-weighted series are spin echo sequences. To compare the three centers, all three series were acquired in all centers with the same complete head and neck RT-setup with the same positioning inside the setup. The sequences were repeated in March, April and May on the scanner in Trondheim to assess the variation over time. To have the opportunity to compare the SNR values for two centers, a T1-weighted series consisting of two repeated scans was acquired in Tromsø and Trondheim. The ACR phantom profile does not have a recommended SNR value, but the SNR-values were calculated to evaluate possible differences between scanners and setups. The SNR value is a good measure for comparing image quality.

Table 3.4: Scan parameters for the three different series acquired for the ACR QA. The numbers in parentheses are parameters for the scan in march in Trondheim and the scan in Bergen.

Parameter	Sagittal localizer	T1-weighted series	T2-weighted series
FOV (mm^2)	250x250 (512X512)	250x250 (512X512)	250x250 (512X512)
Slice thickness (mm)	10	5	5
Gap (mm)	-	5	5
TR (ms)	200	500	2000
TE (ms)	20	20	80
Acquired pixel size (mm)	0.977 (0.489)	0.977 (0.489)	0.977 (0.489)

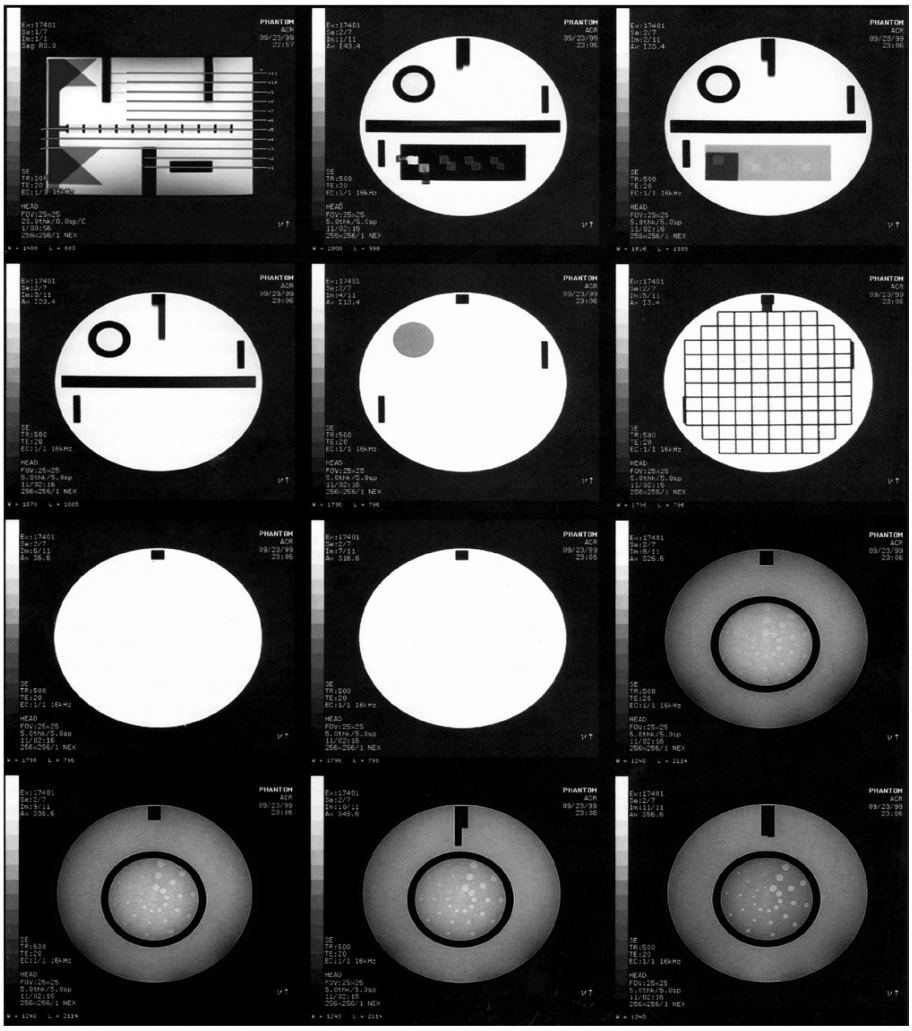

Figure 3.3: Image showing the sagittal localizer and the 11 axial slices for The ACR Large Phantom.

The influence on image quality of the positioning of the phantom in the head and neck setup was investigated as a part of the QA with the ACR phantom. This was done by repeating the scan for different positions relative to the center of the head and neck RT-setup in Tromsø. In this scan, the 0 cm position was set as the center of the head and neck RT setup. The phantom was then moved in 4 cm intervals for each measurement in the superior direction until the phantom was at a distance of 24 cm from the center, see figure 3.4c. This will be referred to as -24 cm. The phantom was then moved from the center, in 4 cm intervals, in the inferior direction until it was a distance of 32 cm from the center. This will be referred to as 32 cm, see figure 3.4d. The phantom

was scanned at different positions to evaluate the image quality at different positions. At each position, the T1-weighted axial series was acquired with two different RT-coil setups. One setup was a head coil setup where no neck coil was included, the other was a complete head and neck coil. This was chosen as the two setups to investigate the potential influence the neck coil had on the image quality. Relevant spinal coils, which were located in the table the patient lies on, was applied for all setups in all positions.

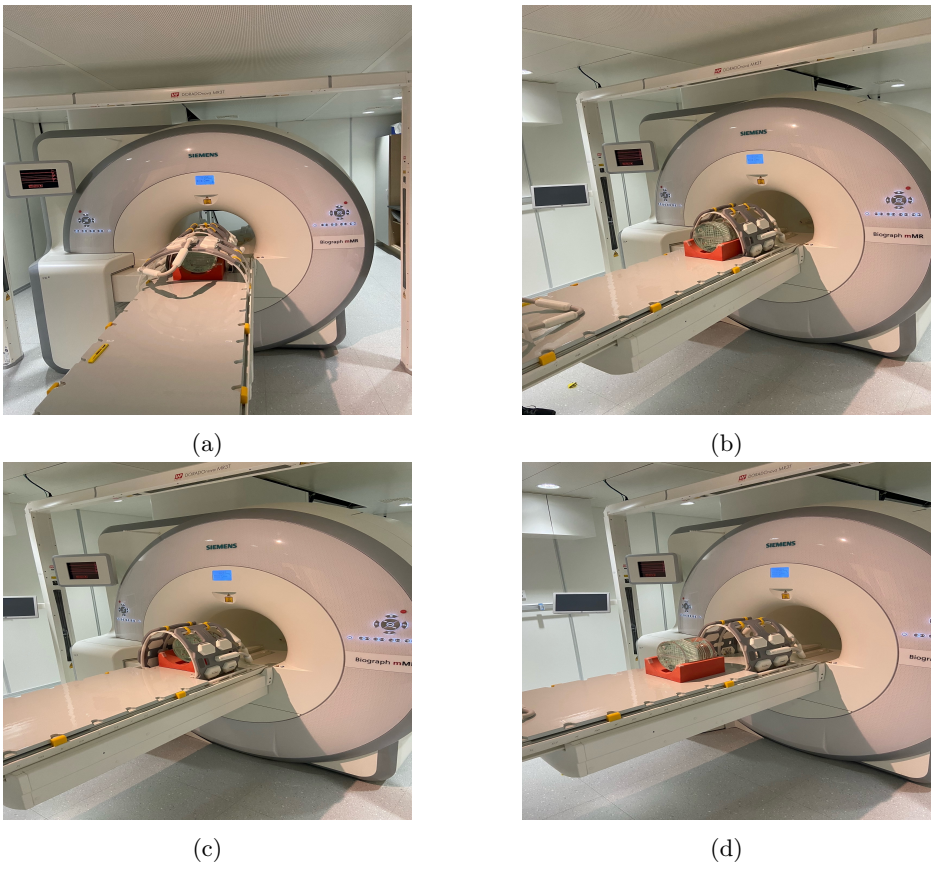

(a) (b)

(c) (d)

Figure 3.4: The figure shows (a) the full head and neck RT-setup with the ACR phantom positioned inside. (b) The 0 cm position imaged without the neck coil to easier see. (c) The -24 cm position and (d) the 32 cm position which is the extreme positions in superior and inferior direction, respectively, for the position varying scan in Tromsø.

3.2.2 Image analysis

The image analysis of the measurements of the ACR was done in MATLAB 2019b (The MathWorks, Inc., Natick, MA, USA) with a script developed for QA at St. Olavs. The script is written and used for QA by the staff at the PET-center. The MATLAB script imports all DICOM files directly and the different slices were used to calculate or determine the different parameters recommended in the ACR phantom manual [8]. The script calculates all the parameters required in the ACR phantom manual [8]. Table 3.5 lists the parameters calculated to perform the QA and the recommended value given in the manual. Each parameter calculation is explained in detail in the following. An explanation of the MATLAB code used in the calculation is included in the appendix. All plotting of the results was done in Jupyter notebook, the code for the plotting is not included.

Table 3.5: Threshold values given as requirements in the Large ACR phantom profile as requirements for Large ACR phantom.

Measure	ADC profile criterion
High contrast spatial resolution left to right (mm)	≤1.0
High contrast spatial resolution top to bottom (mm)	≤1.0
Slice thickness accuracy (mm)	5.0±1
Slice position accuracy slice 1 (mm)	≤5.0
Slice position accuracy slice 11 (mm)	≤5.0
PIU (%)	≥80
Ghosting ratio (%)	≤3
Low contrast detectability	≥37
SNR	-
Geometric accuracy	
Sagittal length (mm)	148±3
Anterior to posterior in slice 1 (mm)	190±3
Left to right in slice 1 (mm)	190±3
Anterior to posterior in slice 5 (mm)	190±3
Left to right in slice 5 (mm)	190±3
Upper right to lower left in slice 5 (mm)	190±3
Lower right to upper left in slice 5 (mm)	190±3

Geometric accuracy

The geometric accuracy of the scanner is of vital importance when using the scanner for the planning of RT-treatment, as the images are used to delineate both the tumor volume and the OARs. Relative to DWI, it was important to assess the geometric accuracy since EPI is prone to distortions due to phase accumulation. The geometric accuracy of the scanner was determined by measuring several distances in different slices and then comparing them with the values given by the phantom manual. These given values as well as the pass/fail criteria are given in table 3.5. The geometric accuracy was only assessed for the T1-series. The distance measurements were done automatically in the scripts. First the center of the phantom was determined, then an intensity profile in different directions was made, see figure 3.5. The next step was to use the twenty highest and twenty lowest values along this intensity profile to calculate the half maximum value. The water filled area in the phantom was much brighter than the surrounding air so the choosing of number of low and high values was not important. The distance measured was given as the distance between the first and last pixel with an intensity value higher than the half maximum value. The geometric accuracy was determined in several directions and slices. In the Sagittal localizer the accuracy of the superior to inferior length measure was determined. For both axial series the accuracy in the following directions and image slices was determined: anterior to posterior and left to right in slice one, and anterior to posterior, left to right, upper left to lower right, and lower left to upper right in slice five. All distances are visualized in figure 3.5.

(a) (b) (c)

Figure 3.5: Visualisation of the distances measured to assess the geometric accuracy for (a) the sagittal localizer, (b) slice one and (c) slice five.

High-contrast spatial resolution

The scanner's ability to resolve small objects when the contrast to noise ratio (CNR) is sufficiently high was tested with a visual inspection. Failure of this test means that the scanner was not resolving small details as well as it should. The test consisted of visual evaluation of three pairs of arrays that consisted of bright spots in image slice one of the axial series. The spots are water filled holes drilled into the plastic. Each pair of array consisted of an upper left (UL) and lower right (LR) array with four times four holes each. The three pairs of arrays had different sizes for the holes and the spacing between them. In the large phantom used in this project the three pairs of arrays had a size and spacing that are 1.1 mm 1.0 mm and 0.9 mm. The resolution was assessed in both top to bottom and left to right direction. First the resolution in the left to right direction was assessed by inspecting the UL array, starting with the left most pair of arrays. To be resolved, the holes in only one of the rows needed to be distinguishable. In the profile, distinguishable or resolved was said to be that it was possible to recognize the holes as points of higher intensity than the spacing between them. If the holes in the array with a hole size of 1.1 mm were resolved, the next pair of arrays was evaluated and so on. The score of the test was the minimum size of the holes in the array where the holes were still resolved. To assess the resolution in the top to bottom direction the procedure was similar, with the only difference being that in this test the holes in a single column in the LR-array needed to be resolved.

In figure 3.6 there are examples of resolved and unresolved holes to give some understanding of the assessment. In the UL-array in the rightmost pair of arrays, it is not possible to resolve the points in the top row, while the points in both the second and the third row are resolved. In the LR-array, the leftmost column is unresolved, while the next three columns are resolved.

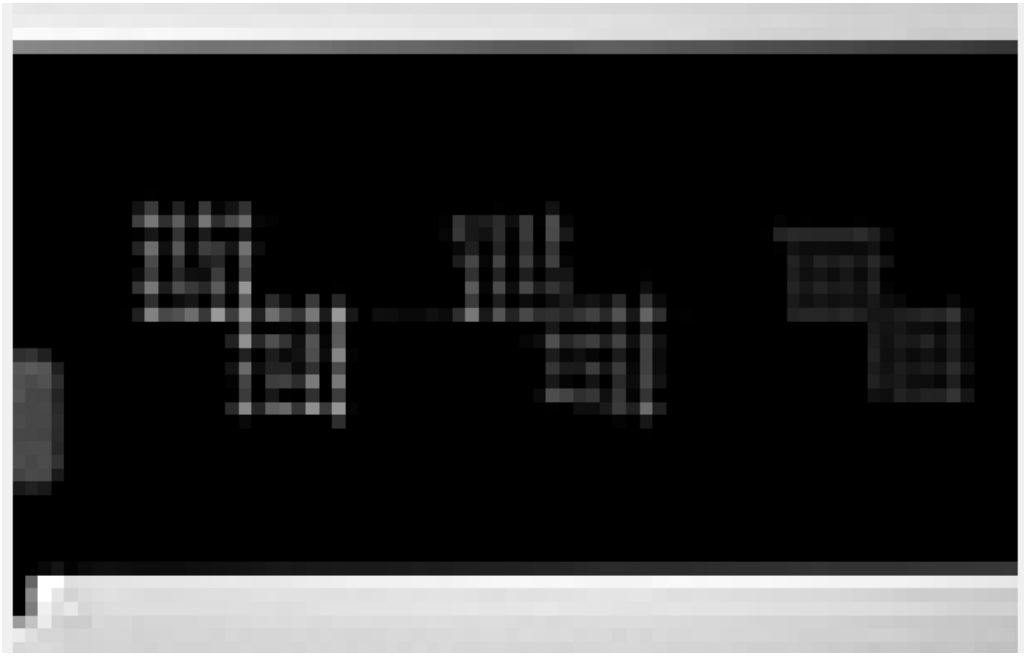

Figure 3.6: Image of the the arrays of holes in slice one used to assess the high contrast spatial resolution.

Slice thickness accuracy

This test was performed to assess whether the specified slice thickness was achieved. If the scanner had too low slice thickness accuracy, the image contrast could be decreased, as well as the SNR. The accuracy was assessed for both axial series. In this test, the lengths of two signal ramps in slice one were measured. The ramps were crossed, meaning that one of the ramps had a negative slope and the other had a positive slope with respect to the plane of the slice. Both ramps were filled with the same solution as the rest of the phantom. The two signal ramps had a slope of ten to one with respect to the plane of slice one. In that way, the ramps had an apparent length in slice one that was ten times the thickness of the slice.

To measure the width of the ramps, the same principle used in the geometric accuracy test was used. For each ramp the half maximum value for the ramp was calculated inside a placed ROI, in this calculation the 15 highest and lowest values in the ROIs were used. The distance from the leftmost pixel to the rightmost pixel on the ramp with an intensity value above the half maximum value was the measured width of the ramp. This was done for both ramps. Figure 3.7a shows the ROIs that was used for the measurement. The slice thickness was then calculated with the following formulae:

$$\text{Slice thickness} = 0.2 \cdot \frac{w_{r1} \cdot w_{r2}}{w_{r1} + w_{r2}}, \tag{3.9}$$

where w_{r1} and w_{r2} are the widths of ramp 1 and ramp 2, respectively, the factor 0.2 is a unitless factor that corrects for the rotation of the phantom about the vertical, y, axis.

Slice position accuracy

The objective of this test was to assess whether the slices were located in the prescribed positions. This was done using the localizer image as a reference for the actual position. The measure for this test was the difference between the prescribed and actual positions of slice one and eleven for

both axial series. Slice one and eleven were supposed to be aligned with the vertices of the crossed wedges at the inferior and interior ends of the phantom. This alignment was done before image acquisition. In the two slices the wedges appeared as two adjacent dark lines at the top of the phantom. If the slice was exactly aligned with the vertices, the two lines would have the same length but when the slice was displaced either inferiorly or superiorly with respect to the vertices, the length would differ. If the right bar was longer, the slices were mis-positioned superiorly while they were mis-positioned inferiorly if the left bar was longer. The measurement started by placing an ROI covering a part of the line and some of the water filled area and then calculating the half maximum value. For each of the lines, the first pixel with an intensity higher than the half maximum value, counted from top to bottom, was marked in red or blue, see figure 3.7b. The length difference in y-direction between the lines was then registered as the score for slice position accuracy.

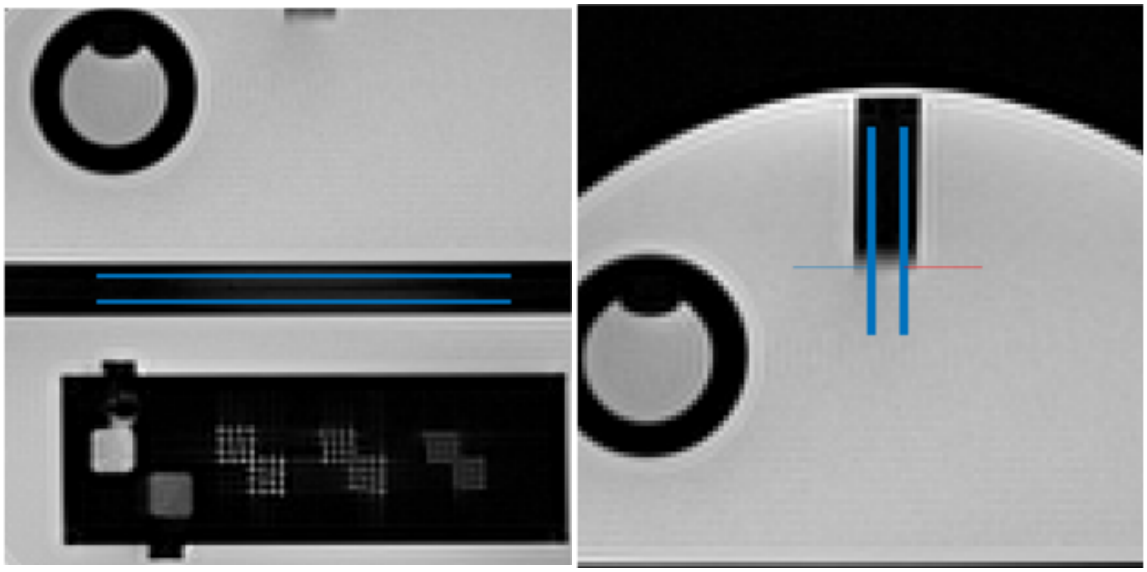

(a) (b)

Figure 3.7: Image visualising the ROIs used to calculate the (a) slice thickness accuracy and (b) slice position accuracy.

Image intensity uniformity

To test the intensity uniformity of the scanner, the uniformity of the image intensity in a large water-only region was assessed. A failure of the test can indicate a defective head and neck coil or a deficiency in the scanner. The test was done for both axial series in slice seven. In slice seven a large circular ROI (area of 200 cm^2) was placed in the center, so it included as much of the water-filled region as possible without including the wedges. To do the calculation two smaller ROIs were determined, one with the lowest mean intensity and one with the highest mean intensity, using the MATLAB script. The area of these ROIs was 1 cm^2. An example of the ROIs used can be seen in figure 3.8a. The image intensity uniformity was calculated with the following formulae,

$$PIU = 100 \cdot \left(1 - \frac{\mu_h - \mu_l}{\mu_h + \mu_l}\right), \tag{3.10}$$

where μ_l and μ_h is the mean intensity value in the ROI with low and high intensity.

Percent-signal ghosting

This test assessed the level of ghosting in the T1-axial series. If the scanner fails this test the ghosting artifacts are significantly higher than what is expected for a functional scanner, and the scanner could have a ghosting artifact well above the recommended limit. Ghosting is an artifact that gives faint copies of the object superimposed on the image, displaced from the actual position. In this test, the ghosting ratio was measured as a percentage of the signal level in the actual image. The measurements of this test were done in slice seven. The average signal intensity in five regions was measured, one region was in the water filled region in the center of the slice (area of 200 cm^2) and four regions were outside the phantom. The ROIs outside the phantom had an area of approximately 10 cm^2 and a width to length ratio of 1:4. The regions are shown in figure 3.8b. The ghosting artifact would only occur in the phase encoding direction in the sequence used for the ACR phantom. The two regions on the sides of the phantom could not have any ghosting artifact and were therefore used as control for the mean background intensity. The ghosting ratio was calculated with the following formula:

$$\text{ghosting ratio} = \left| \frac{(\mu_t + \mu_b) - (\mu_l + \mu_r)}{2 \cdot (\mu_c)} \right|, \tag{3.11}$$

where μ_t, μ_b, μ_l, μ_r is the mean signal intensity in the top, bottom, left and right rectangular ROI respectively. μ_t, μ_c is the mean signal intensity in the large ROI in the center.

Low-contrast detectability

The low contrast detectability (LCD) test assessed how well objects of low contrast could be distinguished from the background in the images. Failure of this test is closely related to the SNR, and generally a low score in the LCD test indicates low SNR. The measurements for this test were done in both axial series. The LCD-objects were located in slices 8-11 in both series. The objects appeared as disks in ten rows radiating from the center, see figure 3.8c. Each of these rows can be seen as spokes on a wheel and each spoke was made up of three disks. All disks in each slice had the same level of contrast, ordered from slice 8 to 11 these values are 1.4%, 2.5%, 3.6% and 5.1%. For each spoke, all disks had the same diameter but decreased spoke by spoke, starting with the largest diameter for the spoke at 12'o clock, hereby called spoke 1. Spoke 1 had disks with a diameter of 7.00 mm and the diameter was decreasing progressively to 1.5 mm for spoke 10. The score for this test was the number of complete spokes detected in the four slices. To be able to detect the spokes, the images had to be carefully adjusted. It was important that the counting of spokes started from spoke 1 and continued clockwise. There was examples of images where an incomplete spoke was followed by a complete spoke of smaller size. This spoke could not be counted and the test score was the last complete spoke before the first incomplete one.

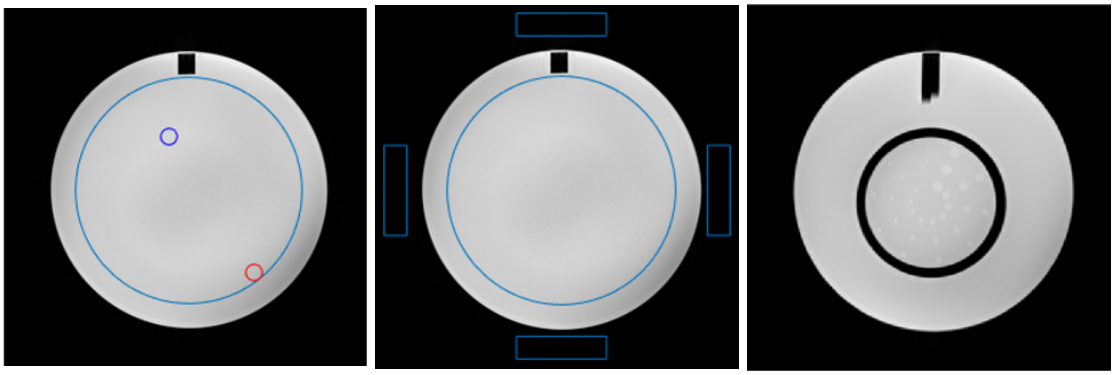

(a) (b) (c)

Figure 3.8: Visualization of the regions used for calculation of (a) image intensity uniformity, (b) ghosting, (c) low contrast detectability for the ACR QA.

SNR

SNR for the ACR measurements was calculated based the similar basic principles as the SNR in the diffusion analysis. The SNR was calculated to reveal possible differences between the centers but especially the different setups used in the scan in Tromsø. The images used for calculation were two repeated scans of slice seven of the T1-weighted axial series. In this slice a large ROI was placed in the center of the water-filled area, see figure 3.9. It was the pixels inside this ROI that was used in the SNR-calculation. A difference from the SNR calculation in the diffusion measurements was that the ACR scan only provided two repeated scans instead of four. The QIBA profile suggests to then use a different procedure to calculate the SNR than the one used for the SNR calculation in the diffusion measurements. In this procedure, the mean of the two images was the signal Image and a DIFF-image was made by subtracting the pixel value in the second image from the first one. The following formula was then used to calculate the SNR,

$$SNR = \frac{\text{Spatial mean pixel value of signal image}}{\text{Spatial standard deviation pixel value on DIFF image}}. \tag{3.12}$$

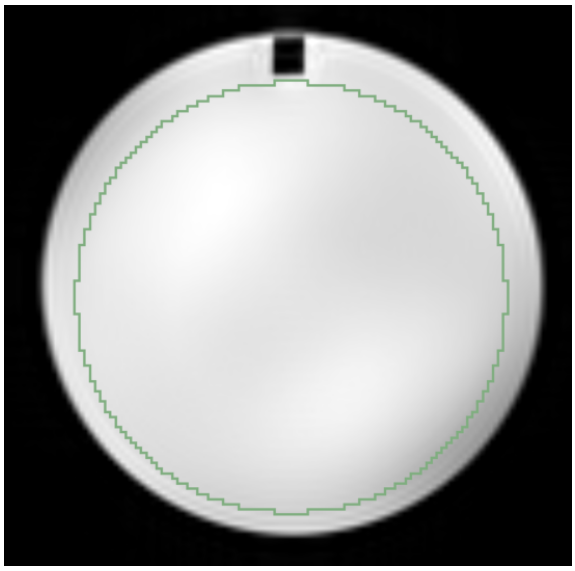

Figure 3.9: Image showing the ROI in slice seven which includes the pixels used to calculate SNR for the ACR QA.

Chapter 4

Results

This chapter is divided into two parts, one focusing on the results from the diffusion measurements and one focusing on the ACR measurements.

4.1 Diffusion phantom

For the diffusion phantom, the measures varied between scanners, coil setups, sequences and between repeated scans, but the general impression is that the variations are relatively small. The results presented in this section are the measures from the scans with one average if nothing else is stated. The short-term repeatability is a measure of the variation between repeated scans. The other measures are the results of the first pass in each measurement. Each scan was repeated four times. The pass number refers to which of these four scans that was analyzed.

Regarding the ADC-bias, all ADC-bias values measured for the center vials were within the QIBA recommendations for all centers, coil setups and sequences. Table 4.1 shows that The Trondheim scan had the highest |ADC bias| of the three centers for all combinations of setup and sequence, but still well within the criterion. The results for the 16-channel diagnostic coil are presented in figure 4.1a. Figure 4.2a and 4.3a shows the ADC-bias values for the benchmark sequence for head and neck and pelvic RT-setup, respectively. The results for the clinical sequence are presented in figure 4.2b for head and neck RT-setup and in figure 4.3b for pelvic RT-setup.

Table 4.1: The ADC-bias results for the the three centers for both sequences and the three different coil setups. All ADC bias values given in x10^{-3} mm^2/s

	Tromsø	Trondheim	Bergen
Benchmark sequence			
Head neck RT-setup	-0.0124 (± 0.0094)	-0.0209 (± 0.0089)	0.0013 (± 0.0092)
Pelvic RT-setup	-0.0120 (± 0.0104)	-0.0215 (± 0.0072)	0.0143 (± 0.0073)
16-channel head coil	-0.0168 (± 0.0050)	0.0218 (±0.0040)	-0.0115 (± 0.0036)
Clinical sequence			
Head neck RT-setup	0.0020 (± 0.0056)	-0.0158 (± 0.0041)	-0.0063 (± 0.0067)
Pelvic RT-setup	0.0008 (± 0.0041)	-0.0209 (± 0.0040)	-0.0163 (± 0.0046)

The error in the ADC value measurements was calculated for the first pass for the scans with

only one signal average. Table 4.2 presents these results. None of these scans met the QIBA error criterion, which is error≤2% . By increasing the number of signal averages for the scans, the error was improved. Note that the plots of the error in figures 4.1, 4.2 and 4.3 present the error as the mean error for the four passes for each different measurement. The improvement presented in the following is therefore the improvement for this mean error. Figures 4.2c and 4.3c present the improvement in error value when the number of signal averages was increased for the benchmark sequence for head and neck RT-setup and pelvic RT-setup, respectively. In the benchmark sequence, the greatest improvement of mean error was achieved, especially when increasing from one to two signal averages. For head and neck RT-setup the improvement was from 5.42 % to 3.7% in Tromsø, from 4.96 % to 3.39% in Trondheim and from 5.2 % to 3.69% in Bergen. For pelvic RT-setup the improvement was from 5.43% to 3.78% in Tromsø, from 4.03% to 2.78% in Trondheim and from 3.53% to 2.58% in Bergen. The change in error for an increasing number of signal averages for the clinical sequence is presented in figure 4.2d for the head and neck RT-setup and in figure 4.3d for the pelvic RT-setup. For the diagnostic coil setup the error improved with 2 signal averages compared with 1, but the improvement was not as clear as in the head and neck and the pelvic setup. This can be seen in the plot in figure 4.1b.

Table 4.2: Error in the ADC value measurements for the QIBA Diffusion Phantom QA.

	Tromsø	Trondheim	Bergen
Benchmark sequence			
Head neck RT-setup	5.07 %	4.78 %	4.87 %
Pelvic RT-setup	5.57 %	3.89 %	3.84 %
16-channel head coil	2.67%	2.1%	1.95%
Clinical sequence			
Head neck RT-setup	2.94%	2.2%	3.55%
Pelvic RT-setup	2.19%	2.17%	2.46%

The results for short-term repeatability for both sequences in the three centers are presented in table 4.3. The table shows that all measurements had a %wCV≤ 0.5%, which means that all of them fulfilled the QIBA recommendations. The result for short-term repeatability calculation for each of the 13 vials for the benchmark sequence is presented in 4.2e and 4.3e for the head and neck RT-setup and the pelvic RT-setup, respectively. Figures 4.2f and 4.3f present the results of the clinical sequence. All these figures show the result for scans with only one signal average.

Table 4.3: Short term repeatability (%vCW) results for the QIBA Diffusion Phantom QA.

	Tromsø	Trondheim	Bergen
Benchmark sequence			
Head neck RT-setup	0.28%	0.41%	0.48 %
Pelvic RT-setup	0.16%	0.26%	0.45%
16-channel head coil	0.09%	0.23%	0.24%
Clinical sequence			
Head neck RT-setup	0.2%	0.37%	0.16%
Pelvic RT-setup	0.17%	0.22%	0.22%

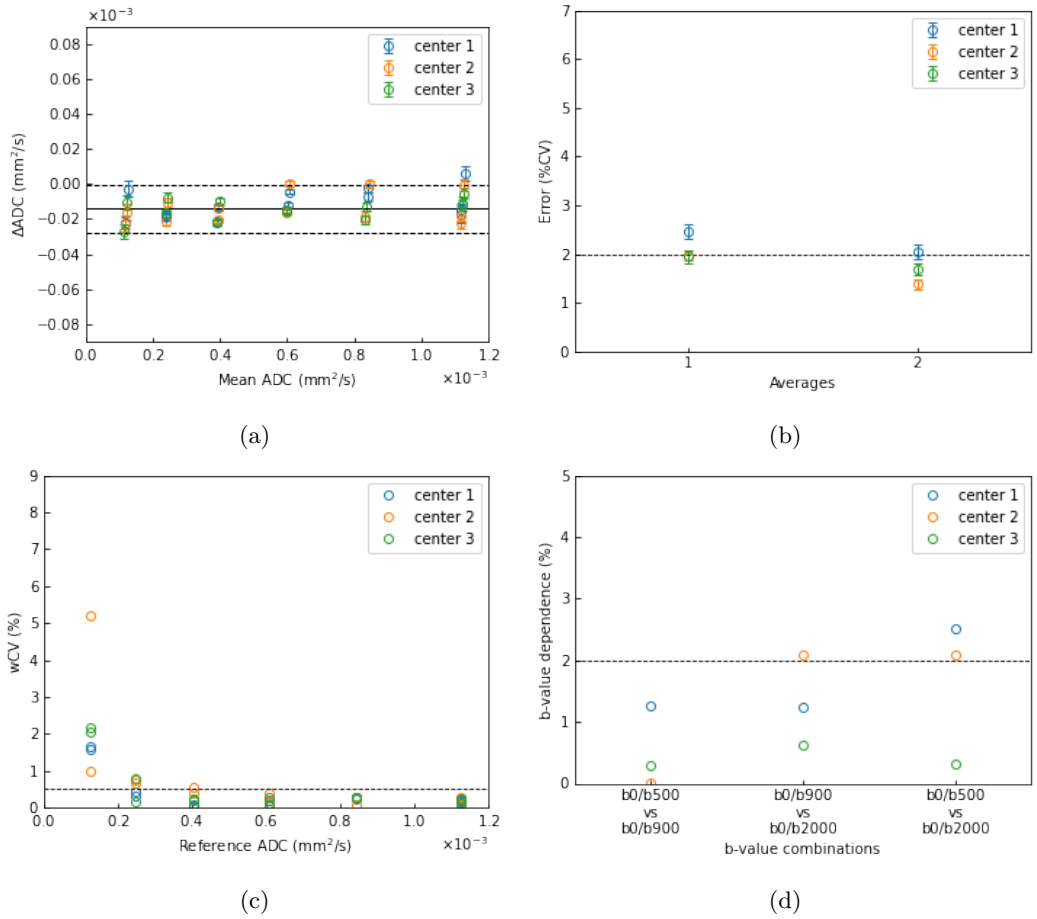

Figure 4.1: ADC measures for the scanners in Tromsø (center 1), Trondheim (center 2) and Bergen (center 3) for the diagnostic 16-channel head coil and the benchmark sequence. (a) ADC-bias for all 13 vials in the diffusion phantom. The center solid line represents the ADC-bias mean and the dotted lines represent the 95% confidence interval. (b) ADC error plotted against number of signal averages. The dashed line represents the QIBA criterion of 2%. (c) Short term repeatability (%wCV) for all 13 vials. The dotted line represents the QIBA criterion of 0.5%. (d) The b-value dependence on the measured ADC value. The x-axis shows different b-value pairs used to calculate the ADC-maps which the b-value dependence is calculated for. The dashed line is the QIBA criterion of 2%.

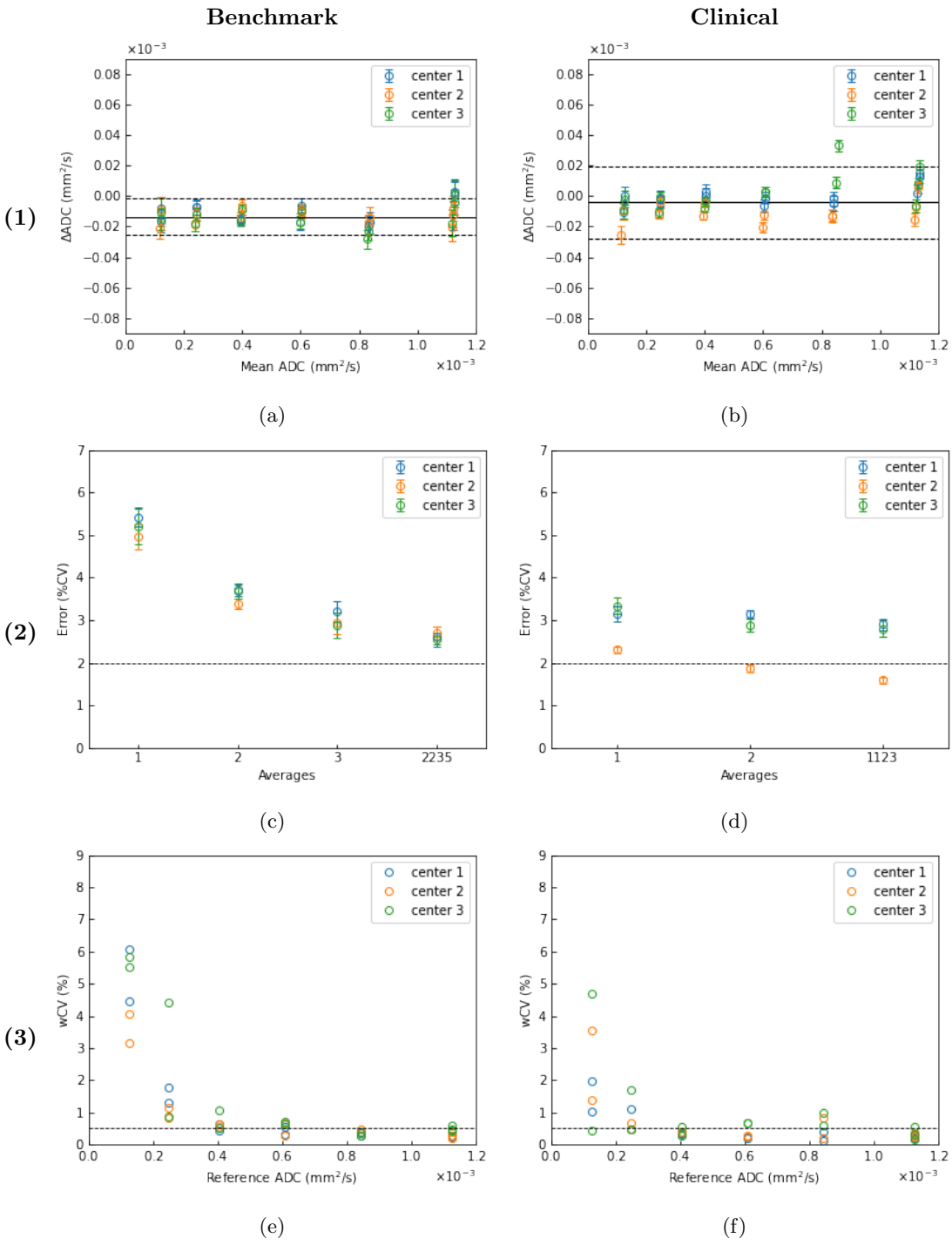

Figure 4.2: ADC measures for the scanners in Tromsø (center 1), Trondheim (center 2) and Bergen (center 3) for the head and neck RT-setup. The left columns is the results from the benchmark sequence and the right column shows the results from the RESOLVE sequence. (1) ADC-bias for all 13 vials in the diffusion phantom. The center solid line represents the ADC-bias mean and the dotted lines represent the 95% confidence interval. (2) ADC error plotted against number of signal averages. The dashed line represents the QIBA criterion of 2%. (3) Short term repeatability (%wCV) for all 13 vials. The dotted line represents the QIBA criterion of 0.5%.

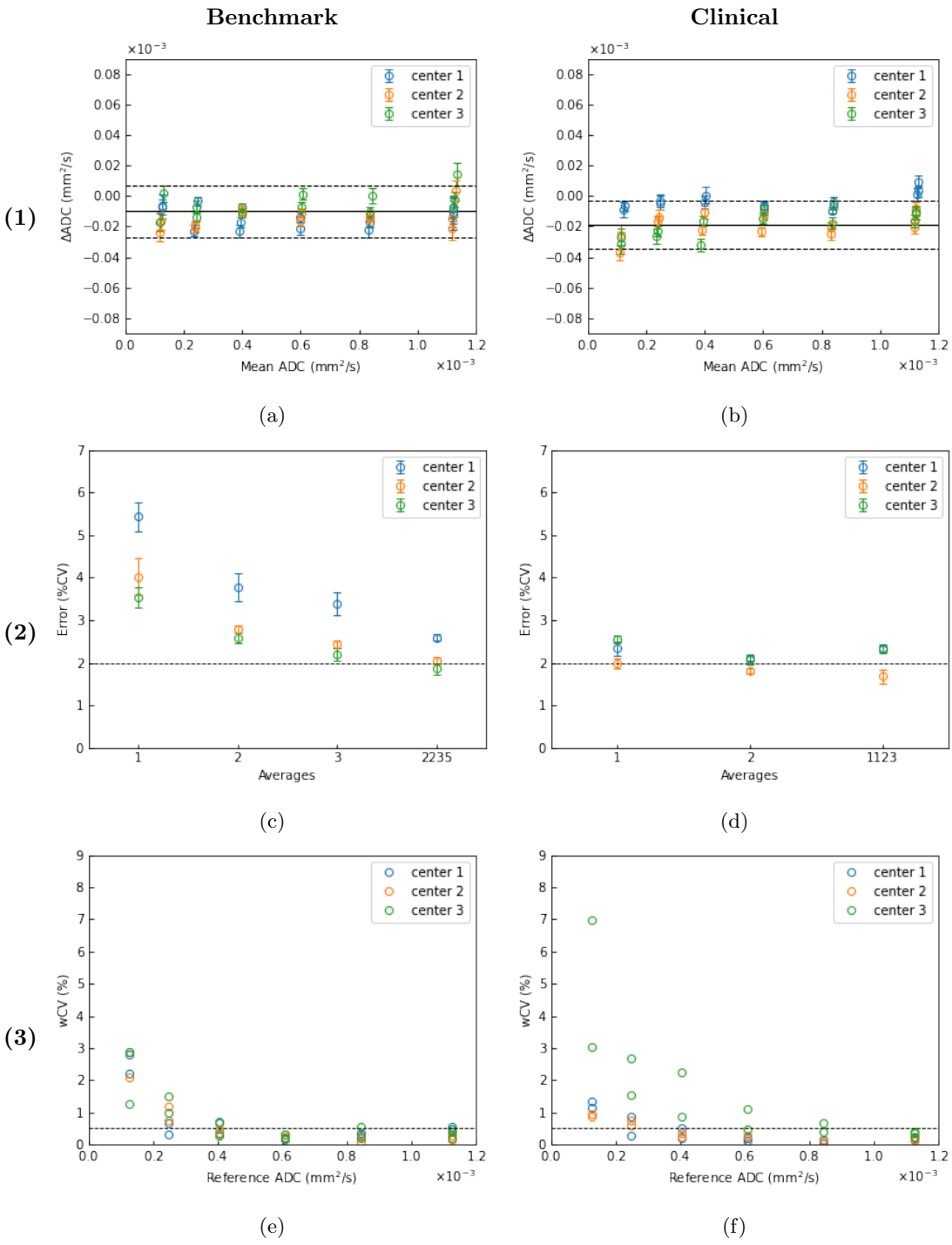

Figure 4.3: ADC measures for the scanners in Tromsø (center 1), Trondheim (center 2) and Bergen (center 3) for the pelvic RT-setup. The left column is the results from the benchmark sequence and the right column shows the results from the RESOLVE sequence. (1) ADC-bias for all 13 vials in the diffusion phantom. The center solid line represents the ADC-bias mean and the dotted lines represent the 95% confidence interval. (2) ADC error plotted against number of signal averages. The dashed line represents the QIBA criterion of 2%. (3) Short term repeatability (%wCV) for all 13 vials. The dotted line represents the QIBA criterion of 0.5%.

By increasing the number of signal averages, the short-term repeatability for the scans was affected. The effect was different for the different sequences and the effect also varies between scanners. For the benchmark sequence, an increase of the signal averages lead to a decrease of the %wCV in a

majority of the scans in all centers, this was the case for both RT-setups, as well as the 16-channel diagnostic head coil. For the clinical sequence, an increasing number of signal averages lead to a increase of the%wCV of varying degree in the head and neck RT-setup. For the pelvic RT-setup the variation of %wCV for increasing number of signal averages was small. The results are presented in Table 4.4.

Table 4.4: Short-term repeatability, %wCV, for increasing number of signal averages for the two sequences and the different setups.

		Number of of signal averages			
Benchmark sequence		1	2	3	2235
Head and neck RT-setup	Tromsø	0.28%	0.23%	0.24%	0.17%
	Trondheim	0.41%	0.19%	0.18%	0.12%
	Bergen	0.48%	0.45%	0.34%	0.26%
Pelvic RT-setup	Tromsø	0.16%	0.24%	0.15%	0.14%
	Trondheim	0.26%	0.23%	0.19%	0.15%
	Bergen	0.45%	0.30%	0.23%	0.18%
16-channel head coil	Tromsø	0.09%	0.06%	-	-
	Trondheim	0.23%	0.14%	-	-
	Bergen	0.24%	0.07%	-	-
Clinical sequence		1	2	1123	
Head and neck RT-setup	Tromsø	0.20%	0.24%	0.39%	
	Trondheim	0.37%	0.42%	0.56%	
	Bergen	0.16%	0.73%	0.90%	
Pelvic RT-setup	Tromsø	0.17%	0.18%	0.21%	
	Trondheim	0.22%	0.18%	0.18%	
	Bergen	0.22%	0.20%	0.28%	

The b-value dependence of the ADC value measured was only calculated for the benchmark sequence. The results show that the b-value dependence is clearly bigger in Trondheim for two of the b-value pairs while for the pairs b (0, 900) and b (0, 2000) the difference is smaller. All b-value dependencies are regardless well below the QIBA criterion of 2%.

b-value combinations	**Setup**	Tromsø	Trondheim	Bergen
(0, 500) and (0, 900)	Head and neck RT-setup	0.52%	1.02%	0.29%
	Pelvic RT-setup	0.12%	0.97%	0.08%
	16-channel head coil	1.26%	0.01%	0.29%
(0, 900) and (0,2000)	Head and neck RT-setup	0.61%	0.36%	0.62%
	Pelvic RT-setup	0.26%	0.14%	0.55%
	16-channel head coil	1.25%	2.02%	0.62%
(0, 500) and (0, 2000)	Head and neck RT-setup	1.13%	1.39%	0.33%
	Pelvic RT-setup	0.15%	1.1%	0.47%
	16-channel head coil	2.50%	2.03%	0.33%

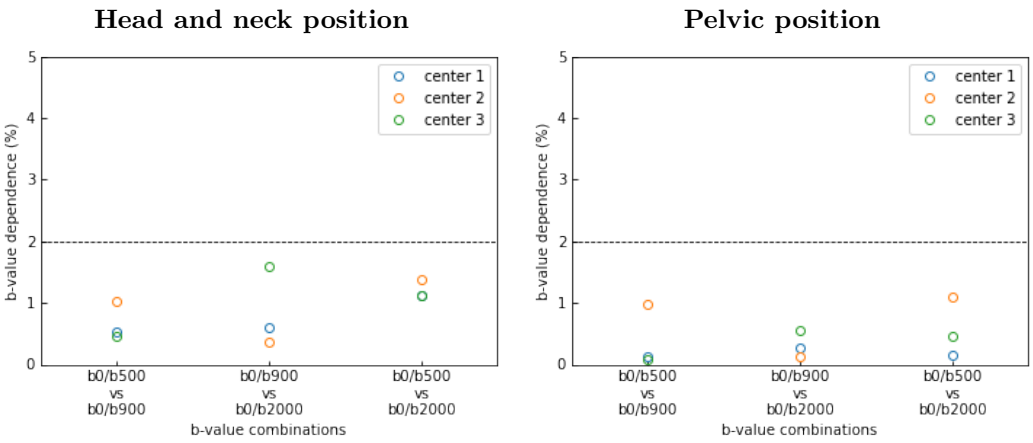

Figure 4.4: b-value dependence results for the benchmark sequence for the scanners in Tromsø (center 1), Trondheim (center 2) and Bergen (center 3). The left plot is the result with the head and neck RT-setup, while the right plot is the result with pelvic RT-setup. The x-axes shows different b-value pairs used to calculate the ADC-maps which the b-value dependence is calculated for. The dashed line is the QIBA criterion of 2%.

The QIBA profile has no required value for reproducibility, but reproducibility can give a measure of how much measurements varies between the scanners in the different centers with the same sequence and setup. The reproducibility for the diagnostic 16-channel head coil was 0.379%. For the benchmark sequence the reproducibility was 0.821% and 1.353% for head and neck RT-setup and pelvic RT-setup, respectively. For the clinical sequence the reproducibility was 0.647% and 0.836% for head and neck RT-setup and pelvic RT-setup, respectively.

For the benchmark sequence the SNR decreased with increasing b-value for both RT-setups in all three centers, as expected. The decrease in SNR was most evident from b500 to b900 and further from b900 to 2000. From b0 to b500 the decrease was minimal. Comparing the two RT-setups showed that both setups yield similar SNR-values. The QIBA criterion of an SNR of 50 for b0 was fulfilled in all three centers in both the head and neck RT-setup as well as the pelvic RT-setup. The SNR-value measured with the diagnostic 16-channel head coil was clearly higher compared with the head and neck RT-setup. In Tromsø, the diagnostic 16-channel coil showed an increase in SNR with a factor of 3 compared with the head and neck RT-setup for the benchmark sequence. The increase in SNR-value with the diagnostic coil was similar in Bergen but clearly lower in Trondheim.

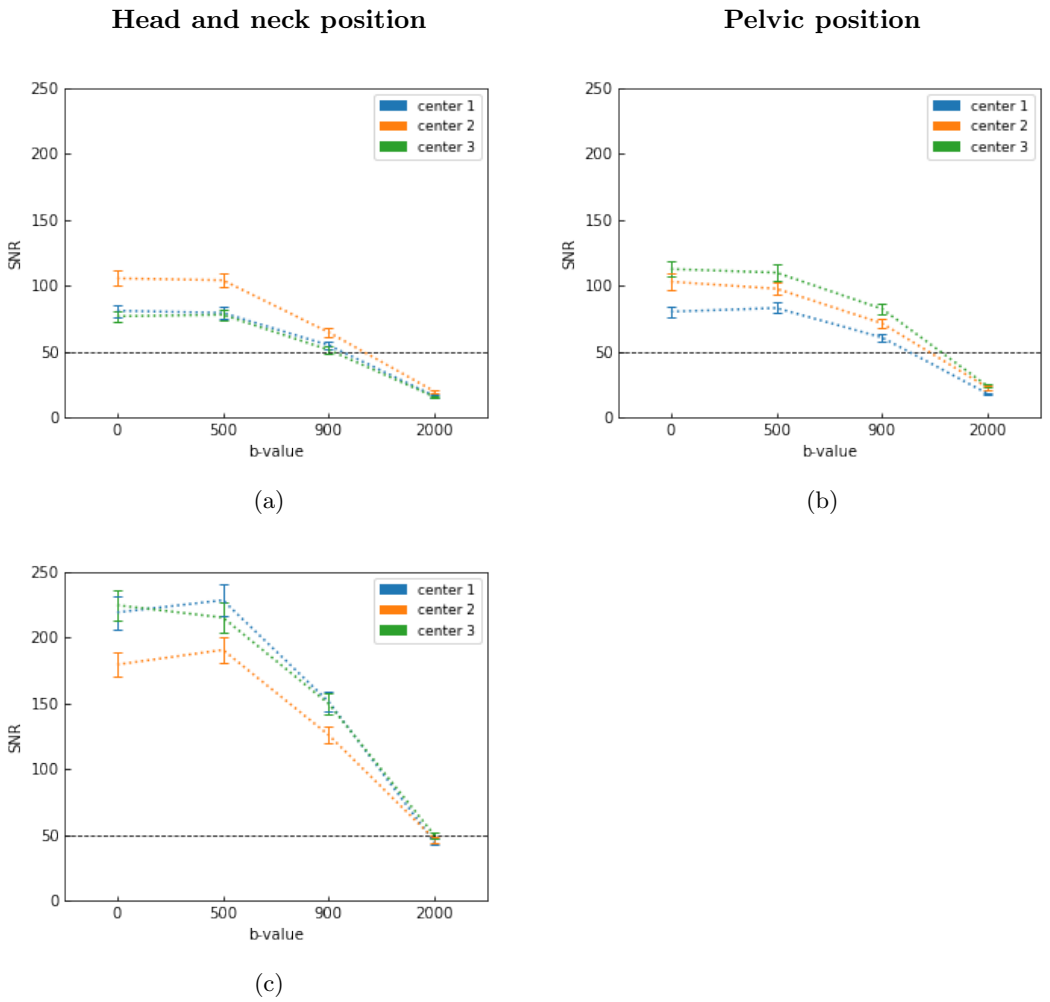

Figure 4.5: SNR values achieved for the images acquired with benchmark sequence in Tromsø (center 1), Trondheim (center 2) and Bergen (center 3) for different b-values. (a) Presentation of the SNR values with the head and neck RT-setup, (b) is the result with pelvic RT-setup. (c) SNR values for the diagnostic 16-channel head coil. The dashed lines represent the QIBA criterion for the SNR value, which is 50 for the b0 images.

The measurements in a head and neck coil setup versus a setup with only the head coil active showed an increased SNR for both the benchmark sequence and the clinical sequence, see figure 4.6. This increase in SNR-value was present for all b-values while the degree of increase varies between the benchmark and the clinical sequence. For the benchmark sequence, none of the b-values images with only head coil active fulfill the QIBA criterion of a SNR of 50 but b0 and b50 are close to fulfilling the criterion. The addition of the neck coil increased the SNR-values. All b-value images acquired with the complete head and neck setup except b2000 satisfy the QIBA recommendation.

For the clinical sequence, all b-value images fulfill the QIBA criterion with only head coil RT-setup and complete head and neck RT-setup. The SNR value is higher for all measurements acquired with the clinical sequence compared to the benchmark sequence. The b0 image acquired with the clinical sequence showed an increased SNR value compared to the benchmark sequence with a factor of 1.7 with the complete head and neck setup.

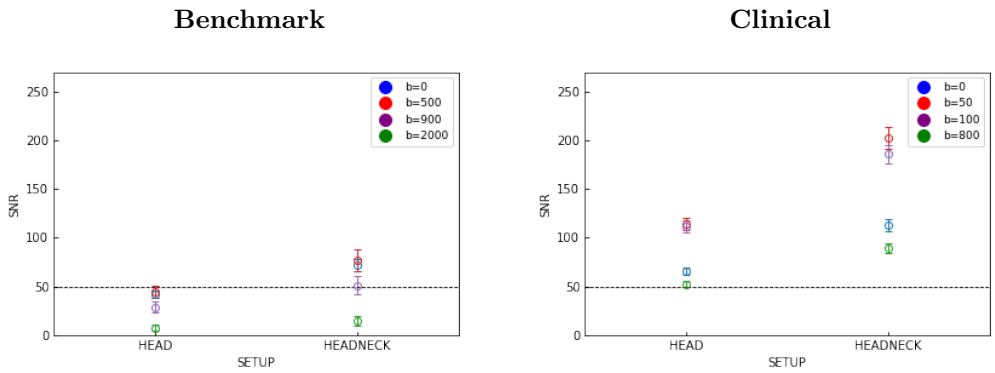

Figure 4.6: SNR values for the four different b-values for the scans in Trondheim. The plots compare the SNR-value achieved when using both head and neck RT-coils versus only using the head coil. The left plot shows the results for the Benchmark sequence while the right plot shows the clinical sequence. The dashed lines represent the QIBA criterion for the SNR value, which is 50 for the b0 images.

4.2 ACR-phantom

The different ACR measures mentioned in the ACR phantom manual did vary to various extent between the difference scanners. Almost without exception, the measures all fulfill the criteria given in the manual. In this section, the results from the intercenter comparison will be presented first, then the results from the position and coil setup varying scan in Tromsø are presented. At last the results for the three time repeated scan in Trondheim are presented.

Geometric accuracy was assessed in all required directions in the first and fifth image slices for the T1-weighted series. All scanners have a geometric accuracy within the criterion of 190 mm ±3 given by the manual. The geometric accuracy results are presented in table 4.5 together with figure 4.7g. As the table shows, all centers show similar results. Only the plot for anterior to posterior in slice one is included in the figure.

High contrast spatial resolution is assessed in both axial series. All scanners have a resolution within the criterion in both top to bottom direction and left to right direction. The resolution is better in the T2 series than the T1-weighted series for the scanners in Tromsø and Bergen while it is equally good in Trondheim, see table 4.5 and 4.6, and figure 4.7c and 4.7c. Only the plot for the left to right resolution is included in the figure.

Slice position accuracy is assessed for both axial series. All scanners have a slice thickness accuracy which is in the required range, see figure 4.7d, 4.8d, 4.7e and 4.8e. Table 4.5 shows that the results are positive for slice one and negative for slice eleven. The negative sign means that the bar on observers left is longer than the bar at observers right and that the slice is misplaced inferiorly. The results show that slice eleven tends to be misplaced inferiorly while slice one is misplaced superiorly. The criterion to pass this test is that the length difference is below 5.0 mm but there is recommended that the difference is not higher than 4 mm. All scanners fulfill this recommendation as well. Note that it is the absolute value of the slice position accuracy for slice eleven that is plotted in the following.

The image intensity uniformity is assessed for slice seven in both axial series. The only result for PIU that does not fulfill the criterion is the PIU for the T1-weighted series in Trondheim, where the PIU is 79.1%. All other PIU values are greater than or equal to 80%, as figures 4.7b and 4.8b show. Visual investigation of low contrast detectability showed adequate quality for all three centers for both axial series. The number of complete spokes detected was 38 for Tromsø and Trondheim while it was 37 for the images from Bergen. For the T2-weighted series the result was similar, see table 4.6 and figure 4.8a . Both series in all three centers are fulfilling the criterion of minimum 37 complete spokes detected.

All scanners showed a very low degree of ghosting artifact for the T1-weighted series. The ghosting ratio was 0.27%, 0.08% and 0.15% for Tromsø, Trondheim and Bergen. All these values are well below the required ghosting ratio of 3% given in the manual.

The ACR manual does not have a criterion for the SNR value, but it is included to get an idea on how the centers compare, especially when all the data from different positions and setups are available from Tromsø. The SNR value was found to be clearly higher at the Tromsø scanner than at the Trondheim scanner. The SNR value for the T1-weighted repeated scan in Tromsø was 739 while the SNR in Trondheim was 565.

Table 4.5: Results for the QA of the T1-weighted series performed in the three centers with the ACR phantom.

Measure	Criterion	Tromsø	Trondheim	Bergen
High contrast spatial resolution left to right (mm)	≤ 1.0	0.9	1.0	1.0
High contrast spatial resolution top to bottom (mm)	≤ 1.0	0.9	1.0	1.0
Slice thickness accuracy (mm)	5.0±1	4.88	5.72	5.03
Slice position accuracy slice 1 (mm)	≤ 5.0	0.98	1.45	3.90
Slice position accuracy slice 11 (mm)	≤ 5.0	-2.92	-3.90	-1.95
PIU (%)	≥ 80	91.15	**79.13**	95.50
Ghosting ratio (%)	≤ 3	0.27	0.09	0.15
Low contrast detectability	≥ 37	38	37	38
SNR	-	739	565	-
Geometric accuracy				
Sagittal length (mm)	148±3	146.97	146.48	146.48
Anterior to posterior in slice 1 (mm)	190±3	191.41	189.94	190.43
Left to right in slice 1 (mm)	190±3	192.38	190.92	188.48
Anterior to posterior in slice 5 (mm)	190±3	190.43	189.45	190.43
Left to right in slice 5 (mm)	190±3	190.43	189.94	188.48
Upper right to lower left in slice 5 (mm)	190±3	189.21	188.52	188.52
Lower right to upper left in slice 5 (mm)	190±3	190.59	189.21	189.21

Table 4.6: Results for QA of the T2 axial series performed on the ACR phantom in the three centers.

Measure	Criterion	Tromsø	Trondheim	Bergen
High contrast spatial resolution left to right (mm)	≤ 1.0	0.9	0.9	0.9
High contrast spatial resolution top to bottom (mm)	≤ 1.0	0.9	0.9	0.9
Slice thickness accuracy (mm)	5.0 ±1	4.70	4.56	5.64
Slice position accuracy slice 1 (mm)	≤ 5.0	-0.49	2.44	3.91
Slice position accuracy slice 11 (mm)	≤ 5.0	-3.91	-2.93	-1.46
PIU (%)	≥ 80	80.39	93.55	95.36
Low contrast detectability	≥ 37	38	38	37

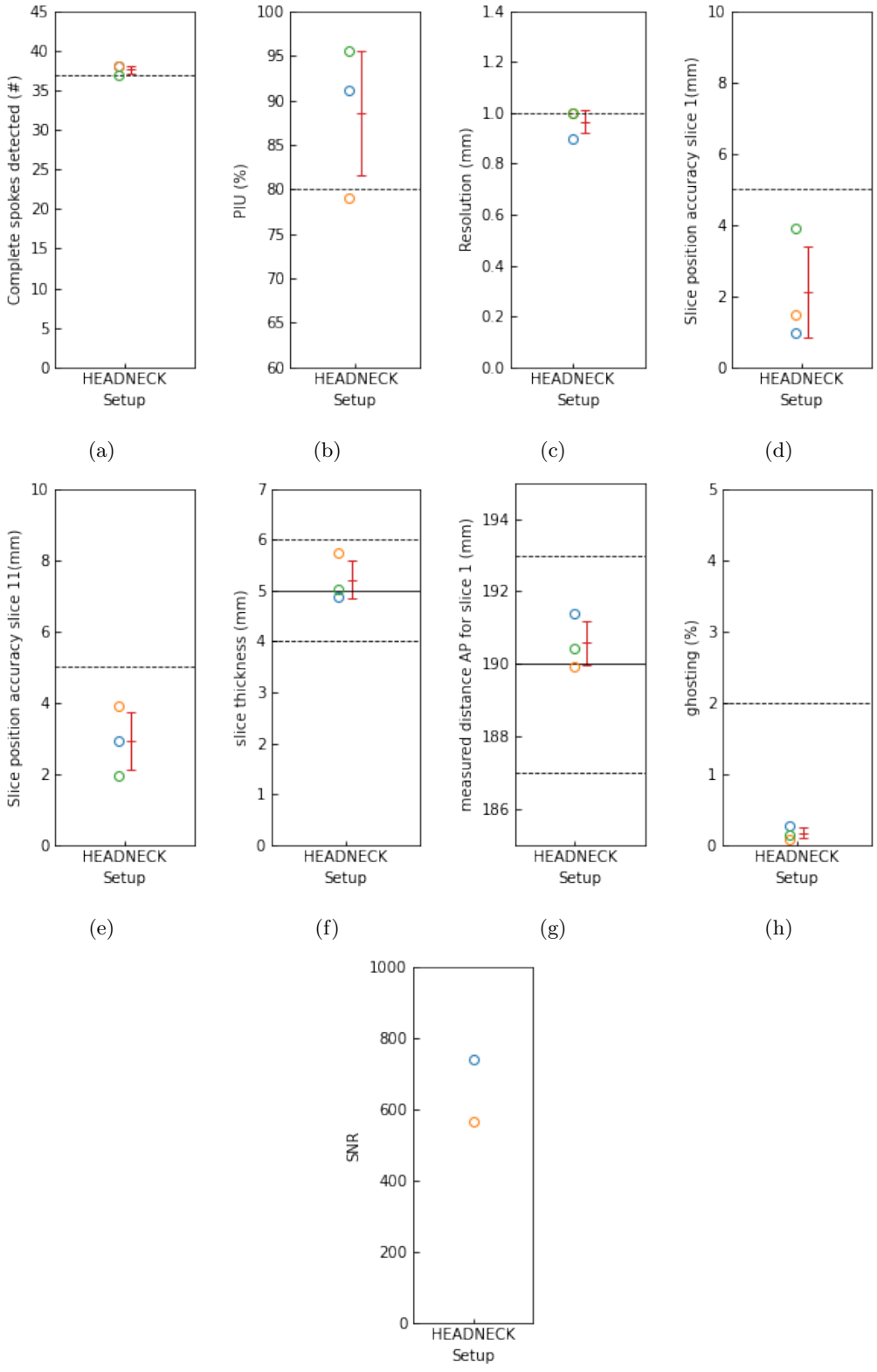

Figure 4.7: ACR measures for the T1-weighted series from Tromsø (blue marker), Trondheim (orange), Bergen (green). The score for (a) the low contrast detectability, (b) The image intensity uniformity, (c) high spatial resolution, slice position accuracy in absolute value for (d) slice one and (e) slice eleven, (f) slice thickness, (g) geometric accuracy for anterior to posterior in slice one, (h) ghosting and (i) SNR. The red marker indicates the mean score for the three centers and the standard deviation. The solid line represents the ideal ACR profile criterion and the dashed lines represents the interval the measure has to be within.

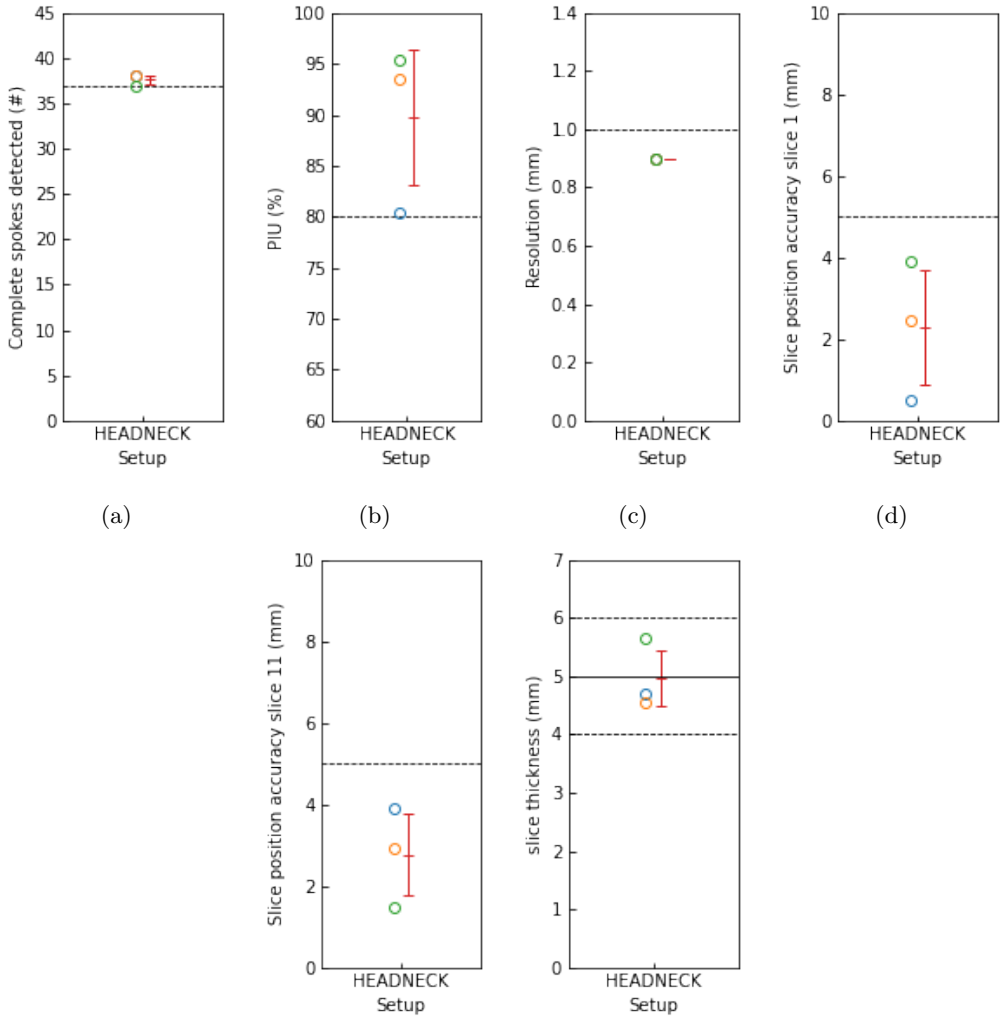

Figure 4.8: ACR measures for the T2 axial series from Tromsø (blue marker), Trondheim (orange), Bergen (green). The score for (a) the low contrast detectability, (b) The image intensity uniformity, (c) high spatial resolution, slice position accuracy for (d) slice one and (e) slice eleven and (f) slice thickness. The read marker indicates the mean score for the three centers and the standard deviation. The solid line represents the ideal ACR profile criterion and the dashed lines represents the interval the measure has to be within.The solid line represents the ideal ACR profile criterion and the dashed lines represents the interval the measure has to be within.

In Trondheim the three series were repeated three times with the same setup in the same position. The scans where done in March, April and May 2022. The variation for the different measures was small overall with some measures, specially PIU, showing a larger variation. Note that the slice position accuracy for slice eleven for May was within the criterion but higher than the recommended absolute value of 4 mm.

Table 4.7: Results for the QA of the T1-weighted series performed on the ACR phantom in March, April and May 2022 at the scanner in Trondheim.

Measure	Criterion	March	April	May
High contrast spatial resolution left to right (mm)	≤ 1.0	1.0	0.9	0.9
High contrast spatial resolution top to bottom (mm)	≤ 1.0	1.0	0.9	0.9
Slice thickness accuracy (mm)	5.0±1	5.72	4.97	5.40
Slice position accuracy slice 1 (mm)	≤ 5.0	1.45	1.95	0.97
Slice position accuracy slice 11 (mm)	≤ 5.0	-3.90	-2.93	-4.88
PIU (%)	≥ 80	**79.13**	92.09	91.20
Ghosting ratio (%)	≤ 3	0.09	0.18	0.28
Low contrast detectability	≥ 37	38	38	38
SNR	-	-	565	651
Geometric accuracy				
Sagittal length (mm)	148±3	146.97	146.48	146.48
Anterior to posterior in slice 1 (mm)	190±3	189.94	189.45	189.45
Left to right in slice 1 (mm)	190±3	190.92	192.38	192.38
Anterior to posterior in slice 5 (mm)	190±3	189.45	189.45	188.48
Left to right in slice 5 (mm)	190±3	189.94	190.43	190.43
Upper right to lower left in slice 5 (mm)	190±3	188.52	189.21	189.21
Lower right to upper left in slice 5 (mm)	190±3	189.21	190.59	189.21

Table 4.8: Results for the QA of the T2 axial series performed on the ACR phantom in March, April, and May 2022 at the scanner in Trondheim.

Measure	Criterion	March	April	May
High contrast spatial resolution left to right (mm)	≤ 1.0	0.9	0.9	0.9
High contrast spatial resolution top to bottom (mm)	≤ 1.0	0.9	0.9	0.9
Slice thickness accuracy (mm)	5.0 ±1	4.56	4.91	5.41
Slice position accuracy slice 1 (mm)	≤ 5.0	2.44	1.95	0.97
Slice position accuracy slice 11 (mm)	≤ 5.0	-2.93	-2.93	-3.91
PIU (%)	≥ 80	93.55	**76.87**	**79.01**
Low contrast detectability	≥ 37	38	38	38

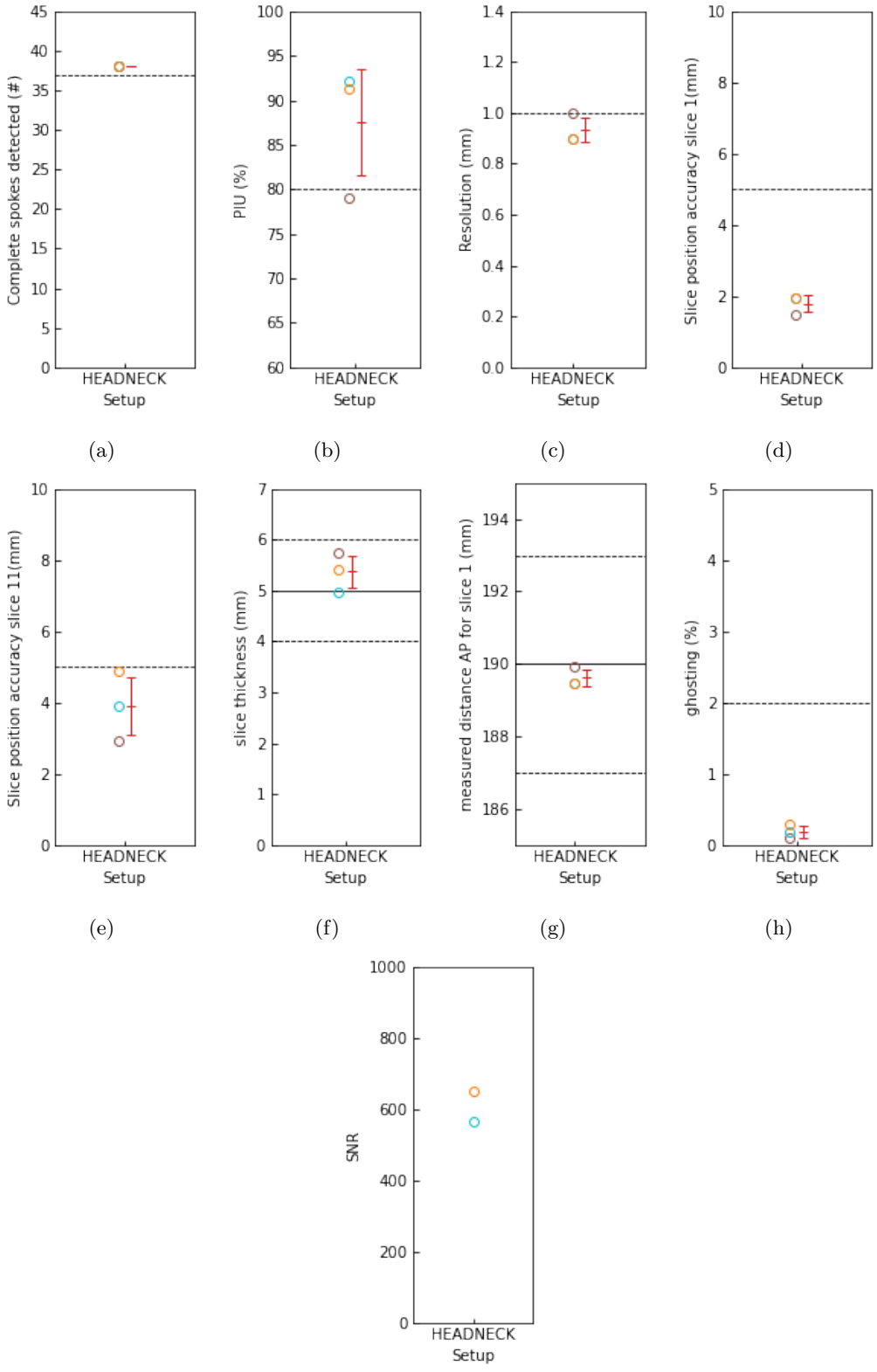

Figure 4.9: ACR measures for the T1-weighted series in Trondheim for March (brown marker), April (cyan), May (orange). The score for (a) the low contrast detectability, (b) The image intensity uniformity, (c) high spatial resolution, slice position accuracy for (d) slice one and (e) slice eleven, (f) slice thickness, (g) geometric accuracy for anterior to posterior in slice one, (h) ghosting and (i) SNR. The read marker indicates the mean score for the three centers and the standard deviation. The solid line represents the ideal ACR profile criterion and the dashed lines represents the interval the measure has to be within.

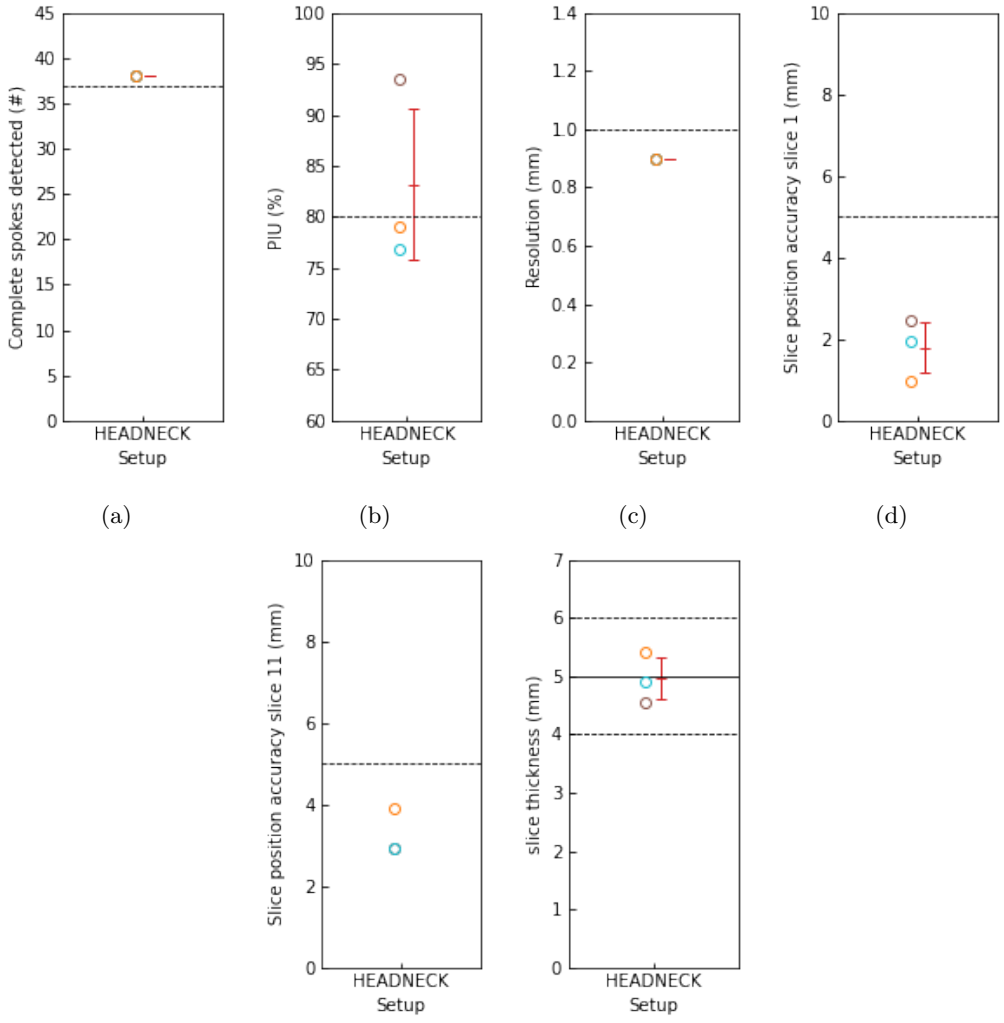

Figure 4.10: ACR measures for the T2 axial series from Trondheim for March (brown marker), April (cyan marker) and May (orange marker). The score for (a) the low contrast detectability, (b) The image intensity uniformity, (c) high spatial resolution, slice position accuracy in absolute value for (d) slice one and (e) slice eleven and (f) slice thickness. The read marker indicates the mean score for the three centers and the standard deviation. The solid line represents the ideal ACR profile criterion and the dashed lines represents the interval the measure has to be within.

In Tromsø a scan was performed where the phantom was scanned in 15 different positions in 4 centimeter intervals. The first position is 24 cm superior to the midpoint (0 cm) between the head and neck coil in the RT-setup. The phantom is then moved in intervals until a distance of 32 cm inferior, relative to the midpoint. The result for each of the RT-coil setups is presented in figure 4.11. The green circles represent data from the scans with both the head and the neck coil active and present. The orange x'es represent the scans with only the head coil active. Data points from -24 cm to -8 cm are common between the two setups since there was only acquired data with the head coil active while the neck coil was still present but inactive. From position 24 cm to 32 cm, there were only acquired images with complete head and neck setup and no acquisition with head only setup.

As the figure shows, every measure with both setups for every position is within the recommended

limits, with some clear exceptions. The low contrast detectability for the head only setup at position 8, 12, 16 and 20 cm had only a score of complete spokes detected below 37. The %PIU for the head only setup for position 20 cm is clearly lower than the recommended value with a value of 74%. The figure shows that most of the measures are pretty stable with varying position and coil setup, which indicates that the head only setup gives satisfactory results for the ACR phantom scans.

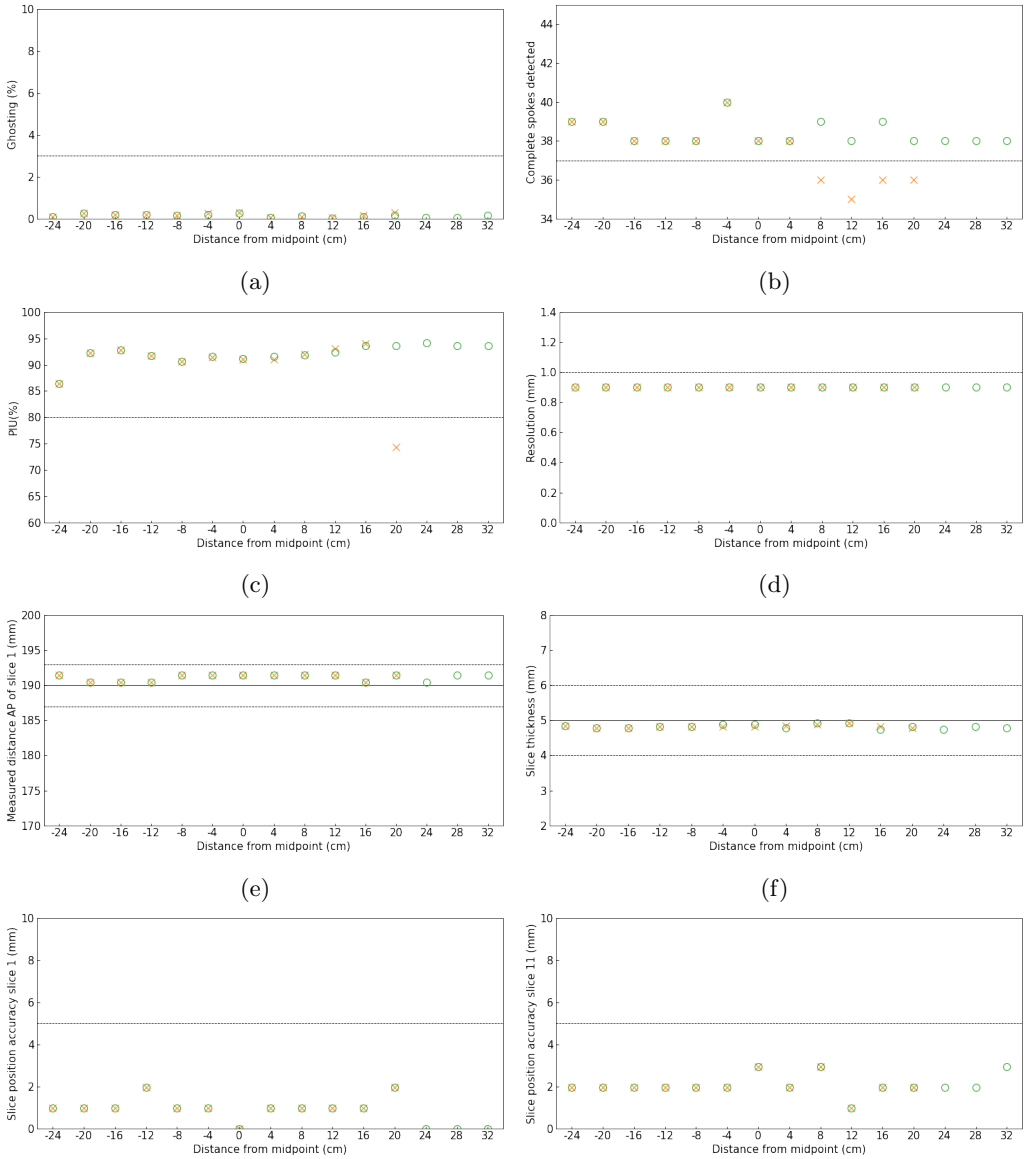

Figure 4.11: ACR measures for the T1-weighted series performed on the PET/MR-scanner in Tromsø. The green markers represents measurements with an RT-setup consisting of both a neck coil and a head coil, the orange marker represents measurements with no neck coil. "Negative" positions is positions superior relative to the midpoint of the head and neck setup. "Positive" positions are positions superior relative to the midpoint. The score for (a) the low contrast detectability, (b) The image intensity uniformity, (c) high spatial resolution, slice position accuracy in absolute value for (d) slice one and (e) slice eleven, (f) slice thickness, (g) geometric accuracy for anterior to posterior in slice one and (h) ghosting are presented. The solid line represents the ideal ACR profile criterion and the dashed lines represents the interval the measure has to be within.

The SNR-value for the different coil setups in all positions were calculated, and figure 4.12a shows the results. This scan was only acquired in Tromsø. The head and neck setup shows a higher SNR-value for all distances except -4 cm from the midpoint. For the 16 cm position, there is a small drop in the SNR value for the head and neck setup. To investigate whether this drop originates from the signal intensity or from the noise figure 4.12b and 4.12c present the signal value and the noise value, respectively. The noise in the 12, 16 and 20 cm positions for the head and neck setup shows an increased value compared to the other positions in the inferior direction from the midpoint. The figure shows a significantly higher SNR value for the complete head and neck RT-setup compared to head coil only for the positions 4, 8 and 12 cm. The enhancement is with a factor of 1.9, 1.9 and 1.7 for the three positions.

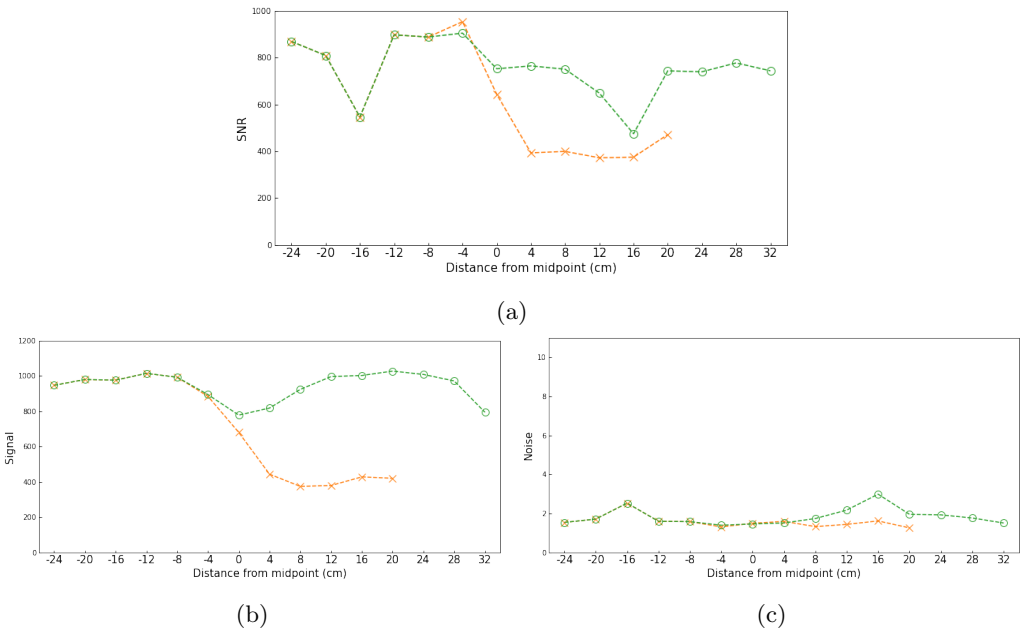

(a)

(b)

(c)

Figure 4.12: (a) SNR-values, (b) signal-values and (c) noise-values for the ACR-measurements in Tromsø. The green markers represents measurements with an RT-setup consisting of both a neck coil and a head coil, the orange marker represents measurements with no neck coil. "Negative" positions is positions superior, relative to the midpoint of the head and neck setup. "Positive" positions are positions inferior, relative to the midpoint.

Chapter 5

Discussion

The discussion is divided in two parts. First, a part discussing the QIBA phantom, then a part discussing the results from the ACR phantom. The results will be compared to results from similar studies.

5.1 The QIBA phantom

QA was performed in the three centers to investigate whether quantitative measurements from different centers can be directly compared or if there was a bias that should be taken into account. The RT-setup in the head and neck position was compared to the 16 channel diagnostic head coil to assess whether the results were satisfactory for clinical use. In the pelvic position, no diagnostic coil setup was compared to the RT-setup but we expected comparable results with the head and neck RT-setup. Two different sequences, a benchmark SS-EPI sequence, defined by QIBA, and the RESOLVE sequence, a sequence to be used in a clinical study, were compared to investigate and reveal possible differences.

In the comparison between the different coil setups it was expected that images acquired with the diagnostic 16-channel diagnostic head coil will have higher image quality. This was due to the increased distance between body and coils for the RT-setup, that was expected to result in a lower SNR compared to the 16-channel diagnostic coil. In addition, the body coil used in the RT-setup has 6 channels and was of lower quality than the 16-channel diagnostic head coil, also decreasing the signal intensity and SNR. The number of channels in a coil is directly related to the signal intensity acquired since each channel can receive signal. A coil with more channels will in total be able to receive more signal and therefore increase the SNR and the image quality.

The RESOLVE sequence has great clinical interest due to improved geometric precision and increased SNR in the images. By the use of parallel imaging, reacquisition and readout segmentation, the images acquired with the clinical RESOLVE sequence were expected to have higher quality than images acquired with the benchmark sequence. The clinical sequence uses much lower b-values than the benchmark sequence, the lower b-value will also make the images less diffusion weighted, and thus record higher signal intensity. The increased time consumption for the clinical sequence must be considered when it comes to heating, especially when imaging a phantom that has to be in thermal equilibrium. This was closely monitored by using localizer images that showed

the ice level inside the phantom.

For all centers, the QIBA recommendation for ADC bias in the center vial was fulfilled. The largest bias measured with all setups and sequences in the three centers was 1.9 % from the true ADC value, see figure 4.2 and 4.3. These small variations across all centers, setups and sequences showed that the ADC measurements were accurate. The variation of |ADC-bias| for the different vials was similar for the different sequences and setups. The ADC-bias reported in the result part is absolute bias, and the relative bias will increase with decreasing true ADC value in the vial since the absolute bias value did not vary with varying ADC value. The ADC-bias results for this study showed similar results as other studies have reported for the diffusion phantom with the same benchmark sequence [27].

All ADC measurements with one signal average with the head and neck and the pelvic RT-setups showed an error in the ADC value measurements above the QIBA recommendation. This was the case for both sequences and both RT-setups. An increase in error is closely related to a lower SNR value. The error in the ADC value was calculated using the standard deviation of the ROI which was also used to calculate the SNR, see equations (3.3) and (3.12). The results showed that the diagnostic setup had a lower error for the one signal average measurement compared to both RT-setups in the measurements acquired with the benchmark sequence. Two out of three centers had an error within the QIBA recommendation with the diagnostic setup, see figure 4.2 and 4.3. The difference in error between the benchmark sequence and the clinical sequence was evident for the one signal average measurement which can be expected because of the higher SNR with the clinical sequence. The error has been shown to be higher than the recommended values in other ADC studies, which is explained by a lower SNR in the body coils compared to the diagnostic head and neck coil [27] [28].

The error was affected when increasing the number of signal averages for the measurements. An increasing number of averages yielded a lower error for all setups and sequences, although the effect varies. The improvement in SNR when increasing the number of signal averages with a factor N is $\sqrt{N}$ and a part of the improvement in the error value can be explained by this [29]. The results showed that the best improvement in error could be seen from one to two signal averages, as could have been expected when the connection between the SNR and the number of signal averages was known. The improvement in error with an increase in the number of signal averages was most evident in the results from the benchmark sequence. For the higher number of signal averages, the results for the two sequences were more comparable to each other, with the pelvic RT-setup in Tromsø as an exception. The images in Tromsø were investigated to reveal any artifacts that could affect the standard deviation of the ROI or decrease the mean value. Nothing was found, but there would be a focus for further work to analyse new data for the pelvic RT-setup in Tromsø to reveal if there was just random fluctuations causing the difference. Improvement of error due to the number of signal averages was decisive for making the error results for the clinical sequence in Trondheim fulfill QIBA recommendation. The mean error of the four passes for 2 averages and 1123 averages fulfilled the QIBA recommendation for both the head and neck and the pelvic RT-setup. In summary, the error was relatively similar in the three centers and the head and neck RT-setup yields similar results to other studies. Increasing the number of signal averages proved to improve the error effectively. The trend was that Tromsø had the largest error for the benchmark sequence and Trondheim the lowest error for the clinical sequence.

The short-term repeatability for the ADC measurement for the center vial was within the QIBA

recommendation for all three setups with the benchmark sequence and with the two RT setups for the clinical sequence, see figure 4.2 and 4.3. The QIBA profile says that a possible reason for high wCV% can be due to a phantom out of thermal equilibrium. This study showed good short-term reproducibility, which is an indication of good preparations when it came to ice water refilling and monitoring of the ice level through localizers. Another reason for an enhanced wCV% may be distortions and/or artifacts inside the ROI in some of the passes. All passes were inspected and no such artifacts were revealed. The small variations between the wCV% for the scanners could then be due to random fluctuations or differences in the scanners, but since all wCV% values were within the recommendations, the RT-setups in both positions were suitable for intercenter comparison.

The wCV% increased for lower ADC values. This was expected as the wCV% is a relative measure where the mean ADC is the denominator, see equation (3.4). Therefore, a small change will have a large impact on the result for the lower ADC values. The results suggested that the wCV% was pretty stable for ADC values of 0.04 x 10^{-3} mm^2/s and higher. This seemed to be the case for both Trondheim and Tromsø while the results from Bergen showed a greater variation for the clinical sequence in particular. For Trondheim and Tromsø the results showed a smaller variation in the clinical sequence than in the benchmark sequence. An extra investigation of the Bergen images was done to reveal possible artifacts, but nothing out of the ordinary was found.

The reproducibility between centers was best for the diagnostic setup. The reproducibility for the RT setup was best for the clinical sequence and the head and neck setup had better results than the pelvic setup. These results can be expected based on the setups and sequences. The setup in the head and neck positions has a smaller distance between the phantom and the coils. Since there are no recommendations for reproducibility in the QIBA profile, it is necessary to compare the results with similar studies. Kooreman et al. performed the same QA for the, but with a 1.5 T scanner and achieved a reproducibilty of 0.6% for the ADC value measured in the center vial in a head and neck RT-coil setup with the benchmark protocol [27]. Houd et. al reported a reproducibility of 1.15 % for the intercenter reproducibility for the center vial in the QA of the QIBA phantom [28]. In the study by Houdt different sequences were used in different centers. The reproducibility results from these studies are of similar size as the reproducibility results in this project.

The SNR value for the b0 image should be greater than 50 according to the QIBA recommendations. This criterion was fulfilled for all three centers for the benchmark sequence for all setups. The results showed an expected reduction when changing from the diagnostic coil to the RT-setup. All centers showed a decrease when the RT-setup was used, but the change was smaller in Trondheim, where the RT-setup yielded the highest SNR of the three centers, but also the lowest SNR with the diagnostic coil, see figure 4.5.

The expected decrease in SNR value with increasing b-value was most prominent for the intervals b500 to b900 and from b900 to b2000 for the RT-setups. The decrease in SNR was due to the lower signal that was recorded when the images were more diffusion weighted. For the diagnostic coil, the SNR for the b500 image was higher than in the b0 image for the centers in Tromsø and Trondheim. The reason for this is not clear and the increase was only 4.6 % so the increase can also be explained by random fluctuations between the passes. The decrease was clear for the higher b-values, as we expected.

Comparing the SNR-values in the head and neck RT-setup by using both coils and only the head coil was done to investigate the importance of the neck coil in addition to the head coils. For the benchmark sequence, the inclusion of the neck coil made all b-value images except b2000 fulfill the recommendation, see figure 4.6. For the clinical sequence, all b-values had a satisfactory SNR value without the neck coil, but the inclusion of the neck coil showed a prominent improvement, demonstrating the importance of a complete head and neck setup if it is available. The results for these scans also showed that the RESOLVE sequence gave a better SNR value for all b-values. When considering these SNR results, it is important to consider which b-values that are relevant for clinical exams of humans. Several sources reports that b-values between 0 and 1000 are usually used [30]. Knowing that we can conclude that the low SNR-value of the b2000 image was not relevant for the performance of the RT-setup in a clinical setting.

The b-value dependence analysis resulted in that all pairs of b-values showed a b-value dependence of less than 2% for the RT-setups in all three centers. This was within the QIBA recommendations. The b-value dependence in the diagnostic setup was over the recommended value for the two combinations of b-value pairs in Trondheim and one combinations of b-value pairs in Tromsø. All combinations that did not fulfill the recommended values included the b2000 image. This is, as mentioned, a b-value that is not relevant for clinical examinations in most cases. The QIBA profile explains the increasing b-value dependence for higher b-values with the decreasing SNR-value, and this could explain the results for the higher b-values. The fact that the highest b-value dependence was seen in the diagnostic setup, which had the highest SNR, cannot be explained by this. It is important to consider how close the results were to being within the criterion. The Trondheim results that did not fulfill the recommendations were only 0.02% and 0.03% too high, and a new scan could have revealed if this is a trend or just random. Overall, the results for the b-value dependence were satisfactory, see figure 3.8.

5.2 The ACR phantom

The intercenter comparison for both the T1-weighted series and the T2-weighted series showed similar results in all three centers for the majority of measures. All but one measure were within the recommendations set by the ACR phantom profile for all centers, this was the %PIU in the T1 weighted series in Trondheim. The variation between centers varies between measures, but overall this study showed that the centers yielded comparable results for the measures recommended for the ACR phantom. The images acquired in this study have all been acquired with a matrix size of 256x256 and a pixel size of 0.977 mm, but the images from Bergen and from the scan in March in Trondheim were reconstructed to a 512x512 matrix in the scanner software, resulting in a pixel size of 0.489 mm for these two data sets. Note that for the intercenter comparison, the Trondheim data from the scan in March was used for all measures except SNR. The only measure that the pixel size seems to really affect was the high contrast spatial resolution in the T1-weighted series, which will be commented on later in this section.

The only measure that did not fulfill the recommended value was the %PIU for the scan in Trondheim. The value was close to be within the recommendation so the images used for calculation was inspected to reveal any possible artifacts, but no artifacts were revealed. Note that the %PIU measure from Trondheim was 79.13% and almost fulfilled the recommendation, so the clinical consequences should not be exaggerated. The later scans, performed in April and May showed an increase in the %PIU, and the March result for %PIU could be as it was due to a random error. The possibility that the pixel size should influence this measure was not considered since it was calculated as the mean value of a circular ROI, and that the mean was not influenced to that degree by including more pixels. This assumption was also supported by the high %PIU in Bergen.

In all measures where distance was calculated, such as geometric distortion, slice position accuracy and slice thickness, the pixel size of the images would define how exact the distances could be measured. With infinitesimal small pixels, the distance from one bright edge to the adjacent bright edge could have been measured with maximal precision. In the analysis, it was not possible to tell where a bright edge was inside a given pixel, we just knew in which pixel it was. Therefore, the distance measures were quantified and exact distances were not possible to measure. Note that the problem was not as prominent for the slice thickness accuracy as for other measures. As an example, an underestimation in measured distance of 1 mm for both ramps would give a difference of 0.1 mm in the final slice thickness accuracy result according to the ACR-phantom manual.
Results that were close to the recommended values should be looked at with the pixel size in mind and scanners close to the value should be followed with extra focus in upcoming QAs to see if the results deviate more and more towards too high or low values.

The high contrast spatial resolution test resulted in a resolution of 0.9 mm in Tromsø for the T1-weighted series and for the T2-weighted series in all three centers. This means that the resolution score from the test was lower than the pixel size in the image. This should be noted as a weakness for the test. The reconstructed data from Trondheim and Bergen showed a poorer resolution compared to Tromsø. In the images from Trondheim and Bergen there was an apparent "smear out" effect caused by the reconstruction. A zero padding technique would make the image look more smooth and less "pixely", this can be an explanation for the lower score in the test [31]. This effect was not present in the scans performed in April and May from Trondheim, where the images were 256x256 matrices.

One way to increase the SNR, as stated in the discussion of the results in the study by Kooreman et al., is to increase the voxel size [27]. Therefore, it was desired to have the same voxel size in the intercenter comparison. In March, no SNR data was acquired so the SNR data used in the intercenter comparison was from April, where the pixel size was the same as in Tromsø. The SNR value in Tromsø was clearly higher than in Trondheim. In the ACR phantom profile, poor slice thickness accuracy and PIU are mentioned as measures that are related to poor SNR. Looking at the results, it was not possible to see a pattern relating the measures, as both the %PIU and the slice thickness accuracy had good results for the April scan in Trondheim. The low-contrast detectability is said to be affected by ghosting artifacts and poor SNR values. The results showed that all centers fulfill the recommended score of 37 or more complete spokes detected. This fit well with the low score for ghosting artifacts and showed that the lower SNR in Trondheim was still good enough to ensure the desired detectability.

The monthly repetition of the scan in Trondheim was done to investigate to what extent the results were reproducible. The results showed stable results for a majority of the measures and the study showed that the scanner performed stable. The %PIU measure in both the T1-weighted and T2-weighted series has a result from March that differs clearly from the two other months. Ideally, the data for March included the SNR scan so that this difference could have been investigated, to see ifv the SNR and %PIU had a relation. For the T2-weighted %PIU, both the April and May scans have a result lower than the recommended value. Investigation of the images used for calculation revealed no artifacts or distortions in the images and the low uniformity did not seem to be critical for the image quality. Note that the %PIU-values were close to fulfill the recommendations and that the images still fulfill the recommendation for every other measure.

The result for slice position accuracy for slice 11 in May for the T1-weighted series was clearly higher than the value for the two previous months. It is advisable to have a score of 4 mm or less, but the scanner passes the test with a score of 5 or less. For this scanner, an idea could be to monitor development to see if the May measurement was an abnormality or if adjustments should be made. For this exact result, the effect of a relatively large voxel size compared to the distance measured has to be considered. The other months have lower results, suggesting that the actual slice position accuracy for May was also lower. In total the results from the monthly repeated scans showed that the measures have comparable values for most measures. To reveal whether the small abnormalities were random or if there were trends that were not revealed with only three repetitions, the scan can be performed more times and over a longer period to collect more data that can be compared.

In Tromsø, a scan was performed to investigate the effect of RT-setup and the position had on the measures. By moving the phantom a distance away from the center of the head and neck RT-setup and comparing a head coil only setup with a head and neck setup any differences in performance would be revealed. The results showed similar performance for both setups in the different positions for all measures recommended for the T1-weighted series. The measures were also very stable when comparing the different positions, showing that the image quality outside the center of the RT-setup was on a satisfactory level. Of all the measures, only one measure was not within the recommended values. The number of complete spokes detected for the 8, 12, 16 and 20 cm position without neck coil was not fulfilling the recommendation. These positions without neck coil also had the lowest SNR, which was previously mentioned as a reason for poorer low contrast detectability. It should be noted that the SNR values for these positions were just below 400. The result indicates that the SNR had to be significantly low before the image quality was affected.

The result gives a measure on how large the difference in SNR-value between the centers in Tromsø and Trondheim had to be before we would see the same effect in compared image quality.

The need for the inclusion of the neck coil was not justified with the ACR profile-recommended measures. The effect was evident for the inferior positions for the SNR results. When a potential patient is positioned in the head and neck RT-setup for imaging of neck cancer, the patient's chin is positioned in the center of the setup, i.e. at position 0 cm. The neck will naturally be in a position between approximately 4 and 8 cm inferior relative to the midpoint. This was the positions where we started to see clear evidence that the SNR values were much better for a complete head and neck setup. As an example, the SNR value at 4 cm improved with a factor of 1.9 when including the neck coil. Figure 4.12b shows that the increase in SNR was due to the increase in signal rather than the decrease in noise. This indicates that the increased acquired signal was what we gained by including the neck coil. This effect should be further investigated to see if there are visual differences in clinical scans. The measures used in the ACR phantom manual were not affected by the large SNR improvement that we can see that the neck coil provides.

The overall results of the ACR QA were similar to those achieved in other studies when performing QA with the Large ACR phantom. A study by Ihalainen et al. from 2011 showed similar results for the measures for a 3 T scanner. The study showed that the ACR method was feasible for QA of a multi-scanner center, similar to what the results in this thesis showed. The results for each measure were similar as well.
In another study, Etman et al. performed quality assurance with the ACR phantom on a 1.5 T scanner. The study by Etman et al. also showed similar results for all measures as achieved in this thesis [32]. Note that the recommended value for %PIU and LCD is different for 1.5 T than for 3.0 T.

Similarities with other studies, in addition to the fact that a large majority of the measures were within the recommended values, indicate that the ACR method is feasible for intercenter studies. The results presented in this thesis showed that the variation between the centers was relatively small and that it is realistic to compare the quantitative MRI values acquired with the RT-tailored setup between centers in a clinical study. The further work should focus on collecting more data by performing the QA more times in each center to increase the certainty of the results. The inclusion of ACR QA in the pelvic RT-setup would also be natural to focus on in future work.

Chapter 6

Conclusion

The DWI results showed that the RT-tailored setups both in the head and neck position as well as in the pelvic position yield results that are within recommended values for all measures except the error in ADC-measurements, which is too high. The results did not show any clear institutional bias in the measured ADC values, which indicates that the results from different centers can be used in the same study. The high error results have to be addressed, but the results showed that an increase in DWI signal averages improved the results, which can be further investigated to find the perfect compromise between error and time consumption. The results of the QA with the ACR phantom showed that the recommended measures in the ACR phantom profile have values within the criterion for the majority of the measures for the head and neck RT-setup. The few measures that did not fulfill the recommendation were very close, and the results showed that failure in one of the tests did not necessarily cause the series to fail other tests or make the images unusable. The effect of the inclusion of the neck coil in the head and neck coil RT-setup was evident for the SNR value and the detectability of low contrast objects in a position relevant for neck cancer. Further image acquisitions with the phantom in these positions can be done to include the ideal combination of head, neck and spine coils.

For future work, a larger dataset should be acquired and assessed to easier reveal if results deviating from the ideal value are random or if there is a trend. This is the case for both QA processes. The next step is to acquire images of humans in a clinical setting and analyze the images to see if the RT-setup with the clinical sequence can yield images of similar quality as the diagnostic coil. Overall, the results showed that the RT-tailored setup performed stable within the recommendation for the majority of measures in both QA processes and that the use of the quantitative measures in a clinical study is realistic.

Bibliography

[1] *Radiation Therapy for Cancer - NCI*. Archive Location: nciglobal,ncienterprise. 29th Apr. 2015. URL: https://www.cancer.gov/about-cancer/treatment/types/radiation-therapy (visited on 10/06/2022).

[2] Wolfgang Schlegel, Thomas Bortfeld and A. Grosu, eds. *New technologies in radiation oncology*. Berlin ; London: Springer, 2006. 464 pp. ISBN: 978-3-540-00321-2.

[3] Jisang Park et al. 'Diagnostic Accuracy and Confidence of [18F] FDG PET/MRI in comparison with PET or MRI alone in Head and Neck Cancer'. In: *Scientific Reports* 10.1 (11th June 2020). Number: 1 Publisher: Nature Publishing Group, p. 9490. ISSN: 2045-2322. DOI: 10.1038/s41598-020-66506-8. URL: https://www.nature.com/articles/s41598-020-66506-8 (visited on 04/06/2022).

[4] Raymond F. Muzic and Frank P. DiFilippo. 'PET/MRI – Technical Review'. In: *Seminars in roentgenology* 49.3 (July 2014), pp. 242–254. ISSN: 0037-198X. DOI: 10.1053/j.ro.2014.10.001. URL: https://www.ncbi.nlm.nih.gov/pmc/articles/PMC4451572/ (visited on 08/05/2022).

[5] Luís Curvo-Semedo et al. 'Diffusion-weighted MRI in rectal cancer: Apparent diffusion coefficient as a potential noninvasive marker of tumor aggressiveness'. In: *Journal of Magnetic Resonance Imaging* 35.6 (2012). _eprint: https://onlinelibrary.wiley.com/doi/pdf/10.1002/jmri.23589, pp. 1365–1371. ISSN: 1522-2586. DOI: 10.1002/jmri.23589. URL: https://onlinelibrary.wiley.com/doi/abs/10.1002/jmri.23589 (visited on 07/06/2022).

[6] Amita Shukla-Dave et al. 'Quantitative imaging biomarkers alliance (QIBA) recommendations for improved precision of DWI and DCE-MRI derived biomarkers in multicenter oncology trials'. In: *Journal of Magnetic Resonance Imaging* 49.7 (2019). _eprint: https://onlinelibrary.wiley.com/doi/p e101–e121. ISSN: 1522-2586. DOI: 10.1002/jmri.26518. URL: https://onlinelibrary.wiley.com/doi/abs/10.1002/jmri.26518 (visited on 25/04/2022).

[7] *Profiles - QIBA Wiki*. URL: https://qibawiki.rsna.org/index.php/Profiles (visited on 01/06/2022).

[8] *ACR MRI Accreditation*. URL: https://www.acraccreditation.org/modalities/mri (visited on 08/06/2022).

[9] *Spin*. Questions and Answers in MRI. URL: http://mriquestions.com/what-is-spin.html (visited on 11/11/2021).

[10] Robert A. Pooley. 'Fundamental Physics of MR Imaging'. In: *RadioGraphics* 25.4 (July 2005), pp. 1087–1099. ISSN: 0271-5333, 1527-1323. DOI: 10.1148/rg.254055027. URL: http://pubs.rsna.org/doi/10.1148/rg.254055027 (visited on 11/11/2021).

[11] *Bloch equations*. Questions and Answers in MRI. URL: http://mriquestions.com/bloch-equations.html (visited on 11/11/2021).

[12] *magnetic scanner 3d model*. URL: https://www.turbosquid.com/3d-models/magnetic-scanner-3d-model/885621 (visited on 10/12/2021).

[13] *Cause of magnetism*. Questions and Answers in MRI. URL: http://mriquestions.com/what-causes-magnetism.html (visited on 07/06/2022).

[14] 'Spaced Out: Spatial Encoding'. In: *MRI from Picture to Proton*. Ed. by Donald W. McRobbie et al. 3rd ed. Cambridge: Cambridge University Press, 2017, pp. 102–123. ISBN: 978-1-107-70695-8. DOI: 10.1017/9781107706958.009. URL: https://www.cambridge.org/core/books/mri-from-picture-to-proton/spaced-out-spatial-encoding/2F557F6B624787162C3D16FC0E28A571 (visited on 11/11/2021).

[15] *T1, T2 and PD weighted imaging - Radiology Cafe*. 28th Mar. 2017. URL: https://www.radiologycafe.com/frcr-physics-notes/mr-imaging/t1-t2-and-pd-weighted-imaging/ (visited on 07/06/2022).

[16] *MRI sequences - Echo planar (EPI)*. IMAIOS. URL: https://www.imaios.com/en/e-Courses/e-MRI/MRI-Sequences/echo-planar-imaging (visited on 08/05/2022).

[17] *k-space and MR signal*. Questions and Answers in MRI. URL: http://mriquestions.com/why-signal-harr-k-space.html (visited on 07/06/2022).

[18] *Diffusion*. Questions and Answers in MRI. URL: http://mriquestions.com/what-is-diffusion.html (visited on 01/06/2022).

[19] Usman Bashir. *Diffusion-weighted imaging — Radiology Reference Article — Radiopaedia.org*. Radiopaedia. DOI: 10.53347/rID-16718. URL: https://radiopaedia.org/articles/diffusion-weighted-imaging-2 (visited on 01/06/2022).

[20] *Apparent Diffusion*. Questions and Answers in MRI. URL: http://mriquestions.com/apparent-diffusion.html (visited on 01/06/2022).

[21] *Echo Planar Imaging - an overview — ScienceDirect Topics*. URL: https://www.sciencedirect.com/topics/medicine-and-dentistry/echo-planar-imaging (visited on 09/05/2022).

[22] Julien Cohen-Adad. 'High-Resolution DWI in Brain and Spinal Cord with syngo RESOLVE'. In: *Clinical Neurology* (), p. 8.

[23] David A. Porter and Robin M. Heidemann. 'High resolution diffusion-weighted imaging using readout-segmented echo-planar imaging, parallel imaging and a two-dimensional navigator-based reacquisition: EPI With Parallel Imaging and 2D Reacquisition'. In: *Magnetic Resonance in Medicine* 62.2 (Aug. 2009), pp. 468–475. ISSN: 07403194. DOI: 10.1002/mrm.22024. URL: https://onlinelibrary.wiley.com/doi/10.1002/mrm.22024 (visited on 02/05/2022).

[24] A. K. Shukla and Utham Kumar. 'Positron emission tomography: An overview'. In: *Journal of Medical Physics / Association of Medical Physicists of India* 31.1 (2006), pp. 13–21. ISSN: 0971-6203. DOI: 10.4103/0971-6203.25665. URL: https://www.ncbi.nlm.nih.gov/pmc/articles/PMC3003889/ (visited on 08/05/2022).

[25] 'Hybrid FDG PET/MRI vs. FDG PET and CT in patients with suspected dementia – A comparison of diagnostic yield and propagated influence on clinical diagnosis and patient management'. In: *PLOS ONE* 14.5 (2nd May 2019). Publisher: Public Library of Science, e0216409. ISSN: 1932-6203. DOI: 10.1371/journal.pone.0216409. URL: https://journals.plos.org/plosone/article?id=10.1371/journal.pone.0216409 (visited on 04/06/2022).

[26] *RESOLVE*. URL: https://www.siemens-healthineers.com/magnetic-resonance-imaging/options-and-upgrades/clinical-applications/syngo-resolve (visited on 02/06/2022).

[27] Ernst S. Kooreman et al. 'Feasibility and accuracy of quantitative imaging on a 1.5 T MR-linear accelerator'. In: *Radiotherapy and Oncology* 133 (1st Apr. 2019), pp. 156–162. ISSN: 0167-8140. DOI: 10.1016/j.radonc.2019.01.011. URL: https://www.sciencedirect.com/science/article/pii/S0167814019300167 (visited on 05/06/2022).

[28] Petra J. van Houdt et al. 'Phantom-based quality assurance for multicenter quantitative MRI in locally advanced cervical cancer'. In: *Radiotherapy and Oncology*. Physics Special Issue: ESTRO Physics Research Workshops on Science in Development 153 (1st Dec. 2020), pp. 114–121. ISSN: 0167-8140. DOI: 10.1016/j.radonc.2020.09.013. URL: https://www.sciencedirect.com/science/article/pii/S0167814020307854 (visited on 07/06/2022).

[29] Waseem Zafar et al. 'Resolution, SNR, signal averaging and scan time in mri formetastatic lesion in spine. A case report'. In: (), p. 4.

[30] *b-value diffusion*. Questions and Answers in MRI. URL: http://mriquestions.com/what-is-the-b-value.html (visited on 08/06/2022).

[31] *Zero filling (ZIP)*. Questions and Answers in MRI. URL: http://mriquestions.com/zip.html (visited on 08/06/2022).

[32] H. M. Etman et al. 'The effect of quality control on the function of magnetic resonance imaging (MRI), using American College of Radiology (ACR) phantom'. In: *The Egyptian Journal of Radiology and Nuclear Medicine* 48.1 (1st Mar. 2017), pp. 153–160. ISSN: 0378-603X. DOI: 10.1016/j.ejrnm.2016.12.003. URL: https://www.sciencedirect.com/science/article/pii/S0378603X16302327 (visited on 08/06/2022).

Appendix

Python code used for diffusion QA

In this appendix the code used for image analysis in the DWI QA is presented. **help_functions.py** is a collections of functions that is resued in the other python scripts, see A. **ADC_qualities_near_isocenter.py** calculates the ADC-bias, error and short-term repeatability in center vial, presented in B. **reproducibility.py** calculates the intercenter reproducibility, the code is presented in C. The code calculating the b-value dependence for the ADC measurement is presented in **ADC_b-value_dependence.py** in D. SNR.py calculates the the SNR value for the ADC-map and all b-value images and is presented in E.

A help_functions.py

```
import numpy as np
import nibabel as nib

##############################################################################
#  Help functions that is used throughout the analysis in the other files.
#
##############################################################################


def weighted_sample_std(array, weights):
    """ Calculates the weighted sample std of an array, which yields similar results
    w_mean = np.average(array, weights=weights)
    N_nonzero = np.sum(np.where(weights != 0, 1, 0))

    return np.sqrt(np.sum(weights*(array-w_mean)**2) /
                   (N_nonzero-1) * np.sum(weights) / N_nonzero)


def get_vial_mask(segm_data, vial_nr):
    """ Returns data-file in the shape of segm_data which is a
        binary mask for vial nr (1 for values=vial_nr, else 0) """
    return np.where(segm_data == vial_nr, 1, 0)


def vial_avg_std(ADC_map, segment, vial_nr):
    """ Calculates the average and sample std of a vial based on
        an ADC map and a segmentation map. """
    vial_mask = get_vial_mask(segment, vial_nr)
    avg = np.average(ADC_map, weights=vial_mask)
    std = weighted_sample_std(ADC_map, vial_mask)
    return avg, std
```

```
def unpack_nifty(filename):
    """ Oens nifty and returns the image as a numpy array """
    image = nib.load(filename)
    # rotate image 90 degrees for consistency with 3D slicer

    return np.rot90(image.get_fdata())
```

B ADC_qualities_near_isocenter.py

```
from help_functions import *
import numpy as np

#########################################################################################
#  Calculates bias, error (precision) and short-term repeatability and stores the res
#
#########################################################################################

# Input values
image = 'EP2D_16CHHN_HEAD_TRA'
appx = '_BERGEN'    # "" for Tromso, "_TRONDH", "_BERGEN" for Trondheim
avs = [1, 2]

# Load segmentation map
segmentation = unpack_nifty(
    fr'D:\Ole\Masteroppgave\Marens_arbeid\Prosjektoppgave\Labelmaps\
    ____{image}{appx}_ADC_vial1_d15mm-label.nii.gz'
)
test=np.where(segmentation==1)
# Store results in a .txt file
filename = image + appx + "_ADC_qualities_near_isocenter.txt"
file = open(f"./results/{filename}", "w")

# ---------------------- #
#  Calculate results  #
# ---------------------- #

# Reference value
ADC_ref = 1127  # unit: [10^6 mm^2/s]

# Number of pixels in ROI
N = np.sum(segmentation)

for av in avs:
    print(f"{image.replace('_',' ')} {av}AV{appx.replace('_',' ')}")
```

```
file.write(f"{image.replace('_',␣'␣')}␣{av}AV{appx.replace('_',␣'␣')}"
           f"\n")

# Create array for storing averages per pass for short-term repeatability
avgs = np.empty(4)

for pass_nr in range(1, 5):
    print("Pass", pass_nr)
    file.write(f"Pass␣{pass_nr}\n")

    # Retrieve ADC map and calculate ROI mean and std
    ADC_map = unpack_nifty(
        f'./data/{image}{av}AV_PASS{pass_nr}_ADC{appx}.nii.gz'
    )
    avg = np.average(ADC_map, weights=segmentation)
    print(avg)
    std = weighted_sample_std(ADC_map, segmentation)

    # Calculate measures and write results to file
    bias = avg - ADC_ref
    ci = 1.96 * std / np.sqrt(N)
    bias_prc = 100 * (avg - ADC_ref) / ADC_ref
    error = 100 * std / avg

    print(f"ADC␣bias:␣({round(bias,␣3)}␣+-␣{round(ci,␣3)})␣x␣10^-6␣mm^2/s")
    file.write(f"ADC␣bias:␣({round(bias,␣3)}␣+-␣{round(ci,␣3)})␣x␣10^-6␣mm^2/s"
               f"\n")
    print(f"ADC␣%bias:␣{round(bias_prc,␣2)}%")
    file.write(f"ADC␣%bias:␣{round(bias_prc,␣2)}%\n")
    print(f"ADC␣error:␣{round(error,␣2)}%")
    file.write(f"ADC␣error:␣{round(error,␣2)}%\n")
    print()
    file.write("\n")

    # Store ROI mean in array
    avgs[pass_nr - 1] = avg

print("Short-term␣repeatability:")
file.write("Short-term␣repeatability:\n")

# Calculate short-term repeatability and write to file
std_w = np.std(avgs)
mean = np.mean(avgs)
RC = 2.77 * std_w
wCV = 100 * std_w / mean
```

```
    print(f"RC: {round(RC, 3)} x 10^-6 mm^2/s")
    file.write(f"RC: {round(RC, 3)} x 10^-6 mm^2/s\n")
    print(f"wCV: {round(wCV, 2)}%")
    file.write(f"wCV: {round(wCV, 2)}%\n")
    print("-------------------------------------------------------")
    file.write("\n-------------------------------------------------------\n")
    print()
    file.write("\n")

file.close()
```

C ADC_reproducibility.py

```
from help_functions import *

#################################################
#  Calculates reproducibility between centers  #
#################################################

# Input parameters
image = 'EP2D_16CHHN_HEAD_TRA'
avs = [1, 2]

# Load segmentation maps
segmentation_tromso = unpack_nifty(
        fr'D:\Ole\Masteroppgave\Marens_arbeid\Prosjektoppgave\
        Labelmaps\{image}_ADC_vial1_d15mm-label.nii.gz')
print()
segmentation_trondh = unpack_nifty(
        fr'D:\Ole\Masteroppgave\Marens_arbeid\Prosjektoppgave\
        Labelmaps\{image}_TRONDH_ADC_vial1_d15mm-label.nii.gz')

segmentation_bergen = unpack_nifty(
        fr'D:\Ole\Masteroppgave\Marens_arbeid\Prosjektoppgave\
        Labelmaps\{image}_BERGEN_ADC_vial1_d15mm-label.nii.gz')



# ------------------------------------------ #
#  Calculate intercenter reproducibility  #
# ------------------------------------------ #

# Open file for storing results
filename = f"{image}_reproducibility.txt"
file = open(f"./results/{filename}", "w")
print(f"Reproducibility - {image.replace('_', ' ')}")
file.write(f"Reproducibility - {image.replace('_', ' ')}\n\n")
```

```
# loop through averages
for av in avs:
    # Load relevant data
    ADC_tromso = unpack_nifty(f'./data/{image}{av}AV_PASS1_ADC.nii.gz')
    ADC_trondh = unpack_nifty(f'./data/{image}{av}AV_PASS1_ADC_TRONDH.nii.gz')
    ADC_bergen = unpack_nifty(f'./data/{image}{av}AV_PASS1_ADC_BERGEN.nii.gz')

    # Calculate the mean ADC value in the ROI for both locations
    mean_tromso = np.average(ADC_tromso, weights=segmentation_tromso)
    mean_trondh = np.average(ADC_trondh, weights=segmentation_trondh)
    mean_bergen = np.average(ADC_bergen, weights=segmentation_bergen)
    # Calculate the %CV- and %RDC-values
    means = np.array([mean_tromso, mean_trondh, mean_bergen])

    CV = np.std(means) / np.mean(means) * 100
    RDC = 2.77 * np.std(means) / np.mean(means) * 100

    # Display and save results
    print(f"{av}AV")
    print(f"%CV = {round(CV, 3)}%")
    print(f"%RDC = {round(RDC, 3)}%\n")

    file.write(f"{av}AV\n")
    file.write(f"%CV = {round(CV, 3)}%\n")
    file.write(f"%RDC = {round(RDC, 3)}%\n\n")

file.close()
```

D ADC_b-value_dependence.py

```
from help_functions import *
import numpy as np

# Input values
image = 'EP2D_RTHN_HEADNECK_TRA'
appx = '_BERGEN'   # "" for Tromso, "_TRONDH", "_BERGEN" for Trondheim
bs = [0, 500, 900, 2000]
save = True

# Load segmentation map for center vial
segmentation_center = unpack_nifty(
    fr'D:\Ole\Masteroppgave\Marens_arbeid\Prosjektoppgave\Labelmaps\{image}{appx}_ADC
)


# ---------- #
#  Load ADC-maps  #
```

```
# ------------------ #
pass_nr = 1

ADC_b1 = np.load(
    f"./data/{image}1AV_PASS{pass_nr}_ADCb({bs[0]},{bs[1]}){appx}.npy"
)
ADC_b2 = np.load(
    f"./data/{image}1AV_PASS{pass_nr}_ADCb({bs[0]},{bs[2]}){appx}.npy"
)
ADC_b3 = np.load(
    f"./data/{image}1AV_PASS{pass_nr}_ADCb({bs[0]},{bs[3]}){appx}.npy"
)


# ------------------------------------------------------------------ #
#  Calculate b-value dependence as described in QIBA profile  #
# ------------------------------------------------------------------ #

if save:
    # calculate mean ADC in center vial
    ADC_b1 = np.average(ADC_b1, weights=segmentation_center)
    ADC_b2 = np.average(ADC_b2, weights=segmentation_center)
    ADC_b3 = np.average(ADC_b3, weights=segmentation_center)

    # Open file for storing data
    filename = f"{image}{appx}_b-value_dependence.txt"
    file = open(f"./results/{filename}", 'w')
    file.write(f"{image.replace('_',' ')}{appx.replace('_',' ')} "
               f"- ADC b-value dependence\n\n")
    print(f"{image.replace('_',' ')}{appx.replace('_',' ')} "
          f"- ADC b-value dependence\n")

    # b1 vs b2
    file.write(f"ADC(b=({bs[0]}, {bs[1]})) vs ADC(b=({bs[0]}, {bs[2]}))\n")
    file.write(f"ADC b-value dependence: "
               f"{round(100 * np.abs((ADC_b2 - ADC_b1) / ADC_b1), 2)}%\n\n")
    print(f"ADC(b=({bs[0]}, {bs[1]})) vs ADC(b=({bs[0]}, {bs[2]}))")
    print(f"ADC b-value dependence: "
          f"{round(100 * np.abs((ADC_b2 - ADC_b1) / ADC_b1), 2)}%\n")

    # b2 vs b3
    file.write(f"ADC(b=({bs[0]}, {bs[2]})) vs ADC(b=({bs[0]}, {bs[3]}))\n")
    file.write(f"ADC b-value dependence: "
               f"{round(100 * np.abs((ADC_b3 - ADC_b2) / ADC_b2), 2)}%\n\n")
    print(f"ADC(b=({bs[0]}, {bs[2]})) vs ADC(b=({bs[0]}, {bs[3]}))")
    print(f"ADC b-value dependence: "
```

```
            f"{round(100 * np.linalg.norm((ADC_b3 - ADC_b2) / ADC_b2), 2)}%\n")

    # b1 vs b3
    file.write(f"ADC(b=({bs[0]}, {bs[1]})) vs ADC(b=({bs[0]}, {bs[3]}))\n")
    file.write(f"ADC_b-value dependence: "
               f"{round(100 * np.abs((ADC_b3 - ADC_b1) / ADC_b1), 2)}%\n\n")
    print(f"ADC(b=({bs[0]}, {bs[1]})) vs ADC(b=({bs[0]}, {bs[3]}))\n")
    print(f"ADC_b-value dependence: "
          f"{round(100 * np.abs((ADC_b3 - ADC_b1) / ADC_b1), 2)}%\n\n")

    file.close()
```

E SNR.py

```
from help_functions import *

#########################################################
#  Calculates SNR for b-value images and ADC-maps  #
#########################################################

# Input values
image = 'EP2D_RTPELV_PELVIS_TRA'
appx = ''   # "" for Tromso, "_TRONDH" , "_BERGEN"for Trondheim
avs = [1, 2, 3, 2235]
bs = [0, 500, 900, 2000]
bvalue_only = False   # Only calculate SNR for b-value images

# Load segmentation map
segmentation = unpack_nifty(
    fr'D:\Ole\Masteroppgave\Marens_arbeid\Prosjektoppgave\Labelmaps\
    {image}{appx}_ADC_vial1_d20mm-label.nii.gz'
)


# ------------------------------------------------------ #
#  Calculate temporal noise image and signal image  #
# ------------------------------------------------------ #
# Temporal noise image: std of the pixel values of the repeated scans
# Signal image: mean of the pixel values of the repeated scans

l, m, n = segmentation.shape  # number of rows, columns, and slices
N = np.sum(segmentation)  # number of pixels in ROI

# b-value SNR:
# Open file
filename = f"{image}{appx}_SNR_bvalues.txt"
file = open(f"./results/{filename}", "w")
```

```
file.write(f"{image.replace('_',' ')}{appx.replace('_',' ')} - SNR"
           f"\n\n")
print(f"{image.replace('_',' ')}{appx.replace('_',' ')} - SNR\n")

# loop through all b-values
for b in bs:
    print(f"b = {b}:")
    file.write(f"b = {b}\n")

    # loop through all averages
    for av in avs:
        # Create array for storing all image passes
        image_all_passes = np.empty((4, 1, m, n))

        # Import all passes
        for pass_nr in range(1, 5):
            image_all_passes[pass_nr - 1] = unpack_nifty(
                f'./data/{image}{av}AV_PASS{pass_nr}_b{b:04d}'
                f'{appx}.nii.gz'
            )

        # Calculate temporal noise image and signal image
        temporal_noise_image = np.std(image_all_passes, axis=0)
        signal_image = np.mean(image_all_passes, axis=0)

        # Calculate SNR and CI
        SNR_nDyn = np.average(signal_image, weights=segmentation) / \
                   np.average(temporal_noise_image, weights=segmentation)

        sCV = weighted_sample_std(signal_image, segmentation) / \
              np.average(signal_image, weights=segmentation)
        nCV = weighted_sample_std(temporal_noise_image, segmentation) /\
              np.average(temporal_noise_image, weights=segmentation)

        CI = 1.96 * SNR_nDyn * np.sqrt(sCV**2 + nCV**2) / np.sqrt(N)

        # Write results to file
        print(f"{av}AV: {round(SNR_nDyn, 2)} +- {round(CI, 2)}")
        file.write(f"{av}AV: {round(SNR_nDyn, 2)} +- {round(CI, 2)}\n")

    print()
    file.write("\n")

file.close()
```

```
print("\n\n")


# ADC SNR:
if not bvalue_only:
    # Open file
    filename = f"{image}{appx}_SNR_ADC.txt"
    file = open(f"./results/{filename}", "w")
    file.write(f"{image.replace('_',' ')}{appx.replace('_',' ')} - ADC SNR"
               f"\n\n")
    print(f"{image.replace('_',' ')}{appx.replace('_',' ')} - ADC SNR\n")

    # loop through all averages
    for av in avs:
        # Create array for storing all image passes
        image_all_passes = np.empty((4, 1, m, n))

        # Import all passes
        for pass_nr in range(1, 5):
            image_all_passes[pass_nr - 1] = unpack_nifty(
                f'./data/{image}{av}AV_PASS{pass_nr}_ADC{appx}.nii.gz'
            )

        # Calculate temporal noise image and signal image
        temporal_noise_image = np.std(image_all_passes, axis=0)
        signal_image = np.mean(image_all_passes, axis=0)

        # Calculate SNR and CI
        SNR_nDyn = np.average(signal_image, weights=segmentation) / \
                   np.average(temporal_noise_image, weights=segmentation)

        sCV = weighted_sample_std(signal_image, segmentation) / np.\
            average(signal_image, weights=segmentation)
        nCV = weighted_sample_std(temporal_noise_image, segmentation) /\
              np.average(temporal_noise_image, weights=segmentation)

        CI = 1.96 * SNR_nDyn * np.sqrt(sCV ** 2 + nCV ** 2) / np.sqrt(N)

        # Write results to file
        print(f"{av}AV: {round(SNR_nDyn, 2)} +- {round(CI, 2)}")
        file.write(f"{av}AV: {round(SNR_nDyn, 2)} +- {round(CI, 2)}\n")

    file.close()
```

Matlab code used for ACR QA

The code used for the ACR QA is written at the PET-center at ST.Olavs and used there for QA for the MRI-scanners at the center. The script has functions for all tests in the ACR QA where calculation or measurement of distance is required. The code in its full size is not included in this thesis as a consequence of the length and the low level of complexity in calculation in most of the measures. The code calculating the PIU (in F) and ghosting (in G) is included only to show a part of the code.

F PIU calculation

```
%INFO ABOUT THE SCRIPT
%A script that calculates PIU from slice 7 of the ACR
%phantom, and also displays the location of the ROIs with highest minimum
%and maximum intensities

%DESCRIPTION
%Use the OpenDicomFiles.m script to open the image and dicom info. Then run
%the script

%INPUT
%radiusLargeROI: radius of spherical large ROI inside the phantom, in mm.
The description suggest to use 80 mm
%radiusSmallROI: radius of the small ROI in mm. The description suggest to
%use 1.12 cm in diameter

%Written by MTG, Dec 5th 2018

%Change if needed
radiusLargeROI=78; %endrer fra 80 til 78 for    unng  at ROI toucher luft
radiusSmallROI=11.2/2;

%Don't change text below
[sentrum,radius,urundhet] = felles__finn_sentrum_av_fantom(X); %Script that
%defines the middle of the phantom
%sentrum=[269 270]
PixelSize=info.PixelSpacing(1,:);
[LX,WX]=size(X);

%CALCULATION FOR LARGE CIRCULAR ROI
RLargeROI=radiusLargeROI/PixelSize; %RLargeROI is radius in number of pixels
[xgrid, ygrid] = meshgrid(1:size(X,2), 1:size(X,1)); %Defines two matrixes
%that describes the coordinates of the image
maskLargeROI = ((xgrid-sentrum(1,1)).^2 + (ygrid-sentrum(1,2)).^2) <= RLargeROI.^2;
%masks a circular ROI with a radius RLargeROI from the midle of the phantom
maskLargeROI_double= double(maskLargeROI); %converts the logical variable into a
```

```
%double variable
X_double=im2double(X)*65535; %converts X into double. To have the same value
%as the value for uint, I must multiply by 65535, since uint 16 is Unsigned
%16-bit integer and values goes from 0 to 65535
valuesImageLargeROI=maskLargeROI_double.*(X_double); %valuesImageLargeROI
%contain the pixel values within the large circular ROI
AreaLargeROI=((sum(maskLargeROI(:) == 1))*PixelSize^2)/100; %in cm^2. Should
%be approximately 200cm^2

%CALCULATION FOR SMALL CIRCULAR ROI
RSmallROI=radiusSmallROI/PixelSize; %RSmallROI is radius in number of pixels

%viscircles([centerX, centerY], RSmallROI);
%axis square;
[x,y] = meshgrid(1:RSmallROI*2, 1:RSmallROI*2);
isinside = (x - RSmallROI).^2 + (y - RSmallROI).^2 <= RSmallROI^2;

%FIND ROI WITH MAX INTENSITY
%Now I do convolution in order to create a matrix containing values that
%describe the the sum of pixel values inside the small ROI inside
%the mask of the phantom
ConvMatrixTemp = conv2(valuesImageLargeROI,isinside);
%The final matrix is larger than size(X), and must be decreased to size(X)
ConvMatrix=ConvMatrixTemp(round(RSmallROI):size(ConvMatrixTemp)-round(RSmallROI)
,round(RSmallROI):size(ConvMatrixTemp)-round(RSmallROI));
MaxConvMatrix = max(ConvMatrix(:)); %Find the maximum value in the
%convolution matrix
[Max_row, Max_col] = find(ismember(ConvMatrix, max(ConvMatrix(:))));

%FIND ROI WITH MIN INTENSITY
X_compl = imcomplement(X); %calculate the complement (inverted) X using the
%imcomplement command
X_compl_double=im2double(X_compl)*65535; %converts X2 into double. To have
%the same value as the value for uint, I must multiply by 65535,
%since uint 16 is Unsigned 16-bit integer and values goes from 0 to 65535
valuesImageLargeROI_X_compl=maskLargeROI_double.*(X_compl_double);
%figure
%imshow(valuesImageLargeROI,[]);
ConvMatrix_X_comp_Temp = conv2(valuesImageLargeROI_X_compl,isinside);
%The final matrix is larger than size(X), and must be decreased to size(X)
ConvMatrix_X_compl=ConvMatrix_X_comp_Temp(round(RSmallROI)
:size(ConvMatrix_X_comp_Temp)-round(RSmallROI),round(RSmallROI)
:size(ConvMatrix_X_comp_Temp)-round(RSmallROI));
MaxConvMatrix_X_compl = max(ConvMatrix_X_compl(:)); %Find the maximum value
%in the convolution matrix
[Max_row2, Max_col2] = find(ismember(ConvMatrix_X_compl, max(ConvMatrix_X_compl(:))));
```

```
%FIGURES
figure
%Large circular ROI
th = 0:pi/50:2*pi;
xunit = RLargeROI * cos(th) + sentrum(1,1);
yunit = RLargeROI * sin(th) + sentrum(1,2);

%Small circular ROI with max intensity
xunit_small = RSmallROI * cos(th) + Max_col;
yunit_small = RSmallROI * sin(th) + Max_row;

%Small circular ROI with min intensity
xunit_small_2 = RSmallROI * cos(th) + Max_col2;
yunit_small_2 = RSmallROI * sin(th) + Max_row2;

imshow(X,[]);
title('Phantom, large circular ROI and small circular ROI with '
'min (red) and max (blue) intensities')
hold on
h = plot(xunit, yunit);
% legend=('Large Circular ROI')
hold on
h2=plot(xunit_small,yunit_small,'Color','blue');
% legend=('ROI with highest pixel values')
hold on
h3=plot(xunit_small_2,yunit_small_2,'Color','red');
hold off
%legend('Large Circular ROI','ROI with highest pixel values')
imcontrast

%subplot(2,2,2)
%imshow(valuesImageLargeROI,[]);
%title('Mask of large ROI')
%subplot(2,2,3)
%imshow(isinside);
%title('Small circular ROI')

%FINALLY CALCULATION OF MIN AND MAX AND PIU

[columnsInImage rowsInImage] = meshgrid(1:length(X), 1:length(X));

% THE ROI WITH MINIMUM INTENSITY
[xgrid, ygrid] = meshgrid(1:size(X,2), 1:size(X,1)); %Defines to matrixes
%that describes the coordinates of the image
```

```
maskROIMin = (xgrid-Max_col2(1,1)).^2 + (ygrid-Max_row2(1,1)).^2 <= RSmallROI.^2;
%masks a circular ROI with a radius RLargeROI from the midle of the phantom
valuesROIMin = X(maskROIMin); %defines a column with all the pixel values in the mask
PIU_LowSignalMean=mean(valuesROIMin)

%THE ROI WITH MAXIMUM INTENSITY
maskROIMax = (xgrid-Max_col(1,1)).^2 + (ygrid-Max_row(1,1)).^2 <= RSmallROI.^2;
%masks a circular ROI with a radius RLargeROI from the midle of the phantom
valuesROIMax = X(maskROIMax); %defines a column with all the pixel values in the mask
PIU_HighSignalMean=mean(valuesROIMax)

PIU=100*(1-(PIU_HighSignalMean-PIU_LowSignalMean)/
(PIU_HighSignalMean+PIU_LowSignalMean))


%% Section save matlab data

%Save the all variables
%save ('PIU_filename');

%Save only the most important variables
%save('PIU_Important_filename.mat','PIU','HighSignalMean','LowSignalMean')


% filename = 'QualityControls_MRI';
% A = {'Calculated PIU','PIU: Low signal mean','PIU: High signal mean';
%PIU, HighSignalMean, LowSignalMean};
% sheet = 2;
% xlRange = 'B2';
% warning( 'off', 'MATLAB:xlswrite:AddSheet' ) ;
% xlswrite(filename,A,sheet,xlRange)
```

G Ghosting ratio calculation

```
%INFO ABOUT THE SCRIPT
%A script that calculates PIU from slice 7 of the ACR
%phantom, and also displays the location of the ROIs with highest minimum
%and maximum intensities

%DESCRIPTION
%Use the OpenDicomFiles.m script to open the image and dicom info. Then run
%the script

%INPUT
%radiusLargeROI: radius of spherical large ROI inside the phantom, in mm.
The description suggest to use 80 mm
%radiusSmallROI: radius of the small ROI in mm. The description suggest to
```

```
%use 1.12 cm in diameter

%Written by MTG, Dec 5th 2018

%Change if needed
radiusLargeROI=78; %endrer fra 80 til 78 for    unng  at ROI toucher luft
radiusSmallROI=11.2/2;

%Don't change text below
[sentrum,radius,urundhet] = felles__finn_sentrum_av_fantom(X); %Script that
%defines the middle of the phantom
%sentrum=[269 270]
PixelSize=info.PixelSpacing(1,:);
[LX,WX]=size(X);

%CALCULATION FOR LARGE CIRCULAR ROI
RLargeROI=radiusLargeROI/PixelSize; %RLargeROI is radius in number of pixels
[xgrid, ygrid] = meshgrid(1:size(X,2), 1:size(X,1)); %Defines two matrixes
%that describes the coordinates of the image
maskLargeROI = ((xgrid-sentrum(1,1)).^2 + (ygrid-sentrum(1,2)).^2) <= RLargeROI.^2;
%masks a circular ROI with a radius RLargeROI from the midle of the phantom
maskLargeROI_double= double(maskLargeROI); %converts the logical variable into a
%double variable
X_double=im2double(X)*65535; %converts X into double. To have the same value
%as the value for uint, I must multiply by 65535, since uint 16 is Unsigned
%16-bit integer and values goes from 0 to 65535
valuesImageLargeROI=maskLargeROI_double.*(X_double); %valuesImageLargeROI
%contain the pixel values within the large circular ROI
AreaLargeROI=((sum(maskLargeROI(:) == 1))*PixelSize^2)/100; %in cm^2. Should
%be approximately 200cm^2

%CALCULATION FOR SMALL CIRCULAR ROI
RSmallROI=radiusSmallROI/PixelSize; %RSmallROI is radius in number of pixels

%viscircles([centerX, centerY], RSmallROI);
%axis square;
[x,y] = meshgrid(1:RSmallROI*2, 1:RSmallROI*2);
isinside = (x - RSmallROI).^2 + (y - RSmallROI).^2 <= RSmallROI^2;

%FIND ROI WITH MAX INTENSITY
%Now I do convolution in order to create a matrix containing values that
%describe the the sum of pixel values inside the small ROI inside
%the mask of the phantom
ConvMatrixTemp = conv2(valuesImageLargeROI,isinside);
%The final matrix is larger than size(X), and must be decreased to size(X)
ConvMatrix=ConvMatrixTemp(round(RSmallROI):size(ConvMatrixTemp)-round(RSmallROI)
```

```
,round(RSmallROI):size(ConvMatrixTemp)-round(RSmallROI));
MaxConvMatrix = max(ConvMatrix(:)); %Find the maximum value in the
%convolution matrix
[Max_row, Max_col] = find(ismember(ConvMatrix, max(ConvMatrix(:))));

%FIND ROI WITH MIN INTENSITY
X_compl = imcomplement(X); %calculate the complement (inverted) X using the
%imcomplement command
X_compl_double=im2double(X_compl)*65535; %converts X2 into double. To have
%the same value as the value for uint, I must multiply by 65535,
%since uint 16 is Unsigned 16-bit integer and values goes from 0 to 65535
valuesImageLargeROI_X_compl=maskLargeROI_double.*(X_compl_double);
%figure
%imshow(valuesImageLargeROI,[]);
ConvMatrix_X_comp_Temp = conv2(valuesImageLargeROI_X_compl,isinside);
%The final matrix is larger than size(X), and must be decreased to size(X)
ConvMatrix_X_compl=ConvMatrix_X_comp_Temp(round(RSmallROI)
:size(ConvMatrix_X_comp_Temp)-round(RSmallROI),round(RSmallROI)
:size(ConvMatrix_X_comp_Temp)-round(RSmallROI));
MaxConvMatrix_X_compl = max(ConvMatrix_X_compl(:)); %Find the maximum value
%in the convolution matrix
[Max_row2, Max_col2] = find(ismember(ConvMatrix_X_compl, max(ConvMatrix_X_compl(:))));



%FIGURES
figure
%Large circular ROI
th = 0:pi/50:2*pi;
xunit = RLargeROI * cos(th) + sentrum(1,1);
yunit = RLargeROI * sin(th) + sentrum(1,2);

%Small circular ROI with max intensity
xunit_small = RSmallROI * cos(th) + Max_col;
yunit_small = RSmallROI * sin(th) + Max_row;

%Small circular ROI with min intensity
xunit_small_2 = RSmallROI * cos(th) + Max_col2;
yunit_small_2 = RSmallROI * sin(th) + Max_row2;

imshow(X,[]);
title('Phantom, large circular ROI and small circular ROI with'
'min (red) and max (blue) intensities')
hold on
h = plot(xunit, yunit);
% legend=('Large Circular ROI')
hold on
```

```
h2=plot(xunit_small,yunit_small,'Color','blue');
% legend=('ROI with highest pixel values')
hold on
h3=plot(xunit_small_2,yunit_small_2,'Color','red');
hold off
%legend('Large Circular ROI','ROI with highest pixel values')
imcontrast

%subplot(2,2,2)
%imshow(valuesImageLargeROI,[]);
%title('Mask of large ROI')
%subplot(2,2,3)
%imshow(isinside);
%title('Small circular ROI')

%FINALLY CALCULATION OF MIN AND MAX AND PIU

[columnsInImage rowsInImage] = meshgrid(1:length(X), 1:length(X));

% THE ROI WITH MINIMUM INTENSITY
[xgrid, ygrid] = meshgrid(1:size(X,2), 1:size(X,1)); %Defines to matrixes
%that describes the coordinates of the image
maskROIMin = (xgrid-Max_col2(1,1)).^2 + (ygrid-Max_row2(1,1)).^2 <= RSmallROI.^2;
%masks a circular ROI with a radius RLargeROI from the midle of the phantom
valuesROIMin = X(maskROIMin); %defines a column with all the pixel values in the mask
PIU_LowSignalMean=mean(valuesROIMin)

%THE ROI WITH MAXIMUM INTENSITY
maskROIMax = (xgrid-Max_col(1,1)).^2 + (ygrid-Max_row(1,1)).^2 <= RSmallROI.^2;
%masks a circular ROI with a radius RLargeROI from the midle of the phantom
valuesROIMax = X(maskROIMax); %defines a column with all the pixel values in the mask
PIU_HighSignalMean=mean(valuesROIMax)

PIU=100*(1-(PIU_HighSignalMean-PIU_LowSignalMean)/
(PIU_HighSignalMean+PIU_LowSignalMean))


%% Section save matlab data

%Save the all variables
%save ('PIU_filename');

%Save only the most important variables
%save('PIU_Important_filename.mat','PIU','HighSignalMean','LowSignalMean')
```

```
% filename = 'QualityControls_MRI';
% A = {'Calculated PIU','PIU: Low signal mean','PIU: High signal mean';
%PIU, HighSignalMean, LowSignalMean};
% sheet = 2;
% xlRange = 'B2';
% warning( 'off', 'MATLAB:xlswrite:AddSheet' ) ;
% xlswrite(filename,A,sheet,xlRange)
```

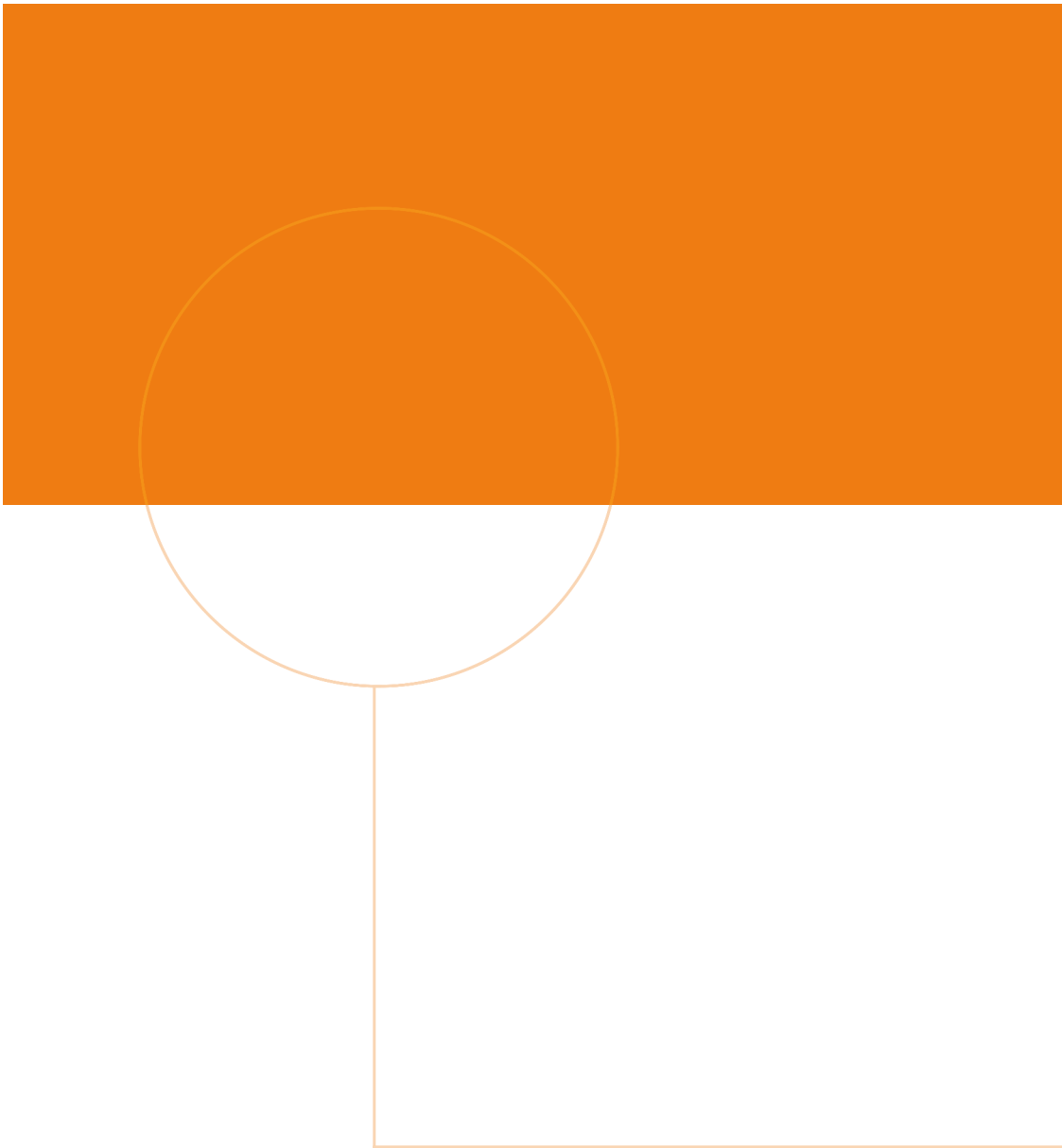

NTNU

Norwegian University of
Science and Technology